MINISTÉRIO DA CIÊNCIA, TECNOLOGIA, INOVAÇÕES E COMUNICAÇÕES
INSTITUTO NACIONAL DE PESQUISAS ESPACIAIS

sid.inpe.br/mtc-m21b/2017/02.02.15.30-TDI

A STUDY OF DAYTIME MSTIDS OVER EQUATORIAL AND LOW LATITUDE REGIONS DURING TROPOSPHERIC CONVECTION: OBSERVATIONS AND SIMULATIONS

Olusegun Folarin Jonah

Doctorate Thesis of the Graduate Course in Space Geophysics, guided by Drs. Eurico Rodrigues de Paula, and Esfhan Alam Kherani, approved in February 17, 2017.

URL of the original document:
<http://urlib.net/8JMKD3MGP3W34P/3NAAB2L>

INPE
São José dos Campos
2017

PUBLISHED BY:

Instituto Nacional de Pesquisas Espaciais - INPE
Gabinete do Diretor (GB)
Serviço de Informação e Documentação (SID)
Caixa Postal 515 - CEP 12.245-970
São José dos Campos - SP - Brasil
Tel.:(012) 3208-6923/6921
Fax: (012) 3208-6919
E-mail: pubtc@inpe.br

MINISTÉRIO DA CIÊNCIA, TECNOLOGIA, INOVAÇÕES E COMUNICAÇÕES
INSTITUTO NACIONAL DE PESQUISAS ESPACIAIS

sid.inpe.br/mtc-m21b/2017/02.02.15.30-TDI

A STUDY OF DAYTIME MSTIDS OVER EQUATORIAL AND LOW LATITUDE REGIONS DURING TROPOSPHERIC CONVECTION: OBSERVATIONS AND SIMULATIONS

Olusegun Folarin Jonah

Doctorate Thesis of the Graduate Course in Space Geophysics, guided by Drs. Eurico Rodrigues de Paula, and Esfhan Alam Kherani, approved in February 17, 2017.

URL of the original document:
<http://urlib.net/8JMKD3MGP3W34P/3NAAB2L>

INPE
São José dos Campos
2017

Cataloging in Publication Data

Jonah, Olusegun Folarin.

J69s A study of daytime MSTIDs over equatorial and low latitude regions during tropospheric convection: observations and simulations / Olusegun Folarin Jonah. – São José dos Campos : INPE, 2017.

xxviii + 159 p. ; (sid.inpe.br/mtc-m21b/2017/02.02.15.30-TDI)

Thesis (Doctorate in Space Geophysics) – Instituto Nacional de Pesquisas Espaciais, São José dos Campos, 2017.

Guiding : Drs. Eurico Rodrigues de Paula, and Esfhan Alam Kherani.

1. TEC. 2. Daytime MSTIDs generation mechanisms. 3. AGW activities. 4. Convective weather activities. 5. Daytime MSTIDs geomagnetic conjugate mappings. I.Title.

CDU 551.510.535:523.4-852

Aluno (a): ***Olusegun Folarin Jonah***

Título: "A STUDY OF DAYTIME MSTIDS OVER EQUATORIAL AND LOW LATITUDE REGIONS DURING TROPOSPHERIC CONVECTION: OBSERVATIONS AND SIMULATIONS".

Aprovado (a) pela Banca Examinadora em cumprimento ao requisito exigido para obtenção do Título de ***Doutor(a)*** em

Geofísica Espacial/Ciências do Ambiente Solar-Terrestre

Dra. Maria Virginia Alves

Presidente / INPE / SJCampos - SP

Dr. Eurico Rodrigues de Paula

Orientador(a) / INPE / SJCampos - SP

Dr. Esfhan Alam Kherani

Orientador(a) / INPE / SJCampos - SP

Dr. Alexandre Alvares Pimenta

Membro da Banca / INPE / SJCampos - SP

Dr. Cesar Valladares

Convidado(a) / University of Texas / Dallas - USA

Dra. Virginia Klausner de Oliveira

Convidado(a) / UNIVAP / São José dos Campos - SP

Este trabalho foi aprovado por:

( ) maioria simples

(X) unanimidade

São José dos Campos, 17 de Fevereiro de 2017

The best preparation for tomorrow is doing your best today.
Jackson Brown, Jr.

This research thesis is dedicated to the glory of God

and

in memory of my father, Pa. Olukayode J. Jonah. May his soul rest in peace.

ACKNOWLEDGEMENT

I am grateful to the Almighty God for His faithfulness and favor during the course of this program.

I deeply appreciate my supervisors Drs. Eurico R. de Paula and Esfhan Alam Kherani for their strong academic supervision, guidance and intelligent suggestions throughout the research period. I am indebted to them for their positive criticism and numerous contributions which are instrumental to the timely completion of my program.

Special appreciation goes to Dr. Joe Huba from the Naval Research Laboratory who made SAMI3 model available to me and gave necessary guidance on the implementation.
I would like to thank Dr. Mangalathayil A. Abdu from INPE, Dr. Bela G. Fejer from the Utah state University, Dra. Anthea Coster from MIT Haystack Observatory, USA for giving their time for useful discussions. I am also grateful to Dra. Inez S. Batista and Maria G. S. Aquino for making the digisonde data available for this research. I acknowledge the CPTEC/INPE staffs who provided the water vapor and infrered data.

I am fortunate to have kind and generous people whose emotional support and enthusiasm have contributed to the success of my work. I thank all of them for their generosity, especially: Conceição Alves and Fatima Usifatti (Division secretaries), Dra. Patricia De Siqueira Negreti, Dra. Claudia Nicoli, Jonas Souza, Régia Pereira, Manuel Bravo, Felipe Guilherme, Ebenezer Chellasamy, Paulo André etc. You are all wonderful people and I will never forget you.

I thank the Brazilian government through the Coordenação de Aperfeiçoamento de Pessoal de Nível Superior (CAPES) and the Conselho Nacional de Desenvolvimento Científico e Tecnológico (CNPq) for the PhD fellowship awarded and for the sponsorship of my program at the National Institute for Space Research (INPE).

Special acknowledgement also goes to Prof. and Mrs. Laseinde for their prayers, constant love and concern for me and my family. May the Almighty God reward them greatly. I also thank Prof. Babatunde Rabiu and his family for all their support and trust.

This acknowledgement will be incomplete if I fail to mention my dear wife, Dra. Ifeloju Folarin-Jonah and my handsome twin boys (Samuel Oluwaseun Folarin Jonah and Paulo Oluwanife Folarin Jonah) for their understating, support and encouragement. I owe you all a lot.

Finally, I am deeply grateful to my late father, Mr. Olukayode Jonah (I miss him every day, but I am glad to know he witnessed this process through to its completion, offering the support to make it possible) and my mother Olanike Jonah for their good moral, and prayer supports, without which I would not have been able to attain this height. Thank you for your love. I thank you all very much.

Olusegun Folarin Jonah

A STUDY OF DAYTIME MSTIDS OVER EQUATORIAL AND LOW LATITUDE REGIONS DURING TROPOSPHERIC CONVECTION: OBSERVATIONS AND SIMULATIONS

ABSTRACT

Medium Scale Travelling Ionospheric Disturbances (MSTIDs) are the highly dynamical phenomenona covering all latitudes in the F region ionosphere and they propagate a long distance, often in the form of wave-fronts. Their presence in a wide region pose threat to the radio propagation and trigger the equatorial plasma bubble which disrupts the GNSS navigation system. Atmospheric Gravity Wave (AGW) is believed to be the cause of these MSTIDs during daytime. However, the seeding mechanism of these AGWs is still a research question. The objective of this thesis is to study the dynamics of daytime MSTIDs over Brazil using detrended TEC, with focus on understanding their propagation characteristics. In addition, this thesis also presents novel results on daytime MSTIDs geomagnetic conjugate mapping characteristics and mechanisms responsible. Both observational and theoretical tools are employed to pursue these objectives. Observational data obtained using instruments such as a network of GNSS receivers, digisonde, low-orbiting satellites (COSMIC) and meteorological satellites (GOES Satellite) are analyzed to identify the driving source of MSTIDs-AGW. Interesting characteristics associated with the widely pursued convective-AGWs driven generation mechanism from past literatures, are investigated. This mechanism is further studied theoretically, by adapting a Convectional-Atmosphere-Ionosphere-Coupled model (CAI-CM) to incorporate the dynamics of convectively generated AGWs and their coupling to the ionosphere. The numerical simulation work also utilizes the SAMI3 (Sami3 is Another Model of the Ionosphere) model to capture the fundamental physics of the ionosphere. The SAMI3 model is used to simulate a large region of the ionosphere for the self-consistent development of MSTIDs. Finally the simulated MSTIDs from both CAI-CM and SAMI3 model are compared with the observed MSTIDs.

KEY WORDS:
TEC; Daytime MSTIDs generation mechanisms; AGW activities; Convective weather activities; Daytime MSTIDs geomagnetic conjugate mappings.

UM ESTUDO DE MSTIDS DO DIA POR REGIÕES EQUATORIA E BAIXA LATITUDE DURANTE A CONVECÇÃO TROPOSFÉRICA: OBSERVAÇÕES E SIMULAÇÕES

RESUMO

Os Distúrbios ionosféricos propagantes de média escala (MSTIDs) são fenômenos altamente dinâmicos que cobrem todas as latitudes na ionosfera da região F e propagam uma longa distância, geralmente sob a forma de frentes de onda. Suas presenças em uma região ampla afetam a propagação de rádio e podem gerar a bolha de plasma equatorial, a qual por sua vez pode interromper o sistema de navegação GNSS. Acredita-se que a Onda de Gravidade Atmosférica (AGW) seja a causa destes MSTIDs durante o dia. No entanto, o mecanismo de geração destas AGWs ainda é uma questão de pesquisa. O objetivo desta tese é estudar a dinâmica das MSTIDs diurnas sobre o Brasil utilizando TEC após a remocão da tendência, com foco na compreensão de suas características de propagação. Além disso, esta tese também apresenta novos resultados sobre as características de mapeamento do conjugado geomagnético do MSTID diurno e os mecanismos responsáveis. Ambos instrumentos observacionais e teóricos são empregados para atingir esses objetivos. Os dados observacionais obtidos usando instrumentos como uma rede de receptores GNSS, digissonda, satélites de baixa órbita (COSMIC) e satélites meteorológicos (GOES) são analisados para identificar os mecanismos de geração das MSTIDs-AGW. São investigadas características interessantes associadas ao mecanismo de geração por AGWs convectivas amplamente persquisadas em literaturas passadas. Este mecanismo é ainda estudado teoricamente, adaptando um modelo Convectional-Atmosphere-Ionosphere-Coupled (CAI-CM) para incorporar a dinâmica de AGWs convectivamente geradas e seu acoplamento com a ionosfera. O trabalho de simulação numérica também utiliza o modelo SAMI3 (Sami3 é Outro Modelo da Ionosfera) para capturar a física fundamental da ionosfera. O modelo SAMI3 é usado para simular uma grande região da ionosfera para o desenvolvimento

auto-consistente de MSTIDs. Finalmente, as MSTIDs simuladas do modelo CAI-CM e SAMI3 são comparadas com as MSTIDs observadas.

PALAVRAS-CHAVE:
TEC; Mecanismos de geração de MSTIDs diurnos; AGW atividade; Atividade climatérica convectiva; Mapeamento do conjugado geomagnético MSTIDs diurno.

LIST OF FIGURES

LIST OF TABLES

LIST OF ABBREVIATIONS

AGW	-	Atmospheric Gravity Wave
ATEC	-	Absolute Total Electron Content
CAI-CM	-	Convectional-Atmosphere-Ionosphere-Coupled Model
CDAAC	-	COSMIC Data Analysis and Archival Center
COSMIC	-	Constellation Observing System for Meteorology,
CPTEC	-	Centro de Previsão de Tempo e Estudos Climáticos
CST	-	Central Standard Time
DoD	-	Department of Defense's America
EGNOS	-	European Geostationary Navigation Overlay Service
Ep	-	Polarization Electric field
Es	-	Sporadic E layer
Esb	-	Blanketing type sporadic E
ESF	-	Equatorial Spread F
EUV	-	Extreme Ultraviolent radiation
fbEs	-	Blanketing frequency of the Es layer
FFT	-	Fast Fourier Transform
foE	-	Critical frequency of E layer
foEs	-	Critical frequency of sporadic E layer
foF1	-	Critical frequency of F1 layer
foF2	-	Critical frequency of F2 layer
GAGAN	-	GPS Aided Geo Augmented Navigation
GLONASS	-	Russia's Global Navigation Satellite System
GNSS	-	Global Navigation Satellite System
GOES	-	Geostationary Operational Environmental Satellite System
GPS	-	Global Positioning System
GPS-RO	-	Global Positioning System Radio Occultation
GW	-	Gravity Wave
hF	-	Height of F layer
hF8MHz	-	Height of F layer at 8 MHz
hvE	-	Virtual frequency of E layer

hvF1	-	Virtual frequency of F1 layer
hvF2	-	Virtual frequency of F2 layer
IBGE	-	Instituto Brasileiro de Geografia e Estatística
IR	-	Infrared
ITCZ	-	Inter Tropical Convergence Zone
LEO	-	Low Earth Satellite Orbit
LHS	-	Left Hand Side
LSTIDs	-	Large Scale Travelling Ionospheric Disturbances
MSAS	-	Multi-functional Satellite Augmentation System
MSTIDs	-	Medium Scale Travelling Ionospheric Disturbances
NAVSTAR System	-	Navigation System with Time and Ranging Positioning
NE	-	Northeastward
Ne8MHz	-	Electron density at 8 Mega-hertz
NH	-	Northern Hemisphere
NmE	-	Electron density of E layer
NRLMSISE	-	Naval Research Laboratory Mass Spectrometer and and Incoherent Scatter Radar
NW	-	Northwestward
RBMC	-	Rede Brasileira de Monitoramento Contínuo
RHS	-	Right Hand Side
RTI	-	Range Time Intensity
SADM-GPS	-	Statistical Angle of Arrival and Doppler Method
SAMI2	-	Sami2 is Another Model of the Ionosphere
SAMI3	-	Sami3 is Another Model of the Ionosphere
SBAS	-	Space Based Augmentation System
SE	-	Southeastward
SH	-	Southern Hemisphere
SOPAC	-	Scripts and Permanent Array Centre
SW	-	Southwestward
TEC	-	Total Electron Content

TECMAP	-	Total Electron Content MAP
TIDs	-	Travelling Ionospheric Disturbances
UCAR	-	University Corporation for Atmospheric Research
UV	-	Ultraviolent radiation
VTEC	-	Vertical Total Electron Content
WAAS	-	Wide Area Augmentation System
WV	-	Water Vapor
ZTO	-	Zenith Tropospheric Delay

TABLE OF CONTENTS

1.0 INTRODUCTION

This chapter gives brief introduction about the motivation for the daytime MSTIDs study, some background on atmosphere and the fundamental characteristics of the ionosphere, including the constituents of the regions and the basic physics that govern the ionosphere in relation with the electrified Medium-Scale Travelling Ionospheric Disturbances (MSTIDs). The chapter also outlines the aims and objectives as well as the contributions of the research. Finally, the scopes of the study are enumerated.

Daytime MSTIDs have been observed using data from various techniques such as ionosondes, High Frequency (HF) Doppler sounders, satellite beacons, and incoherent scatter radars (HOCKE; SCHLEGEL, 1996). With the rapid advancements of satellite techniques in recent years, the global coverage of ionosphere brought an opportunity to study these MSTIDs in great detail [e.g. TSUGAWA et al., 2007; OTSUKA et al., 2011, 2013; HERNANDEZ-PAJARES et al., 2006; 2012). With the dense Global Navigation Satellite System (GNSS) receiver network over Northern hemisphere, studies have revealed the finer details of MSTIDs such as (a) their amplitudes which can be as large as 10% of the background, (b) their preferred direction of propagation towards equatorward-eastward (daytime) and equatorward-westward (nighttime) in the south and north hemisphere respectively (c) their association with the AGW activities and electrodynamics processes.

While there have been few studies on daytime MSTIDs using the GNSS receiver network (e.g. HERNANDEZ-PAJARES et al., 2006; 2012, GROCOTT et al., 2013, JONAH et al, 2016), most of the studies over southern hemisphere (e.g. Brazil) have been limited to the nighttime MSTIDs observed using the all-sky imagers (PIMENTA et al., 2008; CANDIDO et al., 2008; AMORIM et al., 2011). Unlike northern hemisphere, over most parts of the southern hemisphere, the detailed features of daytime MSTIDs are not reported mainly due to the limited spatial resolution of the GNSS network. In recent years,

however, with improved spatial resolution of GNSS over Brazil, varieties of large scale ionospheric phenomena such as the 4 wave structures and TEC variability over South American sector [NOGUEIRA et al., 2013, JONAH et al., 2015], TEC disturbances during SSW (JONAH et al., 2014; PAES et al., 2014), as well as medium scale phenomena such as the plasma bubbles (TAKAHASHI et al., 2014, 2016] have been reported using the GNSS technology. These studies have given a direction to further explore the possibility of identifying the MSTIDs from the TEC measurements and consequently investigating the generation mechanisms.

1.1 Background description of the Atmosphere

Over the years the earth's atmosphere has become an interesting open field for scientific study. It consists of mainly Nitrogen and Oxygen of up to 99% of the whole atmosphere at sea level, with the remaining 1% comprising CO_2, noble gases and traces of many gaseous substances which are kept in space mainly by gravitational attractions. The Earth's atmosphere is denser at the surface and gets progressively rarefied with increasing altitude, since density decreases exponentially with height. The vertical distribution of temperature, pressure, density, and composition of constituents of the atmospheric structure are very crucial for the description of the atmospheric variations. The pressure and density of the atmosphere decrease exponentially with altitude. Solar radiation and internal chemical processes set up within the atmosphere create a temperature profile that varies significantly with altitude, generating four distinct regions: Troposphere, Stratosphere, Mesosphere, and Thermosphere. The boundaries separating these atmospheric regions are referred to as pauses having zero gradient of temperature. Figure 1.1 shows the atmospheric thermal structure and the ionospheric profile.

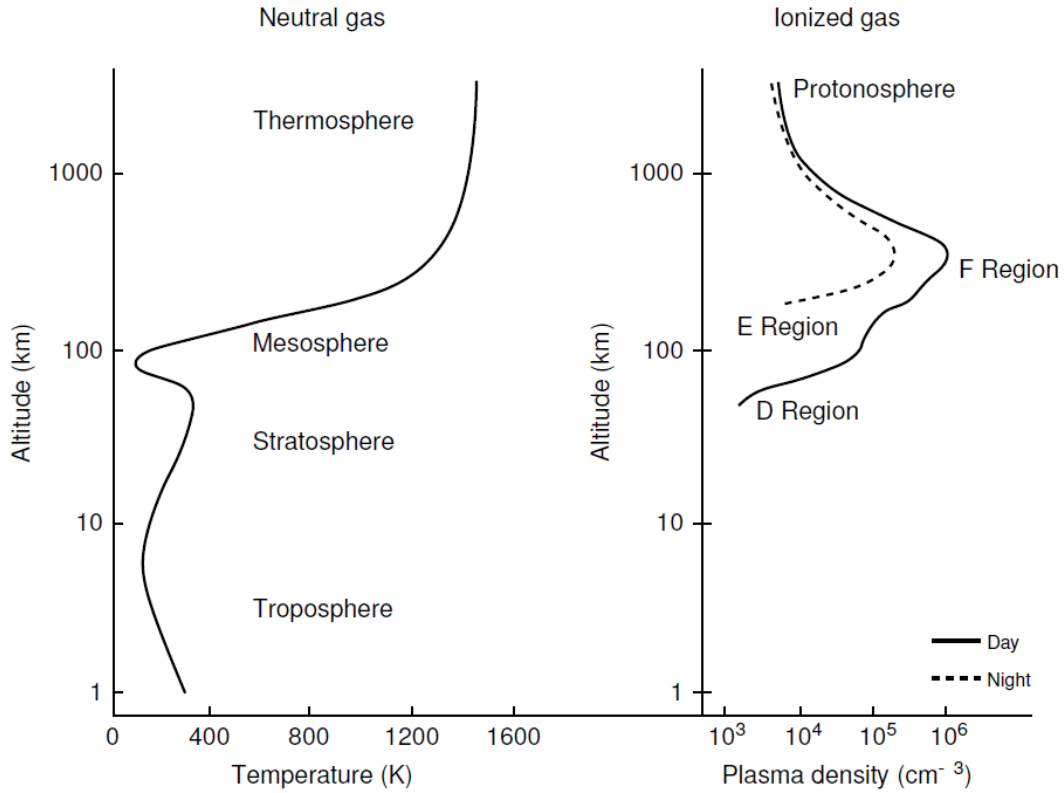

Figure 1.1 - Temperature profile of the neutral atmosphere (left) and ionospheric layers according to their electron density concentrations (right). SOURCE: Rishbeth and Garriott (1969).

In the following paragraphs the atmospheric layers classified mainly by temperature will be described.

Troposphere: 75 percent of atmosphere's mass and most of the atmosphere's water vapor lies in the troposphere. The temperature and water vapor content in the troposphere decrease rapidly with altitude. Water vapor plays a major role in regulating air temperature because it absorbs solar energy and thermal radiation from the planet's surface. The troposphere contains 99% of the water vapor in the atmosphere which vapor concentrations vary with latitudinal

position (north to south) exhibiting greatest values above the tropical regions, and decrease toward the polar regions.

The differential heating of the regions of the troposphere by the sun causes convection currents, large-scale patterns of winds that transport heat and moisture around the globe lead to different kinds of wave formation in the troposphere. In the Northern and Southern hemispheres, air rises along the equator and subpolar climatic regions and sinks in the polar and subtropical regions. Air is deflected by the Earth's rotation as it moves between the poles and equator, creating belts of surface winds moving from east to west (westward winds) in tropical and polar regions, the winds moving from west to east (eastward winds) in the middle latitudes. This global circulation is disrupted by the circular wind patterns of migrating high and low air pressure areas, and by locally abrupt changes in wind speed and direction known as instability. The troposphere is therefore a rich source of convection of vertically propagating perturbations, which can significantly modify the structure and dynamics of the other atmospheric regions. Atmospheric waves, generated from tropospheric sources, propagate upwards into the rarified upper atmosphere, where wave amplitudes increase with height as the background density decreases. The troposphere is bounded at the top by the tropopause.

Stratosphere: It is the second layer of the Earth's atmosphere, and it starts at an altitude around 15 km and extends up to 50 km. It is so named because the stratified layers within it have a temperature profile that increases with altitude (MOHANNAKUMAR, 2008). Due to variations in solar heating, the base of the stratosphere varies with latitude and the seasons. Throughout the stratospheric region, the atmospheric temperature increases with altitude up to about 270 K at around 50 km. This temperature reversal (inversion) is caused by the ozone layer (O_3), which resides in the stratosphere (peak at 30 km) and absorbs incident solar ultraviolet radiation, which is the primary source of heating in the region. Various types of waves, such as atmospheric gravity waves and tides

carry energy from the troposphere upward into the stratosphere and transmit energy from this region up into the layer above it. The waves and tides influence the flows of air and can cause regional heating in the stratosphere. The stratospheric layer is bounded at the top by the stratopause.

Mesosphere is a layer that extends from 50 to 80 km and characterized by decrease in temperature with increasing altitude. The region is considered to be the coldest region of Earth's atmosphere reaching a minimum of ~180 K at 80 km altitude. The gravity waves, planetary waves and tides carry energy and transfer momentum from the stratosphere upward into the mesosphere and are sometime trapped in the mesopause. The dynamical processes of waves and their upward transport of momentum influence the mesospheric temperature. The chemical compositions are fairly uniform and pressures become very low. This layer is bounded at the top by the mesopause.

Thermosphere is a region of high temperature and very low density. Thermospheric temperature increases rapidly in the lower thermosphere (up to ~1000 K), and then remains fairly steady with increasing altitude. Temperatures in the upper thermosphere can range from 1000 K to1500 K or more, depending on the solar activity. The higher temperature found in the thermosphere is caused by the absorption of solar ultraviolet (UV) radiation by atomic oxygen and nitrogen, which is a major heating mechanism in the thermosphere. Overall circulation in this region are driven largely by the atmospheric tides, gravity waves and neutral winds. The neutral thermosphere overlaps in altitude with the ionosphere which extends from ~90 km up to about 1000 km. Energetic ultraviolet and X-ray photons break electrons away from gas particles in the thermosphere, creating electrically charged ions of atoms and molecules. Neutral winds cause moving ions to drag along by collisions with the electrically neutral gases, which results in production of strong electrical currents. The thermopause is the level at which the temperature stops rising with height which depend on the solar activity.

1.2 Composition of the Ionosphere

The Ionosphere is a part of the atmosphere that is partially ionized mainly due to the photoionization by the solar radiation (RISHBETH; GARRIOTT, 1969; KELLEY, 2008). The layer is stratified along the vertical distance in three main layers D, E, and F. The stratification of these layers depends on the relative density of charge particles, the unique characteristics and the behavior of the charged particles in each layer. The characteristics and formation of each of the regions are discussed below:

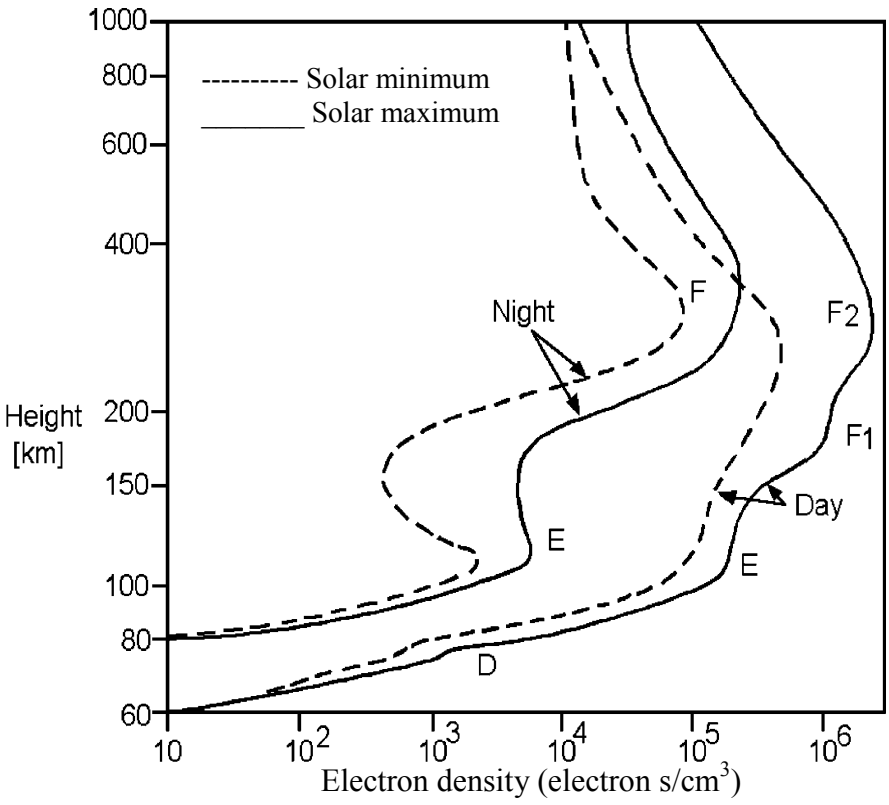

Figure 1.2 - Vertical profile of the ionosphere

Source: Hargreaves (1992).

D Layer: Located at the bottom of the ionosphere up to ~ 90 km height. This region presents a complexity in chemical and photochemical processes which may be characterized by low density and high ionization collisions frequency of electrons with ions and neutral particles. There are three ionization sources in this region, these being X-rays, cosmic rays and Lyman-α radiation, which ionize only nitric oxide (NO). The chemical processes present in this region are quite complex and involve O, O_2, O_3, NO, NO_2, CO_2, H_2O and alkali metals. The ionization of this region is however very low ranging from 10^7 to 10^{10} e/m^3 and as a result the HF radio waves are not reflected by this region which is then mainly responsible for absorption of high-frequency radio waves. When a radio wave enters the ionosphere, the free electrons are set into motion by the alternating electric field on the wave. The energy that is transferred from the wave to the free electrons is lost when the electrons collide with molecules. Therefore the greatest energy loss is in the D region, where the quantity $N\nu$ (N is the electron density, and ν is the collision frequency between electrons and neutral molecules to which the absorption loss is proportional) reaches its maximum value.

E Layer: Situated between 90-140 km high, is characterized by increased electron density between 90 and 110 km. This region of high conductivity is very important due to the presence of ionospheric electrical currents and the interaction of these currents with the Earth's magnetic field. The main sources of ionization are weak X-rays (λ> 10 Å) radiation, solar Lyman-β (1025.7 Å) and EUV (<1000 Å) ionizing the O_2, EUV (<900 Å) ionizing the N_2. Within this region, due to different mechanisms, highly variable dense and thin layers (whose thickness varies from 0.2 to 2 km), called E sporadic (Es) layers, may develop. At mid- and low-latitudes the probability of occurrence of these Es layers is major during the summer daytime hours, while at high-latitudes the probability of occurrence is more pronounced at nighttime hours.

F Layer: It is located approximately between 150-1000 km height. Its main sources of the ionization are Extreme Ultraviolet Radiation (EUV) lines and Lyman continuum of hydrogen. The dominant ion is O^+. The F region can be characterized by two other layers, F1 and F2 as shown in Figure 1.2. In the equatorial region may create a third layer, named F3. The F1 layer is defined based on an inflection or a peak in the curve electron density around 180 km. It is in this region that the transition between the processes of linear and quadratic loss occurs. The F2 layer is located in vicinity of the peak electron density (~ 300-400 km), and it is the region with higher ionization density of the ionosphere. Its formation is predominantly dependent of the winds and its concentration varies with solar activity. The highest concentration of free electrons can be observed during the day, especially during local noon. During the night, this concentration decreases, but the layer remains due to low recombination of ion with neutral and wind transport effects. The equatorial meridional wind plays an important role in the nighttime F layer density maintenance. The free electrons and ions generated by various wind and tidal forces are the main causes for the both electrical and thermal conductivity of the ionosphere.

1.3 Dynamic processes and transport in the ionosphere

The E and F regions of the ionosphere are characterized by robust dynamical processes, owing to variety of forces such as pressure, gravity, electric and magnetic field, as well as forces generated by ions/electrons collisions with neutral particles. These forces are characterized by the ratio $k = \Omega/\nu$ (Ω is the plasma gyrofrequency and ν is the collision frequency). The E and F regions are classified on the basis of k_i and k_e. In the E and F regions, $k_i \ll 1$ and $k_i \geqslant 1$ respectively, while $k_e \gg 1$ in both regions. The different nature of k_i is responsible for the different kind of dynamics in the E and F regions.

As the descriptions of the development of MSTIDs are dependent on knowledge of the conductivity and ion velocity in the ionosphere, it is important to discuss the governing equations that describe these dynamical processes in the ionosphere. The first governing equation is the ion continuity equation. Following Kherani et al. (2012) and assuming no production or loss, the equation can be written as:

$$\frac{\partial}{\partial t} n_i + \nabla \cdot \left(n_i \vec{V}_i \right) = 0 \quad , \tag{1.1}$$

where, n_i is the ion density, and $\vec{V}_i$ is the ion velocity. Equation 1.1 states that the density must be conserved in the system. i.e. the time rate of change for the number of particles must be accounted for by velocities of the particles.

At higher altitudes (above 150 km), the ions gyrofrequency becomes prevalent and diffusion processes also have great importance in the dynamics of the ionosphere. This brings us to the next governing equation, which is the momentum of the particles (called the momentum equation). It can be described as:

$$m\frac{d\vec{V}}{dt} = m\vec{g} - \frac{m}{\rho_{i,e}} \nabla p_{i,e} + q[\vec{E} + (\vec{V} \times \vec{B})] - m\nu_{in,en}(\vec{V} - \vec{U}) - m\eta\vec{\nabla}^2\vec{V} \tag{1.2}$$

In equation 1.2 m is the mass of the ions, $\rho_{i,e}$ and $p_{i,e}$ are the density and pressure related to the species considered, ν_{in}, ν_{en} and ν_{ii} represent the ion-neutral, electron-neutral, and ion-ion collision frequencies, respectively, $\vec{V}$ is the ion velocity, $\vec{U}$ is velocity of neutral wind, η is the dynamic viscosity coefficient, $\vec{g}$ is the force of gravity, $\vec{E}$ is the electric field and $\vec{B}$ is the magnetic field induction. This momentum equation is used to solve for ion and electron velocities in two models used in this thesis.

Equation 1.2 conserves momentum in the system. The momentum generated by the forces caused by gravity, pressure, electric and magnetic fields, friction (ion drag) and viscosity force, must sum to zero with respect to each constituent (both the ions and electrons) in the large scale movement.

Fundamentally, charge neutrality is an important condition for the ionosphere due to the constraint that the number of ions must equal the number of electrons. Hence the last governing equation is the divergence-free condition:

$$\nabla \cdot \vec{J} = 0 \tag{1.3}$$

This equation is based on the charge neutrality assumption and can be derived from Maxwell's equations. The current divergent free equation is important for the simulation of MSTIDs. Without this condition, the polarization electric fields are not created and sustained, and thus the instabilities would not be formed. (i.e. polarization electric field is develop to maintain current divergent free)

1.4 Altitude Variation of Conductivity

Conductivity in general term is the measure of a material's ability to conduct an electric current. In the upper atmosphere, conductivity depends on the electron concentration and the relative amplitude between collision frequency and gyrofrequency around magnetic field. Conductivity affects the development of electric fields and how current flows. It is therefore an important concept in understanding ionospheric electrodynamics. The ionospheric conductivity depends on various parameters such as location, time, season and solar activity. There are three types of conductivity: Parallel conductivity which is in the direction parallel to the magnetic field line and denoted as "σ_0", Pedersen conductivity which is in the direction perpendicular to the magnetic field and parallel to the electric field - it is denoted as "σ_P", and Hall conductivity in the

direction perpendicular to both the magnetic and electric fields. It is denoted as "σ_H".

Under the action of external forces e.g. electric field $\vec{E}$ and the wind-drag force $\vec{W}$ associated with tides, the ion/electron collisions with neutrals (plasma velocity) and current density of the ionospheric plasma, are given by following expressions:

$$\vec{u} = \tilde{\mu} \cdot \vec{F}; \qquad \vec{j} = \tilde{\sigma} \cdot \vec{F} \qquad \vec{F} = \vec{E} + \vec{W} \times \vec{B}_o, \tag{1.4}$$

where $\tilde{\mu}$ and $\tilde{\sigma}$ are the mobility and conductivity tensors, given by the following expressions:

$$\tilde{\mu} = \begin{pmatrix} \mu_P & -\mu_H & 0 \\ \mu_H & \mu_P & 0 \\ 0 & 0 & \mu_0 \end{pmatrix} \quad \tilde{\sigma} = \begin{pmatrix} \sigma_P & -\sigma_H & 0 \\ \sigma_H & \sigma_P & 0 \\ 0 & 0 & \sigma_0 \end{pmatrix}, \tag{1.5}$$

where $(\mu_P,\ \mu_H,\ \mu_0)$ are the Pedersen, Hall and parallel mobilities and (σ_P, σ_H, σ_0) are the Pedersen, Hall and parallel conductivities by charge unity respectively. They are given by following expressions:

Mobility:

$$\begin{aligned} \mu_P &= k \Big/ B_o\left(1+\kappa^2\right) \\ \mu_H &= \kappa\mu_P; \\ \mu_o &= \left(1+\kappa^2\right)\mu_P; \end{aligned} \tag{1.6}$$

Conductivity:

$$\begin{aligned} \sigma_P &= \frac{ne}{B}\left[\frac{k_i}{1+\kappa_i^2} - \frac{k_e}{1+\kappa_e^2}\right], \\ \sigma_H &= \frac{ne}{B}\left[\frac{\kappa_e^2}{1+\kappa_e^2} - \frac{\kappa_i^2}{1+\kappa_i^2}\right], \\ \sigma_0 &= \frac{ne}{B}\left[k_i - k_e\right], \end{aligned} \tag{1.7}$$

where n is the ionospheric density, and (μ_i ,μ_e) are ion and electron mobilities respectively, k has been described in section 1.3. In terms of these mobilities and conductivities, the velocity and currents can be written in the following form:

$$\vec{u} = \mu_P \vec{E}_\perp + \mu_H \vec{E}_\perp \times \hat{b} + \mu_o \vec{E}_\parallel \tag{1.8}$$

$$\vec{j} = \sigma_P \vec{E}_\perp + \sigma_H \vec{E}_\perp \times \hat{b} + \sigma_o \vec{E} \tag{1.9}$$

where ($\perp$, ||) represent the directions perpendicular and parallel to the B_o and $\hat{b}$ is the unit vector along the magnetic field direction.

Equation 1.9 can be modified to include the neutral wind $\vec{U}$, to obtain the effective electric field, $\vec{E}' = \vec{E} + \vec{U} \times \vec{B}$. In this way, the current density equation is expanded as:

$$\vec{J} = \tilde{\sigma} \cdot \vec{E}' \Rightarrow \tilde{\sigma} \cdot \left(\vec{E} + \vec{U} \times \vec{B}\right)$$

Considering each components of conductivity, we have:

$$\vec{J} = \sigma_o \vec{E}' + \sigma_P \left(\vec{E} + \vec{U} \times \vec{B}\right) - \sigma_H \left(\vec{E} + \vec{U} \times \vec{B}\right) \times \hat{b} \tag{1.10}$$

The vertical profiles of these conductivities are presented in Figure 1.3.

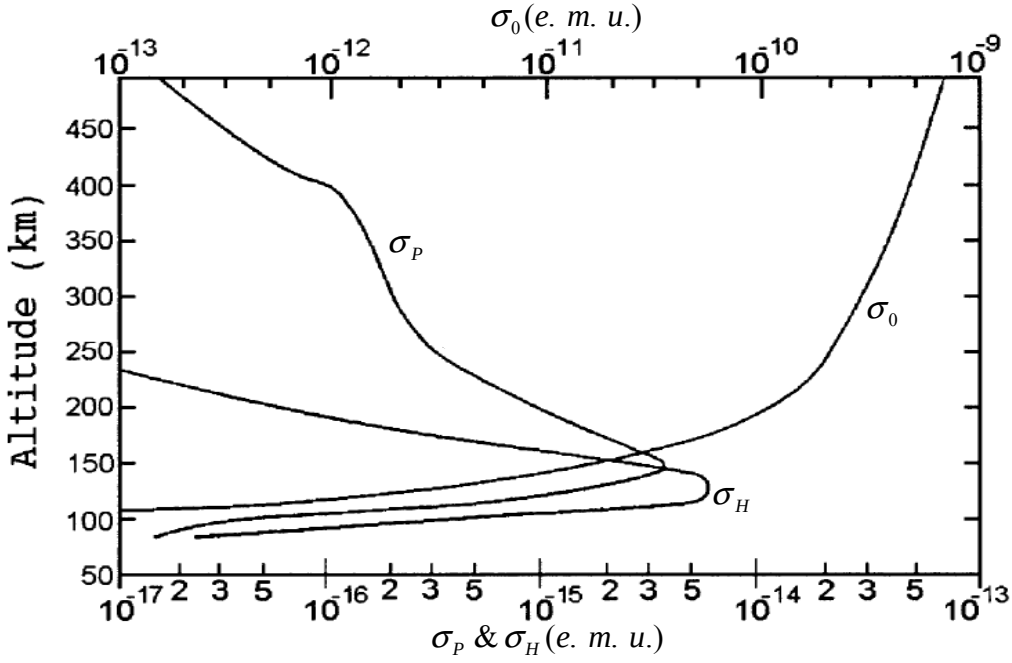

Figure 1.3 - Vertical profile of the Parallel (σ_0), Pedersen (σ_P) and Hall (σ_H) conductivities.
Source: Abdu (2005)

Figure 1.3 also shows Pedersen conductivity peak at around 140 km and the Hall conductivity peak at around 120 km. Their values decrease rapidly above and below these heights. The conductivity parallel to the magnetic field increases substantially with altitude due to decreasing collisions with the neutral gas. The parallel conductivity is always much higher than the conductivity perpendicular to the magnetic field about 150 km.

The movement of a class of charged particles perpendicular to the magnetic fields depends on the ratio of the collision frequency (ν) to the gyrofrequency (Ω). If $\nu >> \Omega$ then collisions prevent the particle from gyrating and the particles move in the direction of the electric field, as a Pedersen current. If, on the other hand, $\nu << \Omega$ then the particles predominantly drift perpendicular to the electric field.

1.5 Aims and Objectives

The present study aims to present the daytime TEC measurements on few chosen geomagnetic quiet days and derive the TEC disturbances as MSTIDs. The adopted methodology dealing with the cross-correlation maps enabled the identifications the MSTIDs from the derived TEC disturbances. The results were compared with relevant literatures over southern hemisphere (HERNANDEZ-PAJARES et al., 2006; 2012) using perturbed GPS-TEC at one New Zealand sector (43.8°S – 43.3°S and 169.5°E – 170.5°E) and MacDougall et al. (2011) using digisonde data over the Brazilian equatorial region and they show good agreement. Furthermore, while daytime MSTIDs are known to be manifestation of AGW in the ionosphere, the sources of this AGW are not yet established. This thesis points out (by using the experimental data provided by GOES and

COSMIC satellite) the tropospheric cloud convection as a principal possible forcing mechanism for AGW causing the observed MSTIDs. On the simulation aspects, Convectional Atmosphere-Ionosphere Coupled model (CAI-CM) (KHERANI et al., 2016) and the SAMI3 numerical models are adapted to incorporate the dynamics of convectively generated AGWs and their coupling to the ionosphere.

1.5.1 Research Questions

This thesis also aims to answer the following research questions:

- Can MSTIDs be observed at the Brazilian sector considering the relatively fewer GPS receiver distributions?
- What are the characteristics of daytime MSTIDs over the Brazilian sector?
- Could AGW through deep convection activities be a principal factor for daytime MSTIDs generation and propagation?
- Is it possible to observe mapping of MSTIDs to conjugate hemisphere during daytime?
- What are the mechanisms responsible for these daytime mappings?

1.6 Scope of the Thesis

The investigations will be carried out under the following outlines:

Chapter 2: Literature review -- A review of the ionospheric research work in the context of this thesis. A brief history of the TIDs followed by their characteristics and causes of the MSTIDs are discussed. The AGW description and generation mechanisms with more emphases on the tropospheric convective mechanism being the principal area of investigation of the thesis.

Chapter 3: The instrumentations and methodology -- The descriptions of the various instruments used in the study are described alongside the data

generated by these instruments. This is followed by the description of the methodology and approach used for the study.

Chapter 4: MSTIDs observations results -- based on the methodology described in chapter 3, Construction of the TEC map and Travel-Time diagram (otherwise known as keogram plots) are presented. Using the statistical analyses described in chapter 3, the MSTIDs propagation observed in the keogram plot are discussed.

Chapter 5: Geomagnetic conjugate observation of daytime MSTIDs -- Results of 4 days of geomagnetic conjugate mapping of MSTIDs are presented and the mechanisms responsible for the daytime MSTIDs mapping are discussed.

Chapter 6: Gravity waves observation and source investigation -- Based on the observations of MSTIDs using primarily the GNSS data, the mechanisms (AGW) responsible for these MSTIDs are investigated by: (1) Identifying GWs signatures from isolines of digisonde, (2) Identifying few tropospheric events based on convection activities (GOES satellite).

Chapter 7: CAI-CM is used as a coupling model to simulate convective induced AGW between troposphere and ionosphere. Two numerical experiments were carried out (1) by using a strong convective forcing and (2) by using a weak convective forcing.

Chapter 8: Simulation studies – SAMI3 numerical model is adapted for the simulation of the observed MSTIDs results. SAMI2 was used as ambient atmosphere input to SAMI3. This chapter explains the coordinate system used in SAMI3 and the physical development of MSTIDs. It also reveals the implementation processes of SAMI3 parallel programing. Finally, the input parameter used and the applied perturbation for the simulation are determined. Finally the results from the two models are compared with the observation results.

Chapter 9: Summary and future direction. This chapter highlights the contributions of the thesis and points out possible areas in which future contribution can be made.

2.0 LITERATURE REVIEW

For proper understanding and insight on recent studies relating to the topic of interest, this chapter gives concrete reviews on properties of day and nighttime MSTIDs as well as basic descriptions of AGW and AGW associated with convective activities.

2.1 Brief Historical Studies of TIDs

Since the 1950s, travelling disturbances called TIDs in the ionospheric plasma have been observed. Based on the work of Hines (1960), it was postulated that gravity waves travelling in the neutral atmosphere caused the TIDs. Hunsuncker (1982) was the first to classify the TIDs into large and medium scale. Since then many simulation and observation studies using different instruments: Incoherent/Coherent Scatter Radar and Airglow Cameras (BEHNKE, 1979, KELLEY AND FUKAO, 1991), digital ionosondes (ABDU et al., 1982, BOWMAN, 1990), optical imager (MENDILLO et al., 1997, GARCIA et al., 2000, CANDIDO et al., 2008, PIMENTA et al., 2008) have been reported. Fukao et al. (1991) investigated the coherent backscatter of 50 MHz radar waves from the mid-latitude F region by using the Japanese MU radar. When the radar was tilted due north in fixed beam mode, they observed intense and turbulent echoes, which were usually from irregular patches, moving upward and away from the radar at Doppler speeds of 100-200 m/s. When the radar was in multiple beam mode, irregular patches were observed to move from east to west at velocities around 150m/s. Further, many RTI (range-time-intensity) plots showed a downward slant which indicated a northwest movement of patches. Kelley and Fukao (1991) compared some instability mechanisms and regarded that Perkins instability was the best one to explain the above coherent radar observations. Kelley (2011) showed five examples of mid-latitude airglow features which were compared with airglow from the magnetic equator. The striking difference is that the mid-latitude features are not aligned with the magnetic meridian and do not move eastward as the equatorward features do, but rather propagate southwestward in the northern hemisphere and

northwestward in the southern hemisphere which is in line with the Perkins theory. Behnke (1979) observed banded structures of raised and lowered F region layer in the ionosphere on five out of eight nights over Arecibo under solar minimum conditions. The structures were aligned with the northwest-southeast direction and propagated to the southwest with height difference of the order of 50 km and phase velocities usually between 13 and 61 m/s. On March 6, 1973, the electric field vector and wave vector were measured with the directions for the former one of 26° north from east and for latter 9° north from east. This configuration had a growth rate very near the maximum growth rate predicted by Perkins.

The Medium-Scale Travelling Ionospheric Disturbances (MSTIDs) observations using Global Navigation Satellite System (GNSS) have also been studied in recent years mainly at the northern hemisphere (e.g. TSUGAWA et al., 2004, 2007, OTSUKA et al., 2004, 2013, etc.) due to densely distribution of the GNSS receivers at this region. Tsugawa et al, (2007) using the GPS-TEC methodology, showed Total Electron Content (TEC) maps for the daytime between 19:20 UT (13:20CST) and 22:00 UT (16:00 CST) on November 28, 2006 over North America where daytime MSTIDs propagate southeastward around mid-day and southwestward in the late afternoon at a velocity of 100 - 200 m/s, with a wavelength of 300 - 1000 km and a peak-to-peak amplitude larger than ~0.5 TEC. Nighttime MSTIDs were also investigated. Following the same methodology above, Otsuka et al, (2013) analyzed the TEC data obtained with the GPS observables over Europe and investigated the time sequence of two-dimensional TEC perturbation during daytime. The TEC perturbation can be seen to have a phase front aligned in the east-west direction and propagate in the equatorward direction, which is in agreement with the Tsugawa et al. (2007).

2.2 What are Travelling Ionospheric Disturbances?

Travelling Ionospheric Disturbances (TIDs) are generally the ionospheric manifestation of gravity waves propagating in the neutral atmosphere, which travel through the ionosphere over very long distance (HINES 1960 and HUNSUNCKER, 1982). They are wavelike perturbation of the ionospheric plasmas that are frequently observed at high and middle latitudes (BRISTOW et al., 1996, OLIVER et al., 1997, and NICOLLS et al., 2005). Their activity and amplitudes vary depending on latitude, longitude, local time, season, and solar cycle (KOTAKE et al., 2006, HERNANDEZ-PAJARES et al., 2006). These ionospheric disturbances are one of the most common ionospheric phenomena that contribute to the perturbations in ionospheric measurements such as Total Electron Content (TEC) and frequency measurements among others, which can be detrimental to radio wave propagation and affect space weather forecast (HERNANDEZ-PAJARES et al., 2006). Large variations in TID characteristics and propagation directions can be generated by very distinct classes of processes, from auroral sources at the high latitude thermosphere to the solar terminator and storms, as well as cloud convection, hurricanes and tornados in the troposphere.

Referring to Hunsuncker (1982), TIDs are classified into two main categories: Large Scale Traveling Ionoshperic Disturbance (LSTID) and Medium-Scale Travelling Ionospheric Disturbance (MSTID). LSTIDs have horizontal wavelength (λ_h), corresponding to λ_h > 1000 km, period of 60 minutes and above, amplitude of 20% of TEC and a propagation velocities of 300 - 1000 m/s in the equatorial direction. They appeared to have geomagnetic dependence with auroral origin. The MSTIDs on the other hand, have horizontal wavelength corresponding to λ_h < 500 km, amplitude of 10% of TEC and a propagating velocities of 50 - 400 m/s with a period of 10 - 60 minutes but they are not geomagnetic disturbance dependent. MSTIDs can also be generally grouped into three main groups: daytime, nighttime and dawn and dusk MSTIDs. The daytime MSTIDs frequently occur in winter solstice and tend to propagate

southeastward in the northern hemisphere while nighttime MSTIDs are more frequent in summer solstices and their direction of propagation is southwestward in northern hemisphere. The dawn and dusk MSTIDs frequently occur in summer and propagate eastward and north-northwestward respectively (OTSUKA et al., 2011). The daytime MSTIDs do not have F region irregularities associated with them while the nighttime is characterized with F region irregularities (OGAWA et al., 2009).

2.3 Characteristics of day and night time MSTIDs

Since the mid-1990s several new characteristics of the MSTIDs have been discovered through the ionospheric observations using various aforementioned instrumental techniques. The characteristics varying from daytime to nighttime are listed in Table 1 below. Although many characteristics have been determined, many more are yet to be discovered. For example, the width of wave fronts and the south and north limit of the wave's propagation. It is interesting to note that, unlike equatorial spread F, the MSTIDs structures are not aligned with the magnetic meridian but are aligned from NW to SE in the northern hemisphere (GARCIA et al., 2000, OTSUKA et al., 2004, 2011, 2013, TSUGAWA et al., 2007) and SW to NE in the southern hemisphere (MARTINIS et al., 2010, PIMENTA et al., 2008 and OTSUKA et al., 2004, 2011, 2013).

Table 2.1. Daytime and nighttime MSTIDs characteristics

S/N	Properties	Daytime MSTIDs	Nighttime MSTIDs
1	Wavelength	300-1000 km	200 – 500 km
2	Wave front	NE – SW (>~2000km) – NH SE – NW (>~2000km) - SH	NW – SE (≤ ~2000km) – NH SW – NE (≤ ~2000km) - SH
3	Period	≤ an hour	≤ an hour
4	Velocity	50 – 300 m/s	50 –200 m/s
5	Direction	Southeastward – NH Northeastward - SH	Southwestward – NH Northwestward - SH
6	Seasonal dependence	Winter solstices	Summer solstices
7	Geomag. activity	Quiet	Disturb
8	F region attribute	No irregularities	irregularities
9	Source	Atmospheric gravity waves	Electrodynamics processes

2.4 Causes of MSTIDS

The different characteristics between daytime and nighttime MSTIDs suggest that the mechanisms causing them could be different between both day and night (KOTAKE et al., 2007). There are substantial indications by Otsuka et al. (2011, 2013) that the daytime and nighttime MSTIDs are primarily generated by atmospheric gravity waves (daytime) and electrodynamics processes involving polarization electric fields (nighttime). The daytime MSTIDs can be created by atmospheric gravity waves from the lower atmosphere (E region), or created in conjunction with auroral activity at the upper atmosphere region (HINES, 1960, HOOKE, 1968, AND HUNSUCKER, 1982). According to Tsugawa et al. (2007), the AGWs can also cause oscillation (growth and damping) of MSTIDs, i.e., if the AGWs propagate with constant amplitude, the total amount of plasma

variation caused by the AGWs could be large at lower latitudes, which could result in latitudinal variation of the MSTIDs amplitudes. However, since geomagnetic inclination angle decreases with decrease in latitude the upward/downward plasma variation along the geomagnetic field lines due to the AGWs decrease. Ion-drag effects can also damp the AGWs during daytime ionosphere. Hence, these two effects imply that, as latitude decreases MSTIDs amplitudes decrease.

Electrical force related to electric field polarization caused by plasma instability has also been suggested to play a main role in the generation of nighttime MSTIDs (SAITO et al., 1998, KELLEY AND MAKELA 2001, SHIOKAWA et al., 2003 and OTSUKA et al., 2004). Otsuka et al., (2004), proposed a hypothesis that electric field is involved in the generation of MSTIDs in both southern and northern hemispheres. This hypothesis was tested by using two all-sky airglow imagers at conjugate points, that are Sata, Japan, in the northern hemisphere and Darwin, Australia, in the southern hemisphere. The airglow imagers were calibrated optically to enable determination of absolute intensity in unity of Rayleigh. They illustrated that the polarization electric field (Ep) should be perpendicular to the wave fronts of MSTIDs, and northeastward in the regions of low airglow intensity and southwestward in the regions of high airglow intensity. It was noted that in the northern hemisphere, the eastward component of Ep in the low airglow intensity region causes northward and upward plasma drift which move the F region plasma to higher altitudes. Therefore, Ep generated in one hemisphere is transmitted along magnetic field lines to the other hemisphere. The observed structure of the OI 630nm airglow perturbation may develop as consequence of an ionospheric instability that acts through electric processes involving electric field. Recent observational and theoretical efforts have shown that AGWs from convective sources in the troposphere can propagate well into the thermosphere before dissipating. Hence, in the section that follows, AGW and it generating mechanisms are discussed as the principal cause of MSTIDs.

2.5 Atmospheric Gravity Waves

Atmospheric Gravity waves (AGW) are the most significant atmospheric wave, which arise due to vertical displacement of the air parcels in stable stratified fluid. AGWs are divided into three groups based on period and wavelength (HUNSUCKER AND HARGREAVES, 2003). The large-scale AGWs have horizontal wavelengths of about 1000 km, their wave periods are more than an hour and horizontal velocities of 250-1000 m/s. The medium-scale AGWs have horizontal wavelengths of several hundred kilometers, wave periods of about 15-70 minutes, and horizontal velocities of about 90-250 m/s. The small-scale AGWs have periods of 2-5 minutes with velocities less than 300 m/s and their wavelengths are less than those of the medium-scale AGWs. Typically, AGWs can, for example, be created by orography (e.g. MCFARLANE, 1987), convection (e.g. LARSEN et al., 1982), strong a diabatic heating (e.g. HOOKE, 1986), jet instability (e.g. UCCELLINI AND KOCH, 1987) or wind shear (e.g. FRITTS, 1982). Gravity waves are fundamental dynamical phenomenona in a stably-stratified atmosphere. They can affect the ambient flow in a variety of ways, including: induction of clear-air turbulence above convective cloud, tops or near upper-level jets (e.g. PAVELIN *et al*., 2001), contribution of a momentum flux in the middle atmosphere that influences the zonal-mean circulation (e.g. FRITTS AND ALEXANDER, 2003), triggering or modulation of convection (e.g. MARSHAM AND PARKER, 2006).

Atmospheric gravity or inertia-gravity waves are characterized by fluctuations of vertical velocity, horizontal winds, density and temperature, in a stably stratified environment (e.g. HOLTON, 1992). The restoring forces could be due to compression or due to buoyancy. When the restoring mechanism is buoyancy only, they are called pure internal gravity waves or simply gravity waves, while inertia-gravity waves result from a combination of stratification and Coriolis effects. Inertia gravity waves are characterized by horizontal scales greater than a few hundred kilometers and periods greater than a few hours, which is the reason why they are also affected by the coriolis force. These gravity waves generated by various sources in the troposphere could transport and deposit

energy and momentum, and play an important role in determining the momentum and energy budget equations in global models (FRITTS AND ALEXANDER, 2003). Several observational studies have demonstrated that convectively generated gravity waves are ubiquitous (SPIGA et.al., 2008). Thus, understanding wave sources and their generation mechanisms is crucial to successfully modeling the general circulation of the middle atmosphere (YAMAMORI AND SATO, 2005). The AGW is characterized with downward propagation of phase and upward propagation of energy as shown in Figure 2.1. The figure also shows that if the source is below, the amplitude of the AGWs grows exponentially with height in order to maintain a constant energy flux through an atmosphere whose density decreases with height. Particles move in an elliptical trajectory, combining the longitudinal displacement typical of an acoustic wave with the transverse displacement of a gravity wave.

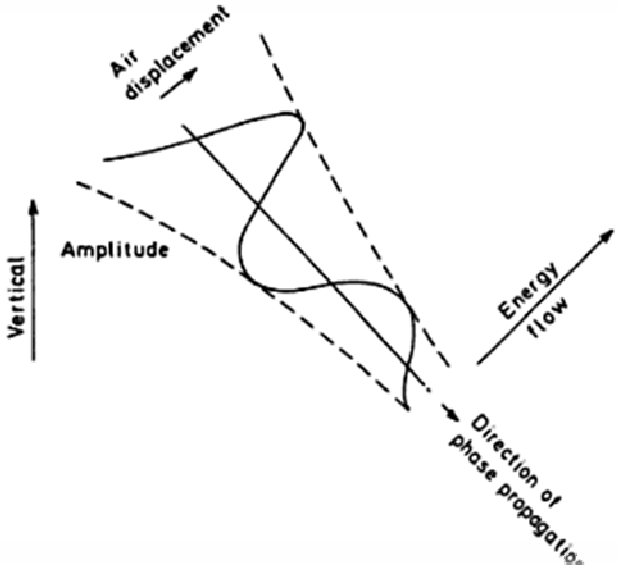

Figure 2.1 - A simple gravity wave showing the energy and phase propagations.
Source: Hargreaves (1992)

In a planar, horizontally stratified, isothermal, single-species, windless, non-rotating atmosphere, the AGW obeys the dispersion relation as give below:

$$\omega^4 = \omega^2 c_s^2 \left(\kappa_y{}^2 + \frac{1}{4H^2} \right) + (\gamma - 1) g^2 \kappa_x^2 = 0 \qquad (2.1)$$

where:

ω is the angular frequency of the wave,

κ_x is the horizontal wave number ($= 2\pi / \lambda_x$)

κ_y is the vertical wave number,

γ is the ratio of specific heats (constant pressure/constant volume),

c_S is the speed of sound ($= \gamma p / \rho$)

H is the vertical scale height of the atmosphere (=RT/g), and

g is the acceleration due to gravity.

This equation states the relation between the frequency and the wavelength (or wave number) in the vertical and the horizontal directions for an AGWs (HUNSUCKER AND HARGREAVES, 2003). Two significant frequencies are the acoustic cut-off frequency and the buoyancy or Brunt-Vaisala frequency, defined as follows:

$$\omega_a = \gamma g / (2c_s), \quad \omega_b = (\gamma - 1)^{1/2} \, g / c_s \qquad (2.2)$$

With these definitions, the dispersion relation may be written as follows:

$$\kappa_y^2 = \left(1 - \frac{\omega_a^2}{\omega^2} \right) \frac{\omega^2}{c_s^2} - \kappa_x^2 \left(1 - \frac{\omega_b^2}{\omega^2} \right)$$

It is clear that to have $\kappa_y^2 > 0$ i.e. for the vertical propagation, wave should have frequency $\omega > \omega_b$ *or* $\omega > \omega_a$. In these frequencies regime, the AGWs become pure gravity and acoustic waves respectively as shown in Figure 2.1a, which illustrates the regimes of AGW in terms of frequency (ω) and the horizontal

wave number (κ_x). Between the acoustic and gravity regimes the waves are evanescent and do not propagate.

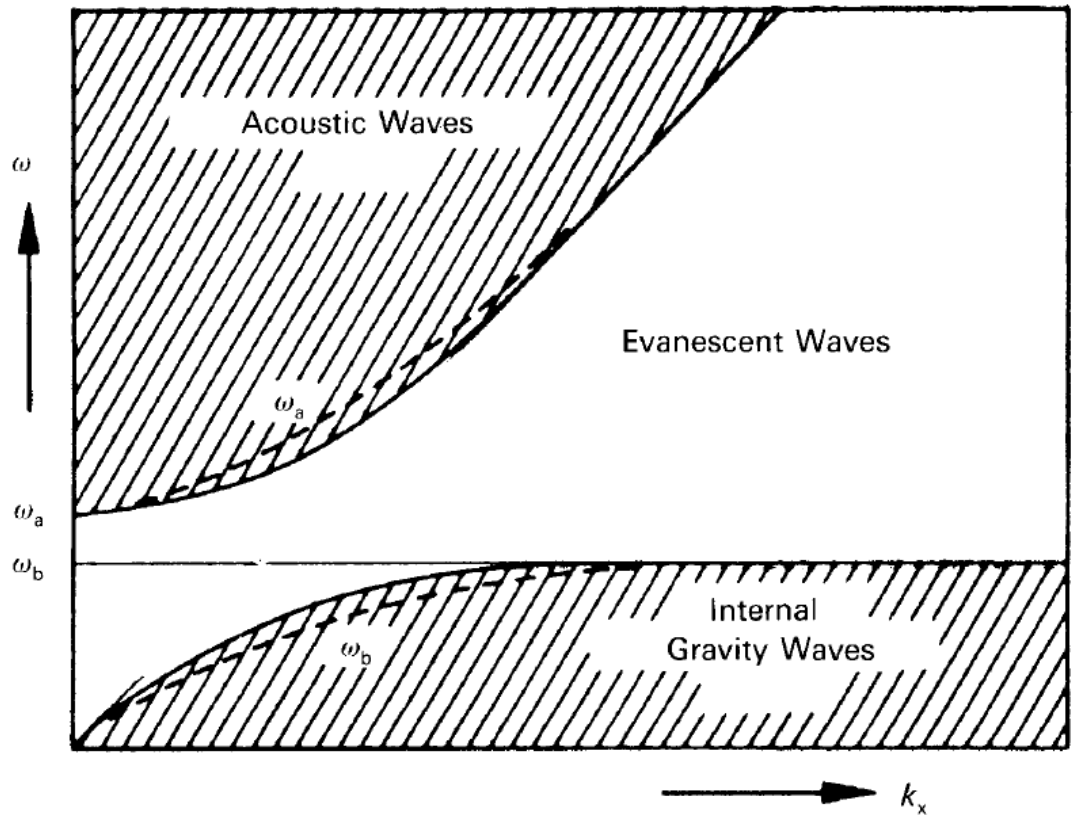

Figure 2.1a - The acoustic, evanescent, and gravity regimes of acoustic-gravity waves. The dashed lines show the effects of neglecting gravity and compressibility, respectively. At ionosphere levels, waves with periods longer than 10 – 15 min are likely gravity waves, while any waves with fewer minutes are probably acoustic gravity waves.
Source: Adapted from Hunsucker and Hargreaves (2003)

The dispersion relation for the pure gravity wave can be obtained under limit $\omega < \omega_b < \kappa_x c_s$ as follows:

$$\kappa_y^2 = -\kappa_x^2\left(1 - \frac{\omega_b^2}{\omega^2}\right) \tag{2.3}$$

The phase and group velocities which states that the group propagation is opposite to the phase propagation are respectively given by the following expressions:

$$\frac{\omega}{\kappa} = \frac{\kappa_x}{\kappa^2}\omega_b; \quad \frac{\partial\omega}{\partial\kappa} = -\frac{\kappa_x}{\kappa^2}\omega_b; \quad \kappa^2 = \kappa_x^2 + \kappa_y^2$$

In real life AGWs can be affected by the following factors: (1) energy loss through the viscosity of the air, (2) non-linear effects if the amplitude becomes too large at the higher altitudes, (3) reflection and ducting due to the change of atmospheric properties with altitude, (4) the curvature of the Earth's surface, and (5) winds.

AGWs play important role in the dynamics of the upper atmosphere because they interact with the ionospheric plasma. AGWs passing through the upper atmosphere leads to changes in the ionospheric plasma and causes wavelike fluctuations of electron density (especially in the F2-region). One of the most important sources of generation of AGWs is likely the deep tropospheric convection. Numerous observational studies have linked AGW activities to tropical convection activities, some of which are discussed in the section that follows.

2.6 Atmospheric Gravity Waves from convective activity

Waves created by convection are as numerous (i.e. with many different scales) as the generation mechanisms (different convective structures or other mechanisms). Convectively-induced waves can, for example, be triggered by the bulk release of latent heat (PIANI et al., 2000), the obstacle effect produced by the convective column on the stratified shear flow above (PFISTER et al., 1993), or the mechanical pump effect due to vertical oscillations of updrafts and downdrafts behaving as an oscillating rigid body (ALEXANDER AND BARNETT, 2007). All three seedings can be coupled, depending strongly upon the local shear and the vertical profile and time dependence of the latent heating (FRITTS AND ALEXANDER, 2003). Atmospheric general circulation

modeling studies (MEDVEDEV et al., 2011; YIGIT et al., 2012) and numerical simulations (VADAS AND FRITTS, 2006) have demonstrated that convectively generated gravity waves can propagate from the lower atmosphere into the thermosphere-ionosphere system. Their wave momenta and energies are deposited at background atmosphere (HORINOUCHI et al., 2002), which has been supposed to be crucial in various aspects of the dynamic and thermal structure of the middle atmosphere. They are not just characterized by a single prominent frequency as in the case for topographic generated waves, instead have wide spectra (e.g. internal gravity waves). The connection between generation of gravity waves and active convection regions have been studied by many authors (e.g., FRITTS et al., 2009, VADAS et al., 2009). Deep clouds near the tropopause region are indicative of active convection regions and a likely source of gravity waves (VADAS et al., 2009). Cold brightness temperature suggests deep convective plumes and convective overshoot which are a convenient launching platform for gravity waves (FRITTS et al., 2009, VADAS et al., 2009). Another clear evidence of gravity waves driven by deep tropospheric convection is given by the work of Shume et al, (2014) as shown in the Figure 2.2 below:

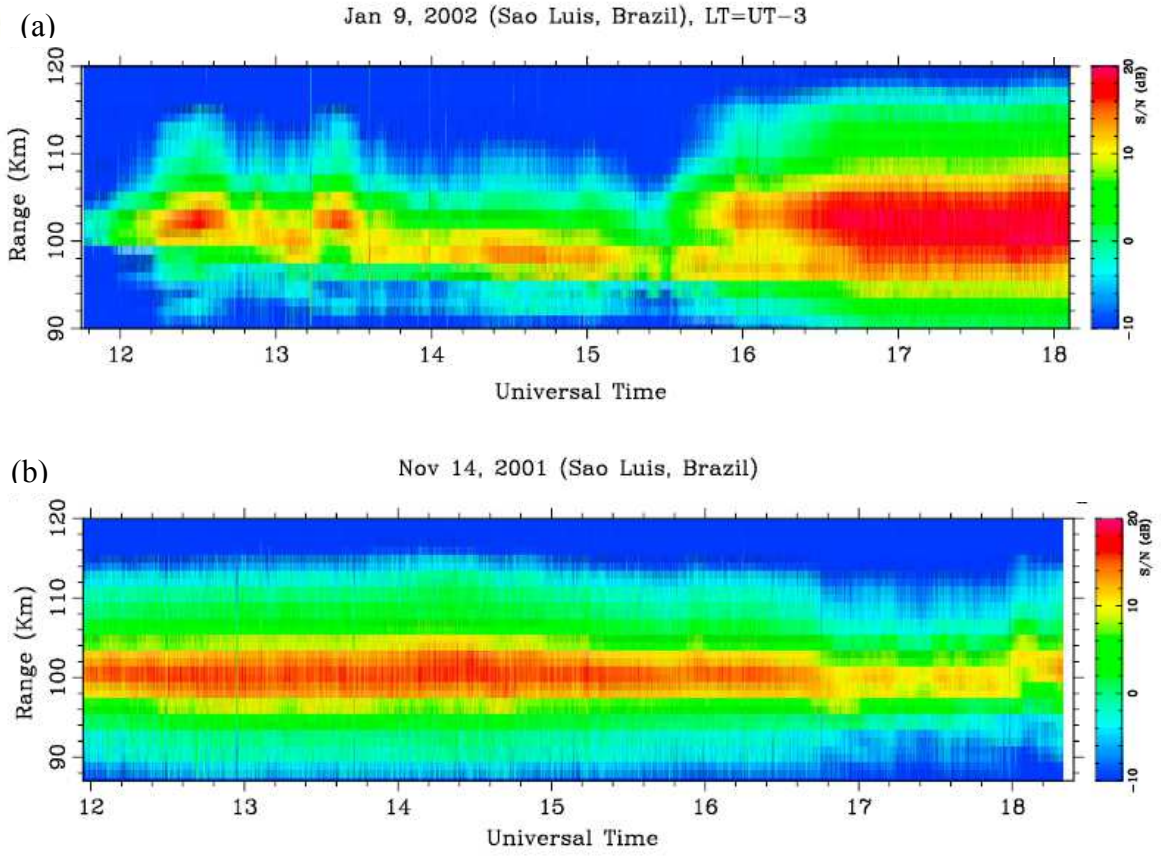

Figure 2.2 - Range time intensity (RTI) representation of coherent scatter from the equatorial electrojet irregularities received by the 30 MHz radar in São Luís on 9 January 2002 (top panel) and 14 November 2001 (bottom panel)
Source: Adapted from Shume et al. (2014)

By using the São Luís 30 MHz radar (Figure 2.2) on 9 January 2002 and 14 November 2001, Shume et al, (2014) observed unusual quasiperiodic fluctuations in the intensity of equatorial electrojet irregularity echoes as a result of tropospheric convective weather condition over the region. A two-dimensional decomposition of Δ*H* (H is the horizontal component of magnetic field) over São Luís, which shows short-period waves, 20 to 60 min (9 January) and 20 to 40 min (14 November) Figure 2.2. From their investigation they proved that gravity waves driven by active tropospheric convection could be coupled to the electrojet and modulate the *E* region electric field thereby causing the

fluctuating radar echoes and the Δ*H* oscillations observed on 9 January and 14 November as shown in the Figure 2.2.

3.0 INSTRUMENTATION AND METHODOLOGY

This chapter describes the various instruments used in the study, such as the Global Navigation Satellite System, the digisonde and the constellation of satellite system from COSMIC mission. The data generated by these instruments are also discussed. This is followed by the methodology and approach used for the study. For example, the estimation of detrended TEC and generation of cross-correlation maps, in addition to the determination of convectional and non-convectional approach and the statistical method used.

3.1 Instrumentation

3.1.1 Global Navigation Satellite System (GNSS)

The GNSS is a constellation of satellites which provides global coverage of signals from space transmitting positioning and timing data. Examples of GNSS are the USA's NAVSTAR Global Positioning System (GPS), Russia's Global Navigation Satellite System (GLONASS), and the new Europe's Galileo system. The accuracy and integrity of GNSS can be greatly enhanced by the use of augmentation information derived from various sources such as: Space Based Augmentation Systems (SBAS) (for example the European Geostationary Navigation Overlay Service (EGNOS) in Europe and Asia, Wide Area Augmentation System (WAAS) in USA, Multi-functional Satellite Augmentation System (MSAS) in Japan, as well as the GPS Aided Geo Augmented Navigation (GAGAN) system in India). The Global Positioning System is the most used in this study and is described below:

The GPS ("Global Positioning System") is a positioning and navigation system satellite in real time, conceived by the United States Department of Defense's America (DoD - "Department of Defense") in the early 1960. Under the name NAVSTAR-GPS project ("Navigation Satellite with Time and Ranging"), the system GPS was declared fully operational in 1995. Being a system with overall coverage, a GPS user can determine its position and its velocity in three dimensions - latitude, longitude and altitude - at any point on or near the

terrestrial surface. The GPS consists of a constellation of 29 satellites network orbiting the earth twice a day at an altitude of approximately 20,200 km with respect to the Earth's surface and emit simultaneously radio signals encoded. The satellites are distributed in six orbital planes inclined at 55 in relation to the geographic equator and equally spaced at 60°, with four satellites in each plan. The orbital period is approximately 12 hours sidereal. This setting ensures global coverage for 24 hours with a visibility at least 4 satellites, minimum number of satellites for navigation and timing.

3.1.1.2 GPS Signals Structure

All GPS satellites transmit the same L1 and L2 carrier frequencies. The code modulation (Figure 2.3), however is different for each satellite. The fundamental frequency is 10.23MHz. Two carrier signals are created from this signal by multiplying the frequency and wavelength (frequency of 1575.42 MHz and wavelength of 19.0 cm,) by 154 for the L1, and by 120 for the L2 (frequency of 1227.60 MHz and wavelength of 24.4 cm) (BLEWITT, 1997). The binary digits 0 and 1 are actually represented by multiplying the electrical signal by either +1 or -1, which is equivalent to leaving the signal unchanged, or flipping the phase by 180^{o} when the code value changes from zero to one or from one to zero.

Information is encoded in the form of binary bits on the carrier signals by a process known as phase modulation. There are three types of code on the carrier signals:

· The C/A code

· The P code

· The Navigation Message

The C/A ("course acquisition") code can be found on the L1 channels. This is a code sequence which repeats every 1 millisecond. It is a pseudo-random code that appears to be random and generated by a known algorithm. The carrier can transmit the C/A code at 1.023 Mbps (million bits per second). The "chip length", or physical distance between binary transitions (i.e. between digits

+1 and -1), is 293 meters. The basic information that the C/A code contains is the time according to the satellite clock and when the time of the signal was transmitted by the satellite. Each satellite has a different C/A code, so that they can be uniquely identified. The C/A code range measurement is relatively less precise compared with that of the P-code. It is, however, less complex and available to all users. It is important to mention that there are new Modern global positioning system signals of L2C and L5 for civilian purpose which have a new developmental prospect. The principal objective of modernizing GPS signal is to improve the overall performance of the GPS system, in terms of improving the accuracy, providing better immunity to RF interference and multipath and better atmospheric corrections. (interested readers are referred to the second edition of Galera, 2008)

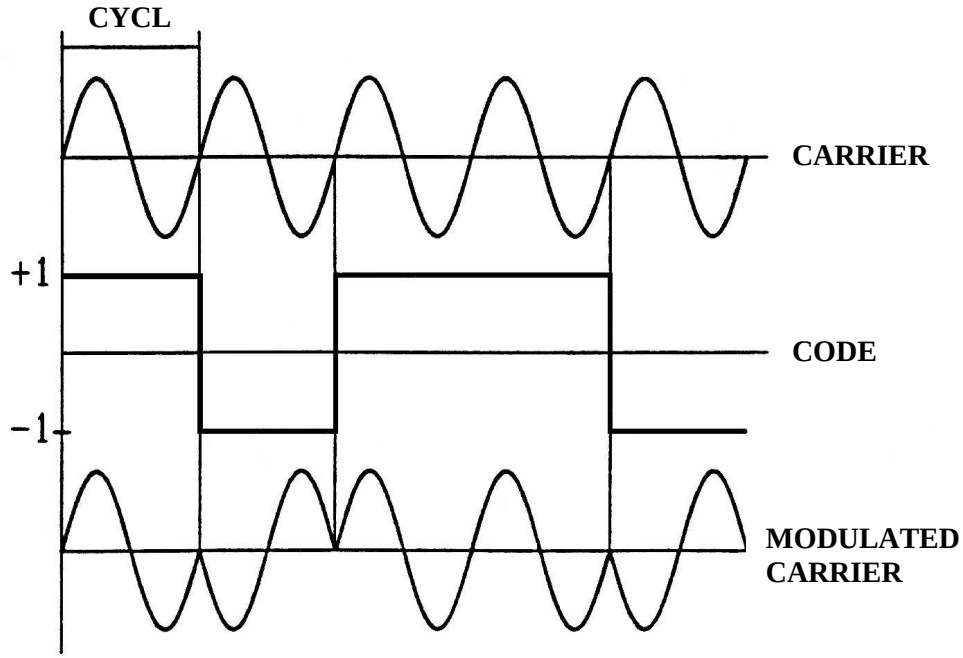

Figure 2.3 - Modulation of the code on the carrier wave.
SOURCE: Hofmann-Wellenhof et al. (1994)

The P (“precise”) code is identical on both the L1 and L2 channel. P code is better for more precise positioning. The P code repeats every 267 days. In practice, this code is divided into 28 day segments where each 7days long is designated a “PRN” number, and is designated to one of the GPS satellites. That is, each satellite transmits a unique 1 week segment of the P-code, which is initialized every 7th day at midnight. The carrier can transmit the P code at 10.23 Mbps, with a chip length of 29.3 meters. The basic information is the satellite clock time which is identical to the C/A information, except that it has ten times the resolution. Unlike the C/A code, the P code can be encrypted with W-code by a process known as “anti-spoofing”(A/S) and the resulting code is denoted by Y-code. Thus, when A/S is activated, the P-code on L1 and L2 carrier is replaced by Y code which in turn cause accuracy denial for civilian users (HOFFMANN-WELLENHOF et al., 1994). Originally the encryption was intended as a means to safeguarding the signal from being corrupted by interference or falsified signals with the GPS signature. Similarly, selective availability (S/A) is a kind of accuracy denial. It is a type of international error imposed on GPS signal. In the presence of S/A, the GPS user may account for position error of up to 100meters (BLEWITT, 1997). S/A is either turned 'on' or turned 'off''. However, when turned 'on' it could be mitigated by differential GPS, where errors in the GPS signal can be computed at a reference station at known coordinates.

The Navigation Message can be found on the L1 channel, being transmitted at a very slow rate of 50 bps. It is a 1500-bit sequence, and therefore it takes 30 seconds to transmit. The Navigation Message includes information on the Broadcast Ephemeris (satellite orbital parameters), satellite clock corrections, almanac data (a crude ephemeris for all satellites), ionosphere information, and satellite health status.

Pseudorandom Code: GPS receivers antenna calculate distances to satellites antenna as a function of the amount of time it takes for satellites' signals to

reach the ground. To make such a calculation, the receiver must be able to tell precisely when the signal was transmitted, and when it was received. The satellites are equipped with extremely accurate atomic clocks, as a result, the timing of transmissions is always known. Receivers contain cheaper clocks, which tend to be sources of measurement error. The signals broadcast by satellites, which are known as "pseudo-random codes," are accompanied by the broadcast ephemeris data that describe the shapes of satellite orbits.

3.1.1.3 The Effects of the Ionosphere on the GPS Signals

The free electrons in the ionosphere, as discussed in section 2, affect the propagation of radio waves. At frequencies below about 30MHz, the ionosphere acts almost like a mirror, changing the path traveled by radio wave back towards the Earth, thereby allowing long-distance communication. However at higher frequencies, such as those used by the GPS, radio waves could pass through the ionosphere but are affected (slow down) by it.

The speed of propagation of radio wave at some point in the ionosphere is determined by the electron density present. The phase of the carrier speed is actually increased by the presence of the electrons. The greater the density of the electrons, the greater is the speed of the carrier phase. The overall effects on a radio wave are obtained by integrating the electron density along the whole path that a signal follows from a satellite to a receiver. The result is that a particular phase of the carrier arrives at the receiver earlier than it would have, had the signal traveled from the satellite in a complete vacuum. This early arrival is known as phase advance. On the other hand, the modulating signal of the carrier (the pseudorandom noise codes and navigation message) is delayed by the ionosphere which increases the apparent length of the path travelled by the signal. The delay of the modulation is called the group delay. The size (error) of the phase advance and the group delay are equal in magnitude and opposite in signs. Both are proportional to the TEC and inversely proportional to

square of the carrier frequency. The higher the frequency the smaller is the effect.

In this thesis GPS data are used to obtain detrended TEC and consequently the MSTIDs signature. The description of this methodology is explained in section 3.2. The GPS data are obtained from Scripts and Permanent Array Centre Garner GPS archive (SOPAC) and Brazilian Network for Continuous Monitoring of the Institute of Brazilian Geography and Statistics (RBMC/IBGE). The data are available at ftp://garner.ucsd.edu/pub/rinex/ and ftp://geoftp.ibge.gov.br/RBMC/dados/, respectively. The distribution of the GNSS receivers is given by yellow circles as represented in Figure 3.3.

3.1.2 The Ionogram

Ionosonde is the most widely used technique in ionospheric research. The first ionosondes were developed based on experiments of Breit and Tuve (1925), which proved the existence of an atmospheric layer ionized by receiving the ionospheric echoes with high frequency electromagnetic pulses.

Ionosondes function by emitting high frequency radio waves, sweeping from lower frequency to the higher, to measure the time required for the signal to travel and return from the refracting ionospheric layer. Radio frequency pulse travels more slowly (group velocity) in the ionosphere than in free space, therefore the virtual height is recorded instead of the true height. For frequencies approaching the maximum plasma frequency in a particular layer, the virtual height tends to become infinity because the wave has to travel a finite distance at effectively zero speed.

Ionograms can provide the relationship between the radio wave frequency and virtual height of the reflecting ionospheric layer. From the ionograms, the characteristic values of virtual heights: virtual height of E region (h_vE), virtual height of F1 region (h_vF1) and virtual of F2 region (h_vF2) and critical

(penetration) frequencies: critical frequency of E region (foE), critical frequency of F1 region (foF1) and critical frequency of F2 region (foF2) can be scaled manually or digitally. Modern ionosondes (digisondes) routinely scale ionograms in digital format and are endowed with greater diagnostic capabilities of the ionosphere due to further technological development. The equipment is used to directly measure the time *t*, at which the pulse radio wave takes to reach the ionosphere and return as a function of frequency. This time can be used to calculate the virtual heights of the ionosphere (Davies, 1965), by the expression:

$$h_v = \frac{1}{2}ct, \tag{3.1}$$

where c is the speed of electromagnetic wave in vacuum.

The transmitting antenna sends electromagnetic pulses in the form of radio waves, vertically propagating in the ionosphere and is reflected after reaching a height where the reflection conditions in a plasma under the action of a magnetic field are met. The reflected echoes are received by a receiver antenna. The principle of operation due to the ionosondes refraction and reflection phenomena of radio waves in the ionosphere can be described as follows: Disregarding the collisions between electrons and neutral particles and the geomagnetic field, the ionospheric refraction index of plasma can be obtained as follows:

$$\mu^2 = 1 - X = 1 - \left[\frac{f_N}{f}\right]^2,$$
$$f_N^2 = \frac{n_e e^2}{4\pi^2 \varepsilon_o m}, \tag{3.2}$$

where n_e is the electron density, and e is the electron charge, ε_o is the electric permittivity in vacuum, m is the electron mass, f_N denotes the frequency of the

plasma, *f* is the frequency of the wave, and *X* denotes the ratio of the frequency of the square natural plasma and the frequency of the radio wave incident on the ionosphere.

In the neutral atmosphere, where *n* is zero, the refractive index is equal to unity *(μ = 1),* therefore, *X = 0*. However, from the source of the ionized layers, where $n_e \neq 0$ due to the presence of free electrons, *X > 0,* the refractive index tends to become lower with the increase in electron density. As the plasma frequency increases with height at the point where the wave frequency to match the plasma frequency $(f^2_N = f^2)$, the refractive index is equal to zero, thereby causing the reflection of the incident radio wave. In this situation it is possible to establish a relationship between the frequency of the incident wave (or frequency plasma) with the ionosphere electron density according to the equation:

$$f_N^2 = f^2,$$

Substituting the constant values, we have:

$$f = (80.5 n_e)^{1/2}, \tag{3.3}$$

where n_e is in *electron/m*^{3} and *f* is in *Hz, o*r it is possible to write in a more usual unit, i.e. electronic density as a function of frequency:

$$n_e = (1.24 \times 10^4) f^2,$$

Where n_e is in *electron/cm*^{3} and *f* is in *MHz.*

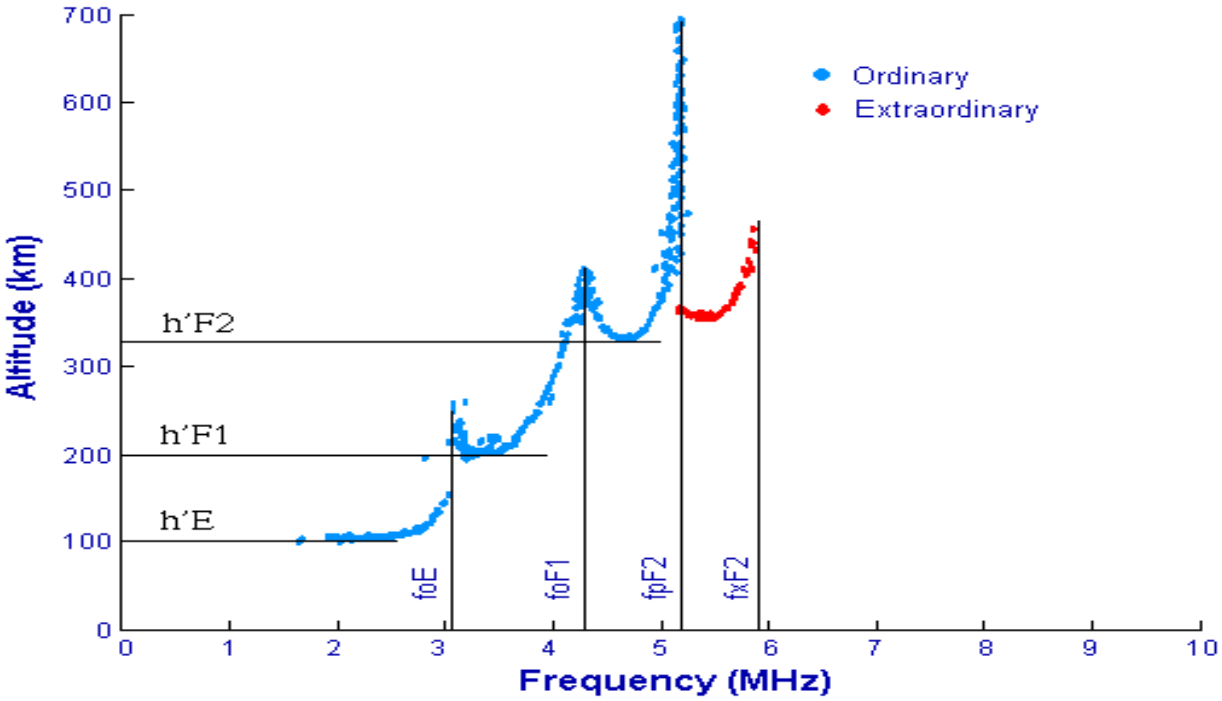

Figure 3.2 - Sample of ionosonde data.

Figure 3.2 is an example of ionogram. The radio wave frequency is plotted against the virtual height of the reflecting layer. It is possible to see that the virtual height steadily increases with the frequency up to the critical frequency. In Figure 3.2, the critical frequencies foE, foF1, and foF2 can be obtained by taking a frequency reading when the virtual height has a local minimum (foE, foF1) or when it tends to approach infinity (foF2). The figure shows clearly, two curves representing the ordinary (blue) and extraordinary waves (red). The curve with the higher critical frequency fxF2 is the extraordinary wave. More discussion on ionogram can be found in Davies, (1965).

The Digisonde data are used in this study to investigate the AGW signature during the observed MSTIDs propagation in order to verify the downward phase motion of two frequencies (LANCHESTER et al., 1993). The data were provided by the National Institute for Space Research (INPE). The positions of the digisondes are shown by red circles at Figure 3.3.

3.1.3 Satellite data from COSMIC

The FORMOSA Satellite Series No. 3/Constellation Observing System for Meteorology, Ionosphere and Climate (FORMOSAT-3/COSMIC) spacecraft constellation consisting of six low-earth-orbiting satellites is the world's first operational constellation system of six low-earth-orbiting (LEO) microsatellites assigned mainly for the Global Positioning System Radio Occultation (GPS RO) remote sensing of the atmosphere and ionosphere at various altitudes with global coverage. The primary scientific goal is to demonstrate the value of near-real-time GPS RO observation in operational numerical weather prediction. The mission provides about 2500 soundings per day in near-real-time vertical profiles of temperature, pressure, refractivity, and water vapor in neutral atmosphere, and electron density in the ionosphere (KUO, et al. 2004, WU, et al. 2006). These data are also valuable for the evaluation of ionospheric models and the use in space weather data assimilation systems (ANTHES, et al. 2008).

3.1.3.1 Scientific COSMIC data processing

The COSMIC Data Analysis and Archival Center (CDAAC) at the University Corporation for Atmospheric Research (UCAR) of the United States of America processes COSMIC data in near real time for operational weather centers and the research community. The CDAAC also reprocesses RO data in a more accurate post-processed mode (within 6 weeks of observation) for COSMIC and other missions such as: GPS/MET, CHAMP, SAC-C, GRACE, TerraSAR-X, and METOP/GRAS. The data processing at the CDAAC includes: GPS site coordinate and ZTD (Zenith Tropospheric Delay) estimation for a global ground-based reference network, high-rate (30 s) GPS satellite clock estimation, LEO precision orbit determination, computation of L1 and L2 atmospheric excess phases, retrieval of neutral atmospheric bending angles and refractivity for each LEO occultation event, estimation of absolute TEC (Total Electron Content), and retrieval of electron density profiles. The CDAAC also provides COSMIC TIP calibrated radiance products. All COSMIC products are made available freely at http://www.cosmic.ucar.edu/.

In this study, the COSMIC data is used to obtain the temperature profile. By using the methodology described in section 3.2 we are able to observe some characteristics of AGW during the MSTIDs event days.

Throughout the period of study the Kp index of < 3 was used to specify the geomagnetic condition. The data were obtained from the Data Analysis Center for Geomagnetism and Space Magnetism at World Data Center for Geomagnetism, Kyoto data base (http://wdc.kugi.kyoto-u.ac.jp/index.html).

3.2 Methodology

3.2.1 Estimation of Detrended TEC and corresponding correlation maps

The background ionospheric variations can be removed from the measured TEC in different ways. For instance (HERNANDEZ-PAJARES et al., 2006) makes this detrending by subtracting from each value an average value of the previous and a posterior measurements. In Tsugawa et al. (2004), detrending was carried out by looking for vertical TEC perturbations from a dense GPS network that is not applicable for a single-receiver measurement. Other methods use a high-pass filtering or the Statistical Angle of Arrival and Doppler Method for GPS interferometry (SADM-GPS) developed by Afraimovich et al. (2003 and references therein). In this research, we used Polynomial fitting to the time series of TEC data which is an alternative to band pass filtering as a method for deriving TEC perturbations and we further take the cross-correlation between two latitudes or longitudes in time in order to observe the propagation of the MSTIDs. The detail explanations are described below:

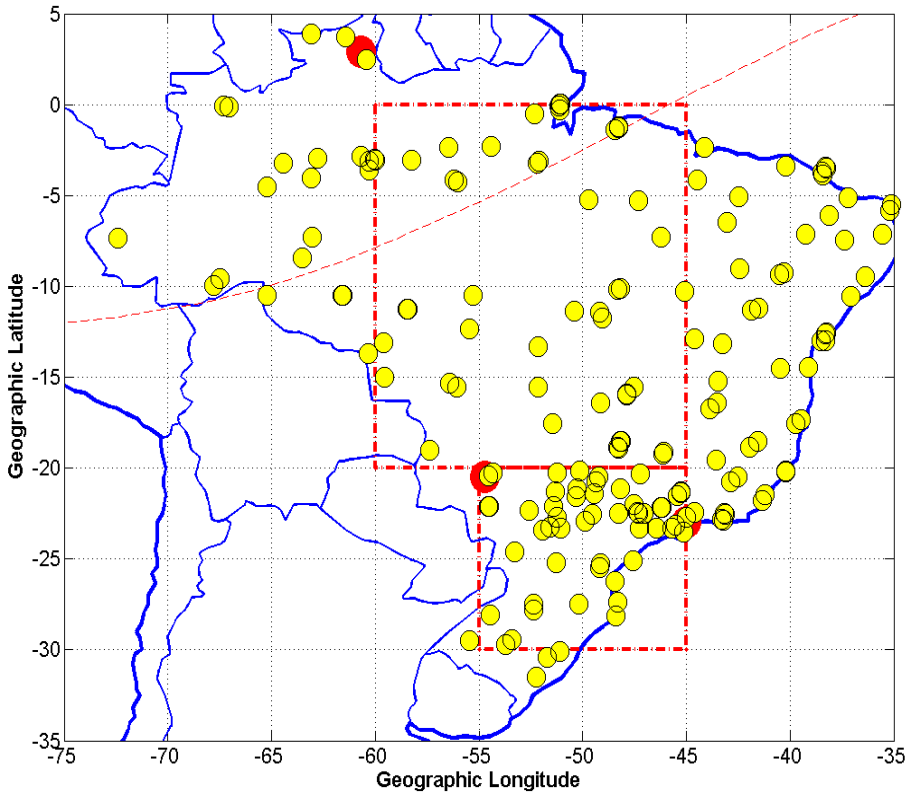

Figure 3.3 - The yellow circles in the red dash box show the distribution of the GPS receivers used, the red circles show the station of the digisonde locations and the red-dash line shows the magnetic equator.

Two-dimensional maps of absolute vertical *TEC* are derived with time resolution of 10 minutes and spatial resolution of 0.5° × 0.5° in latitude and longitude. The Nagoya model [Otsuka et al., 2002] is employed to derive the absolute TEC map over the cuts specified in Figure 3.3, which have relative high GNSS receiver spatial resolution of order of 200 km. The Nagoya-TECMAP program allows the calculation of *TEC* maps with up to 0.15° × 0.15° grid and is very useful for dense Global Positioning System (GPS) receivers network (e.g. the Japan GPS network distribution). Over the South America, with a relatively less dense GPS network, this program is running with a good performance by using data from the expanded Brazilian Network for Continuous GPS Monitoring (RBMC) Brazil network, and IGS stations placed at this region. We considered

data above 35° of elevation angle in order to minimize multipath effect. More explanation about the NAGOYA model can be found in Otsuka et. al. (2002).

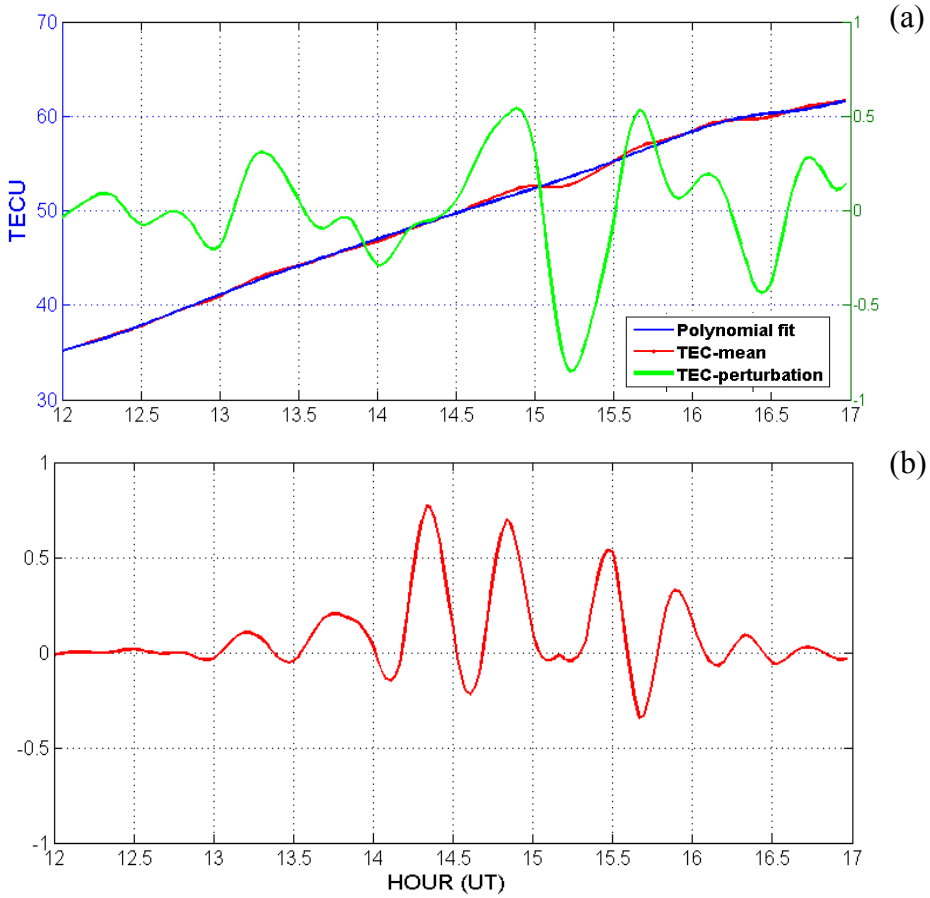

Figure 3.4(a) - represents TEC mean (red), its polynomial fit (blue) and the resultant detrended TEC (green), while the red curve in 3.4(b) shows an example of the cross-correlation between two latitudes which represents the MSTID propagation.

We focus on the *TEC* measurements during 12-17 UT thus boundary condition effects are avoided. From this *TEC* map, keograms are generated by choosing a cut along latitude and a cut along longitude directions. These keograms consist of the temporal variation of TEC distributed along the latitude and longitude. A polynomial fit with order 7 is employed to each of these spatially distributed time series and corresponding best fits are obtained. From this, the

TEC disturbance *(ΔTEC)* is derived by subtracting the TEC best fit *(TEC_{fit})* from the TEC mean i.e.:

$$\Delta TEC = \overline{TEC}_i - TEC_{fit}(x,t) \tag{3.4}$$

where $\overline{TEC_i} = \frac{\sum_{t=1}^{N} TEC_t}{N}$, *i* represents each latitude or longitude for all time and *N* is the total number of *t*. In Figure 3.4(a) the blue and red curves represent the polynomial fit and the mean *TEC* respectively, while the green curve is the detrended *TEC* obtained by equation (3.4). This method of deriving ΔTEC has been earlier employed by Galvan et al. (2011) to identify the tsunamigenic *TEC* disturbances and TIDs. From these keograms of *TEC*, cross-correlation maps are generated. The cross-correlation is defined as follows:

$$MSTID_{PROP} = \frac{\Delta TEC(x,t) \times \Delta TEC(x+\Delta x, t+\Delta t)}{(\Delta TEC)^2} \tag{3.5}$$

Where: *x* is the space (in longitude or latitude) and (*x, t)* is change is space with time, and $MSTID_{PROP}$ is the cross-correlation coefficient. These cross-correlation maps enable us to identify the waves, if present, by tracking the space and temporal shift of the maximum cross-correlation region. An example of this cross-correlation is shown in Figure 3.4(b) which represents the MSTIDs propagation between two latitudes as represented by equation (3.5).

3.2.2 Determination of convectional and non-convectional activity days

Observations of MSTIDs using the analysis described above are carried out during days with and without convection activities, since convection activities in the troposphere is one of the principal causes of AGW (VADAS et al., 2009) which can consequently lead to MSTIDs. Hence, analysis during some days with deep convection activities and some days with weak convection activity are investigated. The statistics analysis would be carried out during December

summer month of 2011 and 2014, which represent moderate solar activity. The prominently strong convection activities and the GNSS data availability contributes to our choice for the study of this time period.

According to Vadas et al. (2009) deep clouds near the tropopause region are indicative of regions of active convection and a likely source of gravity waves. Cold brightness temperature suggests deep convective plumes and convective overshoot which are a convenient launching platform for gravity waves (FRITTS et al., 2009). Gravity waves generated from the convective sources can propagate into the higher altitude and penetrate deep into the upper atmosphere (YIGIT et al., 2008; FRITTS et al., 2009). Therefore the convective activities will be defined from the water vapor and infrared temperature data which are obtainable from the CPTEC/INPE web site. A strong convection activity would imply that the difference in water vapor and infrared is greater than 0°C (i.e. WV – IR > 0°C) while a low convection activity implies that the difference between the water vapor and the infrared temperature is less than 0°C (i.e. WV – IR < °C) as given by Shume et al. (2014).

3.2.3 Statistical Method

The statistical analyses are computed using the following steps:

- To calculate the period of each wave event, a peak to peak wave in time was defined as one wave period.
- The velocity of the wave were computed by using the basic wave relations i.e. the velocity is the distance (λ) the wave travelled in space (latitude or longitude) divided by the time interval (i.e. $V=\lambda / T$), where λ is the wavelength and the T is the period of the MSTIDs.
- The wavelength is defined as the distance between peak to peak of the each wave event using visual assessment of the TEC perturbation map.

- The orientation and propagation direction of the each wave is determined by the ratio between the vertical and horizontal wavelength. While the vertical wavelength (λ_x) is related to the wave observed in the latitude and given by $2\pi/k_x$, the horizontal wavelength (λ_y) is related to the wave observed in the longitude and is given by $2\pi/k_y$. Hence the propagation direction is defined as tan= $\lambda_x/\lambda_y=k_y/k_x$, where k_x and k_y are the wave numbers in latitude and longitude respectively.

4.0 MSTIDS OBSERVATION RESULTS

This chapter presents and discusses the observed MSTIDs during the period of 4 days in December 2011. Event analyses are carried out to explain the characteristic properties of MSTIDs such as: the propagation directions, the velocity of the wave, the amplitude of the wave, the wavelength as well as the wavefront.

The morphology of the MSTIDs, such as frequency of occurrence, time and location has recently been observed by several authors. According to (HERNANDEZ-PAJARES et al., 2006; 2012) the MSTIDs are associated with the solar terminator and occur at daytime in local winter, and nighttime in local summer, and amplitude is correlated with the solar cycle. In Candido et al. (2008), the frequency of occurrence of MSTIDs, originating at high and mid-latitudes, was analyzed statistically revealing an inverse dependency between the MSTID occurrence rate and solar activity, with increased rate during the summer solstice. However, until date, the daytime MSTIDs using the detrended TEC has not been studied over the Brazilian sector. In this research, we show for the first the daytime MSTIDs using detrended TEC during summer solstice period over the Brazilian sectors and some new characteristics of daytime MSTIDs have been also discovered e.g. the geomagnetic conjugate observation of daytime MSTID.

MSTIDs introduce wavelike and periodic variations in the TEC which are the result of changes in the electron density anywhere along the line of sight. The TEC observations from a network of dual-frequency GPS receivers are used for the MSTID analysis. It is assumed that the changes in TEC (due to the MSTID) occur within a two dimensional thin ionosphere layer located at a fixed altitude of 350 km (approximately the altitude of the peak ionospheric electron density). Hence we used the pseudo-range and phase measurements of GPS signals at L1 (1575.42 MHz) and L2 (1227.60 MHz) frequencies to derive slant TEC

information, which was then converted to vertical TEC (VTEC) using the slant factor explained in Otsuka et al, (2002).

In section 4.1, we present the keogram plots of MSTIDs propagation results in latitudes and longitudes for 4 days in December 2011. Section 4.2 presents the statistical analyses of the events and show the preferred propagation direction of the daytime MSTIDs

4.1 Results of daytime MSTIDs at low latitudes

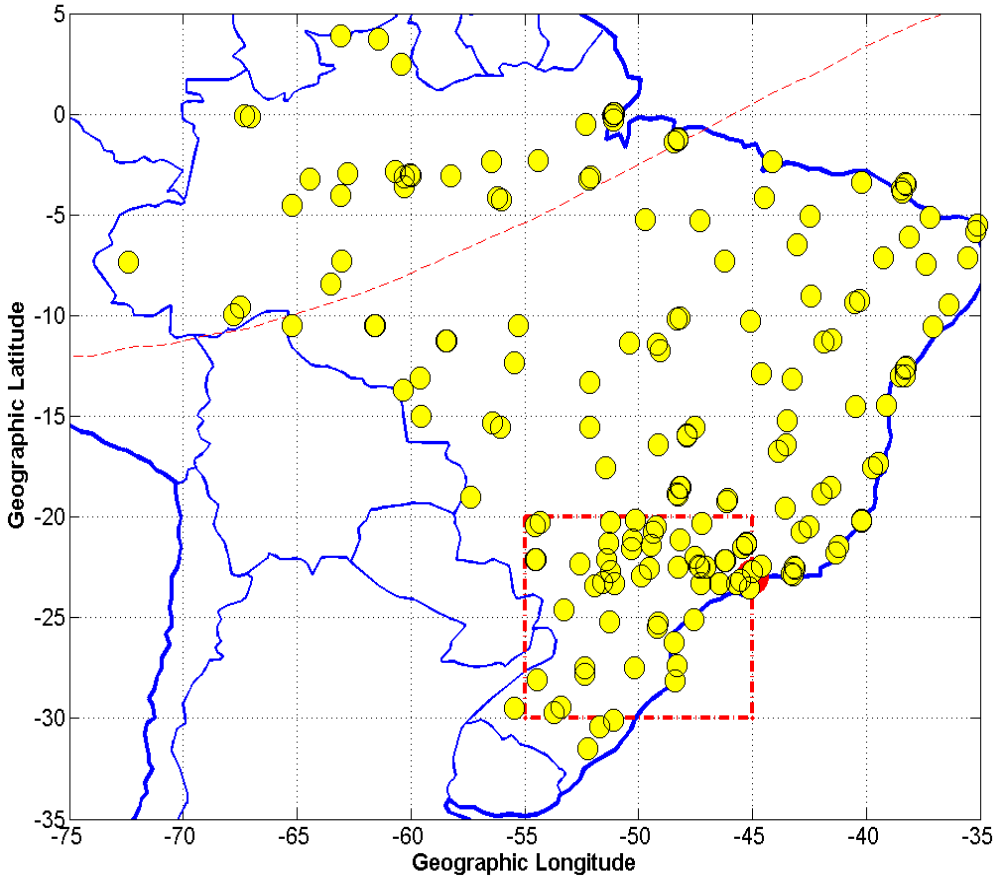

Figure 4.1 - The yellow circles in the red dash box show the distribution of the GPS receivers used, the red circle shows the station of the digisonde location and the red-dash line shows the magnetic equator.

To carry out our investigations we concentrate on the regions where there are more GPS receiver networks represented by the square box in Figure 4.1. This area shows where we have large amount of GPS receivers, up to 40 in a 10° x 10° square box in latitude and longitude (i.e. -30°S to -20°S and -55° W to –45°W). A large number of GPS receivers are located in the northern part of the square region which is over São Paulo state.

Figures 4.2a – 4.2d present the derived TEC disturbances from the GNSS measurements during quiet geomagnetic conditions (kp $\leq$ 3) on 5, December 2011 during 12-17 UT. Figures 4.2a and 4.2c are derived by equation (3.4) and they depict the temporal variation of the TEC disturbances extracted between latitude and longitude respectively. The y axis represents the detrended TEC (TECU) while the x axis represents the hour of the day in universal time. Each line plot represents the latitudinal oscillation for each 0.5°. It is important to note that a constant value is added to each detrended absolute TEC (ATEC) value in order to give a clear offset between the latitudes and longitudes plots represented in Figures 4.2a and 4.2c. On the other hand the corresponding cross-correlation maps in latitude and longihtude represented by Figures 4.2b and 4.2d respectively are derived using equation (3.5). Figures 4.3(a-d) to 4.5 (a-d) represent the same corresponding parameters but for days 6, 26, 27 December 2011. For easy comprehensive discussion, we refer 5, 6, 26 and 27 December 2011 as D5, D6, D26 and D27.

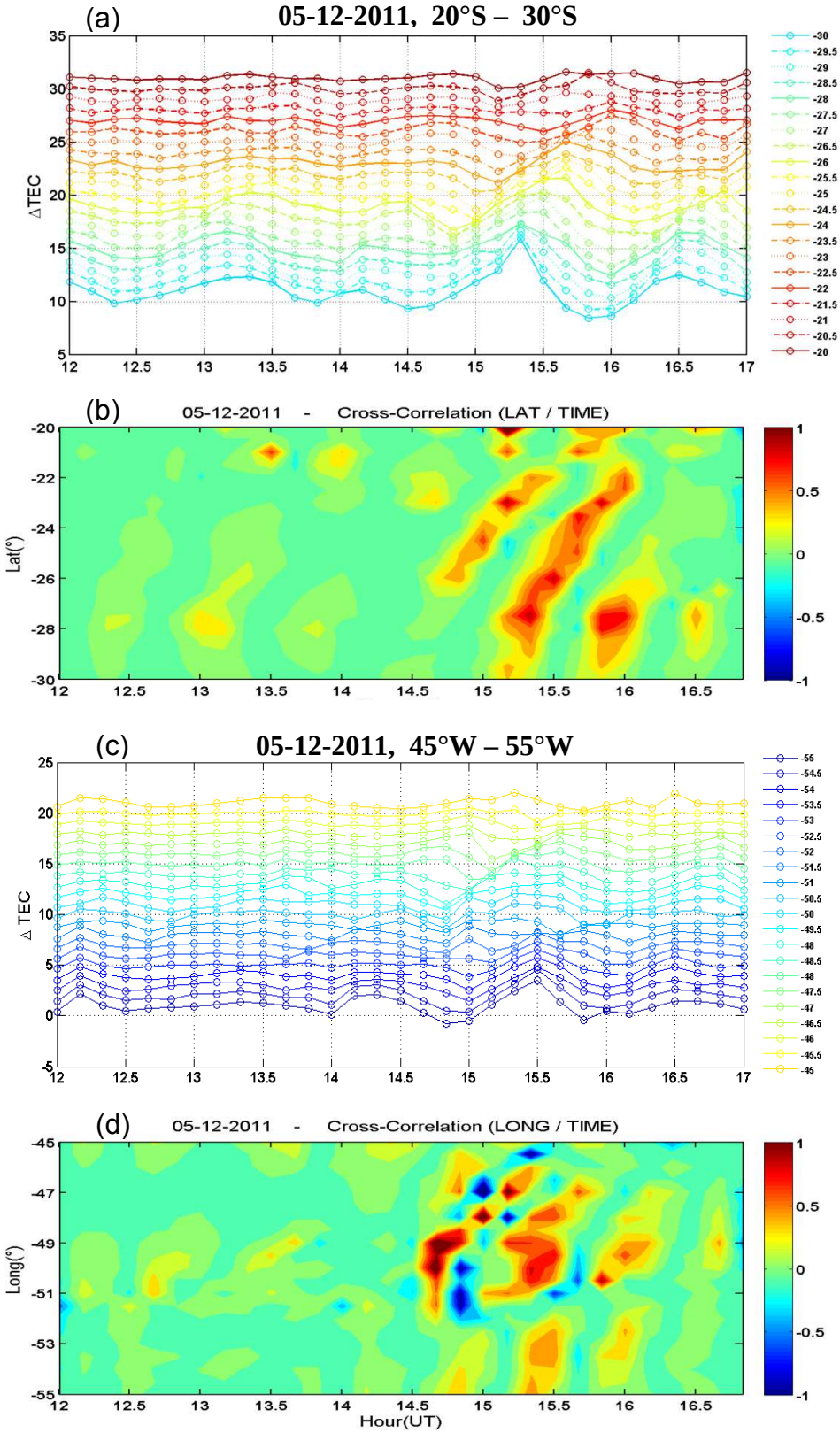

Figure 4.2 From top to bottom, the first and third panels represent the TEC disturbance, in latitude and longitude respectively. Each line represents latitude and longitude as indicated in the legend. The second and fourth panels represent MSTID propagation derived from the cross-correlation coefficients in Latitude and Longitude respectively

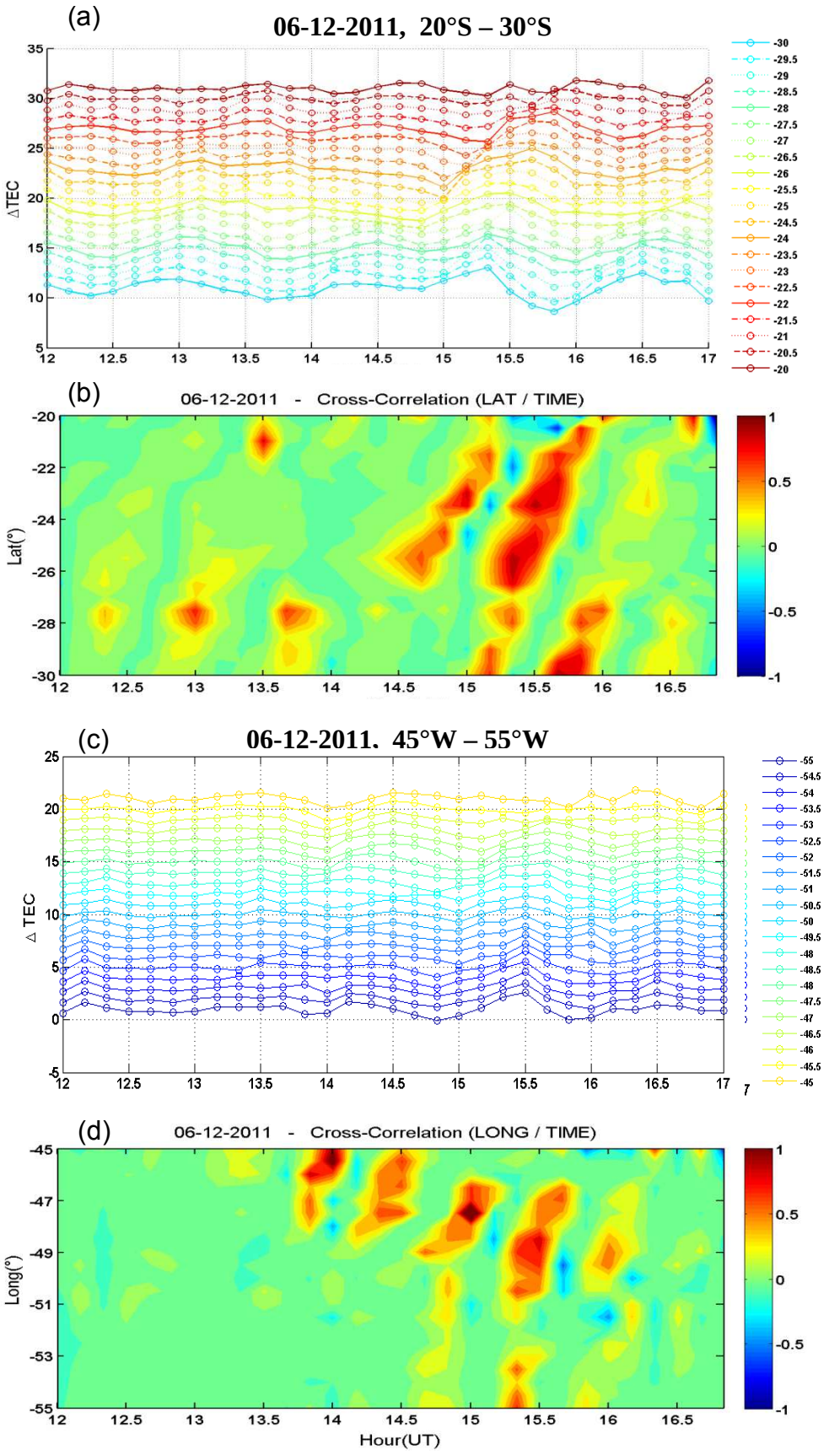

Figure 4.3 - The same as Figure 4.2 but for day 6 Dec. 2011.

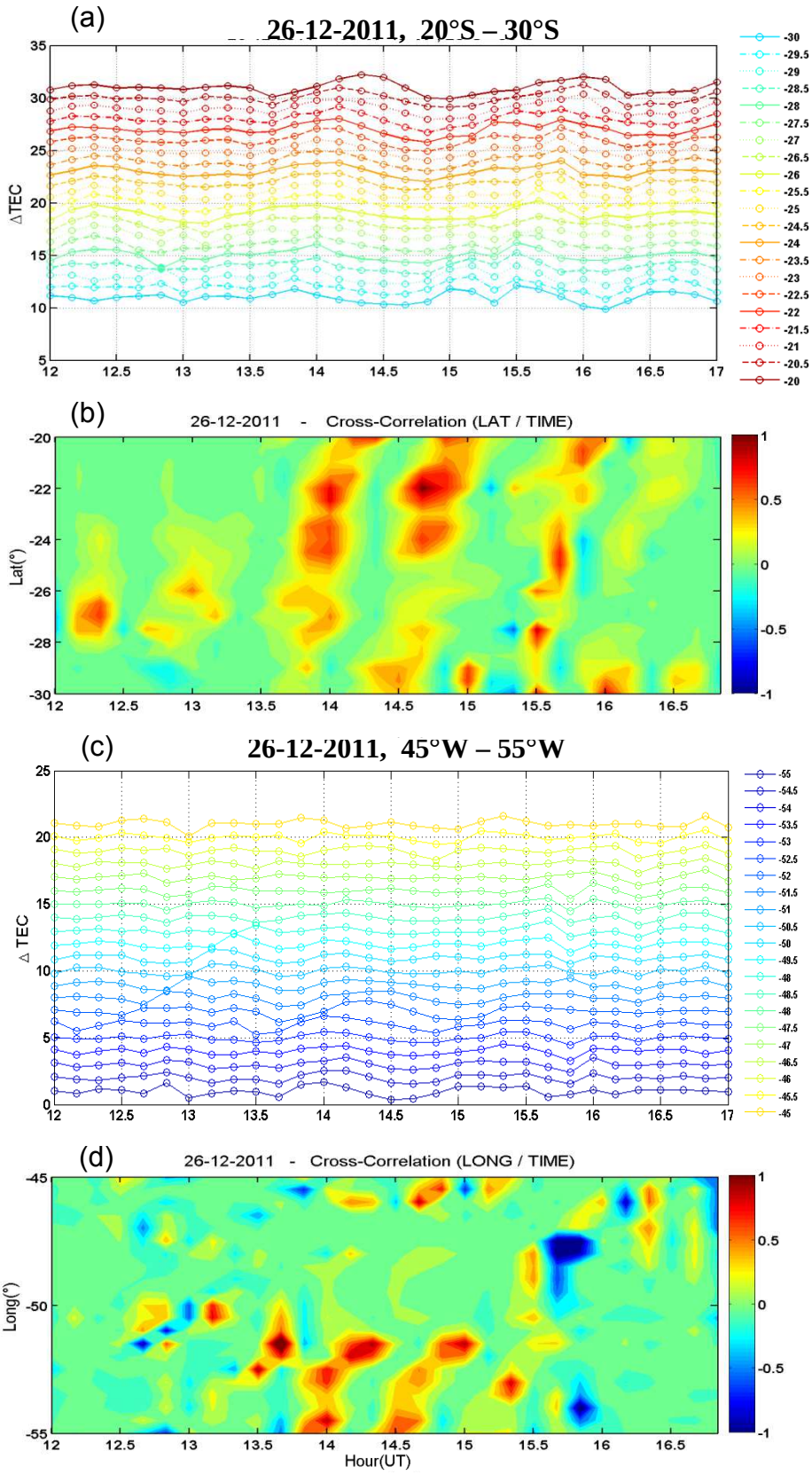

Figure 4.4 - The same as Figure 4.2 but for day 26 Dec. 2011.

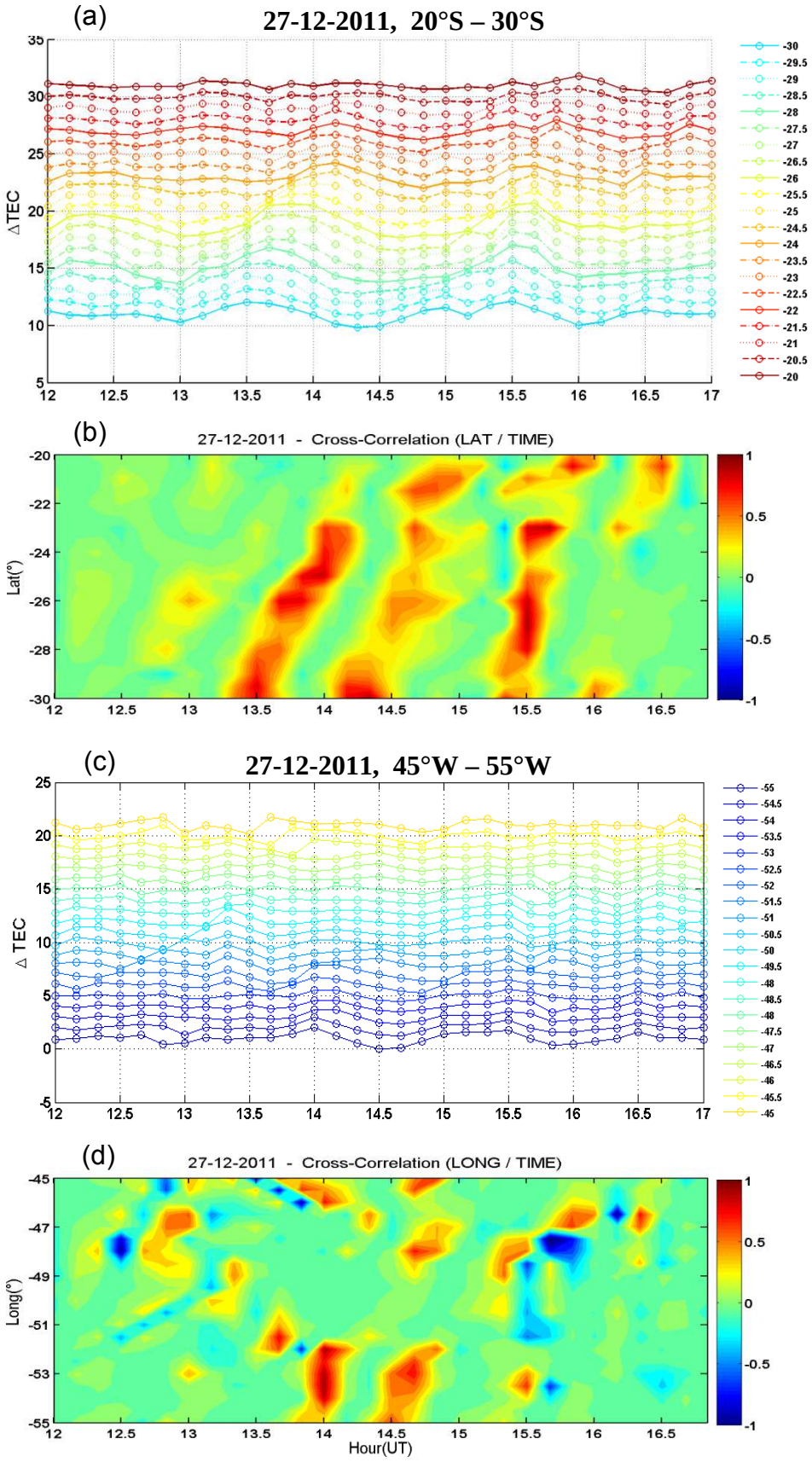

Figure 4.5 - The same as Figure 4.2 but for day 27 Dec. 2011.

We note the following features in Figures 4.2a – 4.2d on D5: (A) TEC disturbance oscillates in time at a chosen location with periods covering between 20-55 minutes, (B) the phase of the oscillation shifts in time while going towards equator and eastward, (C) corresponding cross-correlations maximize sometime during 13-16 UT, (D) the maxima are observed to commonly shift towards equatorward/eastward with time, (E) these cross-correlation maxima shifts longer and last longer in latitude than in longitude. Qualitatively, similar features are noted during D6, D26 and D27 at Figures 4.3, 4.4, and 4.5 respectively. Noteworthy quantitative differences are the following: (F) maximum amplitudes of TEC disturbances are largest on D5 and lowest on D26, (H) maximum cross-correlation occurs more towards eastward on D5-D6 while occurs more towards westward on D26 -D27 and their velocities are higher than the velocities for D5 and D6.

4.2 Statistical analysis Results

In the statistical analyzes the following techniques are used:

We represent an event as a single wave (i.e. each positive and negative peak in time) for each day. In each day, 10 – 14 events are identified depending on the MSTIDs activities for both latitude and longitude. The MSTIDs are defined as the TEC perturbations with amplitude greater than 0.2 TECU (1TECU=10^{16} electron/m^2) and period of perturbation less than 60min. The results are show in Figure 4.6 below.

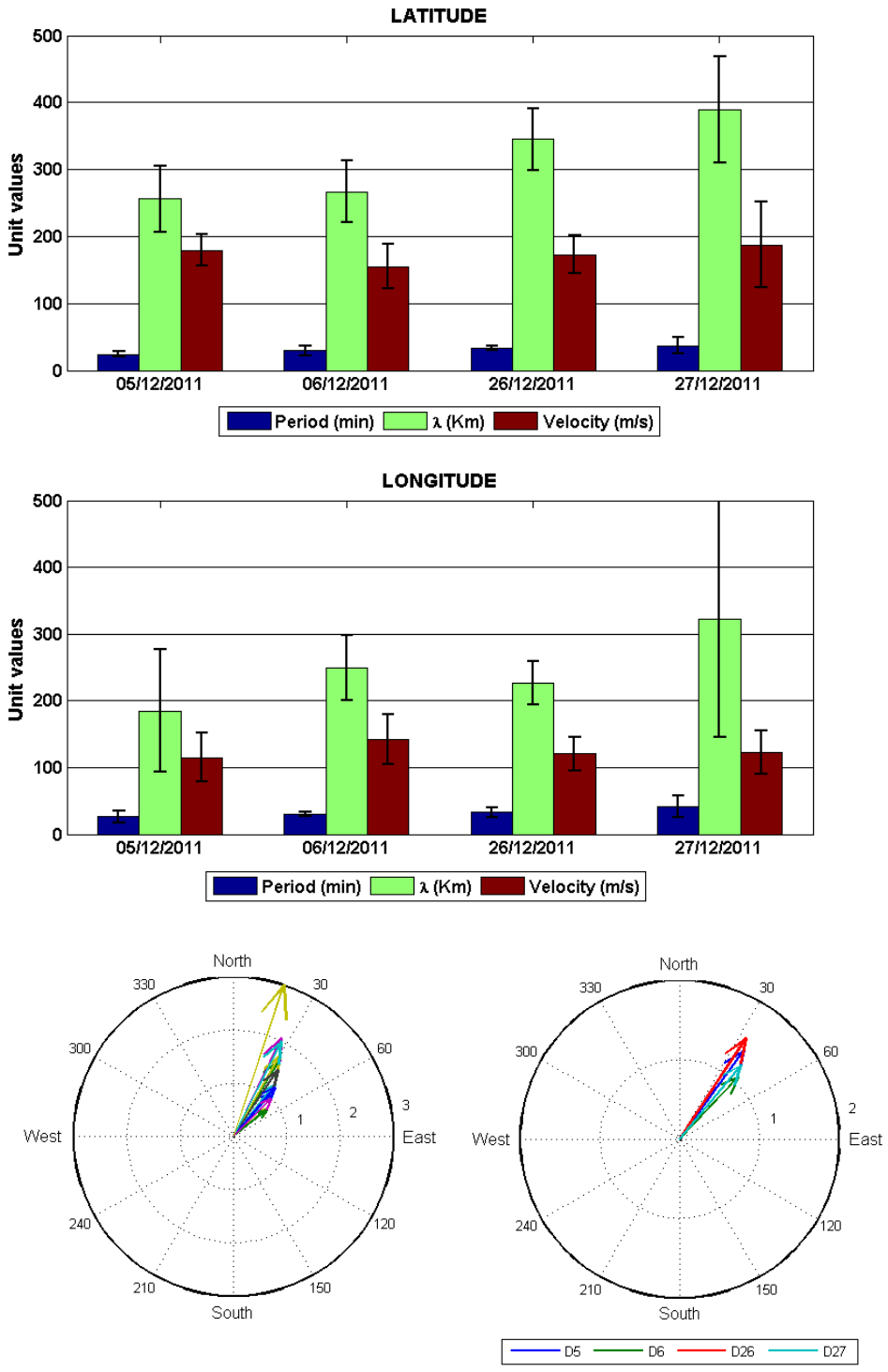

Figure 4.6 - The statistical evaluation of the MSTIDs period, wavelength, and velocity, represented in blue, green and red color respectively. The error bars represent the variance of daily MSTID wave characteristics. The polar plots at the bottom panels represent the directions of individual (left) and daily average (right) waves.

Figure 4.6 represents the statistical evaluation of the MSTIDs characteristics for D5, D6, D26 and D27 in term of period, wavelength, and velocity, represented in blue, green and red color respectively. The bars represent the standard deviation (STD) in the daily MSTID wave characteristics. The methodology used in the analyses is given in section 3.3.

It is possible to note the following important details in Figure 4.6: (G) The MSTIDs travel with a range of 155-189 m/s and with a wavelength range of 255-389 Km in the S-N direction, while in the W-E direction these values are 122-142 m/s and 184-322 km. (H) The wave generally travels with higher velocity and larger wavelength in S-N direction than in W-E direction (i.e. MSTID travels faster equatorward for the four events). (I) observing the variation of MSTID for each day from the error bar, it is possible to note that D27 represents the largest variation in their velocity, wavelength and period. (J) The amplitudes of the daytime MSTIDs attain maximum during noon time which is a known characteristics (KOTAKE et al., 2006; TSUGAWA et al., 2007; OTSUKA et al., 2013).The polar plots in Figure 4.5, show clear evidence of the equatorward (or Northward) directivity of the MSTID propagation for each wave event (left circle) and average for all events on each day (right circle). This shows consistency with the general properties of the MSTIDs observed.

The characteristics (A-B) and (C-D) suggest that the oscillatory TEC disturbances propagate equatorward/eastward in a form of wave which have periodicities ranging between 20-55 minutes and maximum amplitude during 13-16 UT. Periods and wavelengths of these TEC disturbances are in same range as those of the MSTIDs and therefore they can be classified as the MSTIDs. These properties are in close agreement with past literatures on MSTIDs (HERNÁNDEZ-PAJARES et al., 2006; 2012, TSUGAWA et. al., 2007, OTSUKA et al., 2004; 2013, KOTAKE et al., 2007, MACDOUGALL et al., 2011). Taking Hernández-Pajares et. al. [2006; 2012] for a reference, since part of their study deals with MSTID observations over southern hemisphere (at New

Zealand), it is possible to note that the wave properties such as the velocity of propagation and wavelength varying from 100 – 400 m/s and 50 – 300^{+}km, respectively, are in good agreement with the present study. In addition, the daytime wave propagation direction in both studies are mainly to equatorward and eastward directions. The major contrast between these studies is that the daytime MSTIDs in the present study are observed during summer and solar moderate condition of December 2011 while most observations at Hernández-Pajares et al., [2006, 2012] are during winter-fall daytime and spring-summer nighttime but there were no major reports of MSTIDs occurrence during summer daytime for a complete solar cycle. MacDougall et al., 2011 using NmF2 from south hemisphere shows daytime MSTIDs during summer and explain that daytime MSTIDs during summer should be expected since the AGW activity causing most daytime MSTIDs are approximately equal for both day and night.

The characteristic (E) suggests that these waves have S-N average wavelength longer than the W-E average wavelength. A close look into Figures 4.2 to 4.5 reveals that the S-N average wavelengths range between 255 and 389 km and is much longer than the W-E average wavelengths which range between 184 and 322 km. Hence the average propagation velocities are estimated at 187 and 122 m/s in the S-N and W-E directions respectively. This observation shows that MSTIDs move faster towards equator than towards east. Therefore this observation is a property of daytime MSTIDs which could be caused by the preferred movement of charge/neutral particles along geomagnetic field line compared to their orthogonal movement. This particular aspect suggests that the wavefronts of these daytime MSTIDs are inclined more towards S-N than W-E. In this appearance, they resemble the nighttime MSTIDs observed over Northern hemisphere (TSUGAWA et al., 2007; OTSUKA et al., 2013) though they propagate eastward while the night-time MSTIDs propagate westward.

Another important outcome of the present study is that the southern MSTIDs are also preferentially propagating equatorward/eastward as shown by the polar plot at Figure 4.6 which is in agreement with the Hernández-Pajares et al., (2006, 2012).

The equatorward propagation of MSTIDs as noted in this study and in earlier studies can be explained based on gravity wave forcing mechanism proposed by Hooke (1968) and Kotake et al., (2007): the equatorward propagating gravity waves cause larger neutral particle oscillations parallel to $\vec{B}$, in comparison to gravity waves propagating in other directions. This scenario leads to the larger plasma motion along geomagnetic field lines making the equatorward direction as a preferred direction of propagation for the MSTIDs. In the southern hemisphere over Brazil, owing to the large declination angle, aforementioned scenario may be slightly altered but still would maintain the same directivity which is consistent with the present study.

5.0 GEOMAGNETIC CONJUGATE OBSERVATIONS OF DAYTIME MSTIDS AS DETECTED BY TEC DISTURBANCE.

In this chapter, we present some observations and simulations of past literatures on geomagnetic conjugate MSTIDs to set a quick background. We then focus on our results of daytime MSTIDs observed in conjugate hemispheres and discussed the mechanisms responsible for conjugate mapping of the observed daytime MSTIDs.

One of the interesting characteristics of MSTIDs is the ability of mapping along field lines from one hemisphere to the conjugate hemisphere. Burnside et al. (1983) have shown that large electric field could originate at one hemisphere and map along the magnetic field lines to the opposite hemisphere using the ISR measurements during nighttime periods. Since then many literature have shown that electric field mapping to the opposite hemisphere can generate conjugate MSTIDs that mirror around the equator to the opposite hemisphere during nighttime period (YOKOYAMA AND HYSELL, 2010, MARTINIS et al., 2010). Some recent literatures have shown geomagnetic conjugate observation and explained the responsible mechanisms, (e.g. OTSUKA et al. (2004)). Otsuka et al. (2004) reported a simultaneous observation of MSTIDs at geomagnetic conjugate points using a 630 nm all-sky CCD imager at Sata (northern hemisphere) and at Darwin (southern hemisphere). They show that MSTIDs at Darwin propagated northwestward at almost same velocity as the MSTIDs observed at Sata. The amplitudes of the airglow intensity perturbations were approximately 20% and 40% of the background at Sata and Darwin, respectively which could imply that the MSTIDs were generated at Darwin and mapped to Sata.

In order to investigate polarization electric field involvement of the nighttime MSTID structures between the northern and southern hemispheres, Otsuka et al. (2004) mapped Darwin images from southern hemisphere into the northern hemisphere along the geomagnetic field lines using the International Geomagnetic Reference Field 2000 model (IGRF2000). The eastern part of the

airglow images from both Darwin and Sata were superimposed, thereby allowing the two band-like structure of high and low airglow intensities on one side to be smoothly connected to those on the other side of the image. As a consequence, it was evident that the band-like structure over northern hemisphere (Sata) corresponded well with those mapped along magnetic field lines from the southern hemisphere (Darwin).

The similarities in structural features between the two hemispheres could be seen in all MSTID images at 1448 to 1520 UT (Figure 5.1). This result clearly indicates that the 630-nm airglow structures associated with MSTIDs were mapped along $\vec{B}$ and mirrored between the northern and southern hemispheres by polarization electric field development during this period. Valladares et al. (2016) recently investigated the spatial variability and dynamics of nighttime MSTIDs and mapping characteristics of MSTIDs from one hemisphere to the conjugate hemisphere on 2 days in August, 2012. The most viable explanation from instrument like airglow images by Fukushima et al. (2012), observation from satellite measurements by Jonah et al. (2016 and references therein) for the generation of daytime MSTIDs has been gravity waves excitement of electric field. The study of Kelly and Fukao (1991) also suggests that gravity waves could produce required density structures during nighttime, which are explained by the Perkins instability. Another important characteristics of MSTIDs, as observed in TEC amplitude, is the propagation preferential toward equator which have been explained by authors like Kotake et al. (2007) and Jonah et al. (2016) as due to the neutral particles oscillation parallel to $\vec{B}$ being larger for gravity wave travelling equatorward than those travelling in other directions.

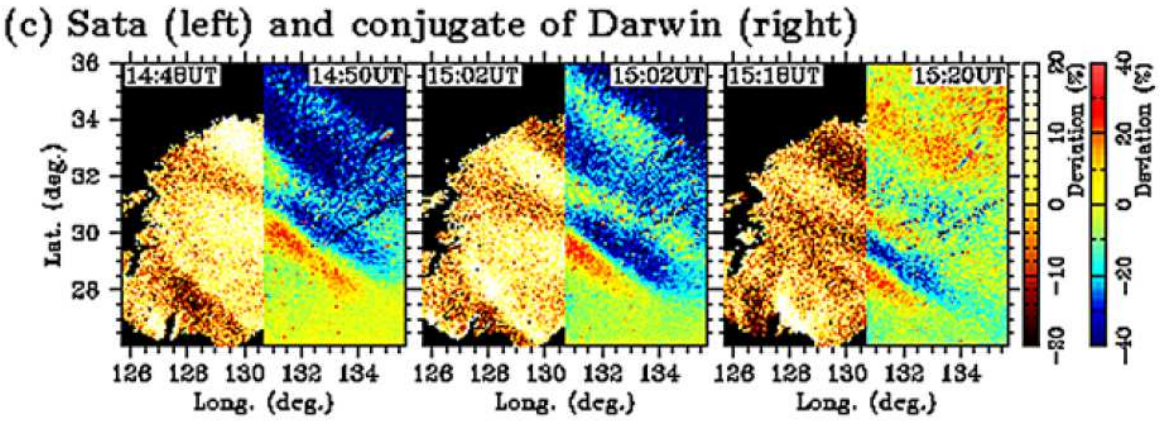

Figure 5.1 - Images composed of Sata and Darwin images. The southern hemisphere is mapped onto the northern hemisphere along the geomagnetic field lines and superimposed onto the right-hand side of each corresponding image. The wave-like airglow structures caused by MSTIDs are smoothly connected between the two images.
Source: Adapted from Otsuka et al. (2004).

Huba et al. (2015) presented a 3-D simulation study of conjugate ionospheric effects associated with the Tohoku-Oki tsunami of 11 March 2001during nighttime period. Using the SAMI3/ESF, they run a simulation of tsunami-driven gravity wave. It was noted that even though the tsunami driven gravity wave disturbance is in the northern hemisphere, its effects could be observed at the conjugate southern hemisphere because the electric field mapped to the conjugate region on the Alfvenic time scales. Figure 5.2 shows in the left column the vertical neutral wind induced by tsunami driven GW (w'), in the middle column the differential TEC, and in the right column the fractional change in the 6300 Å emission as a function of latitude. It is possible to clearly observe perturbations in the TEC and 6300 Å emission at time 12:44 UT in the Northern Hemisphere associated with the gravity wave and at this time there are also perturbations in TEC and optical emissions in the Southern (conjugate) Hemisphere. At time 14:44 UT the gravity wave is at the magnetic equator. The variation in the TEC is very small, but there are still significant variations in the 6300 Å emission. Finally, at time 16:44 UT the gravity wave has reached the southern conjugate region, and strong perturbations are observed in the TEC and 6300 Å emission. There are also perturbations in the northern conjugate region at this time. They finally concluded that the perpendicular neutral wind

perturbations generate an electric field that maps to the magnetically conjugate regions in the ionosphere and causes observable ionospheric disturbances in the TEC and airglow emission.

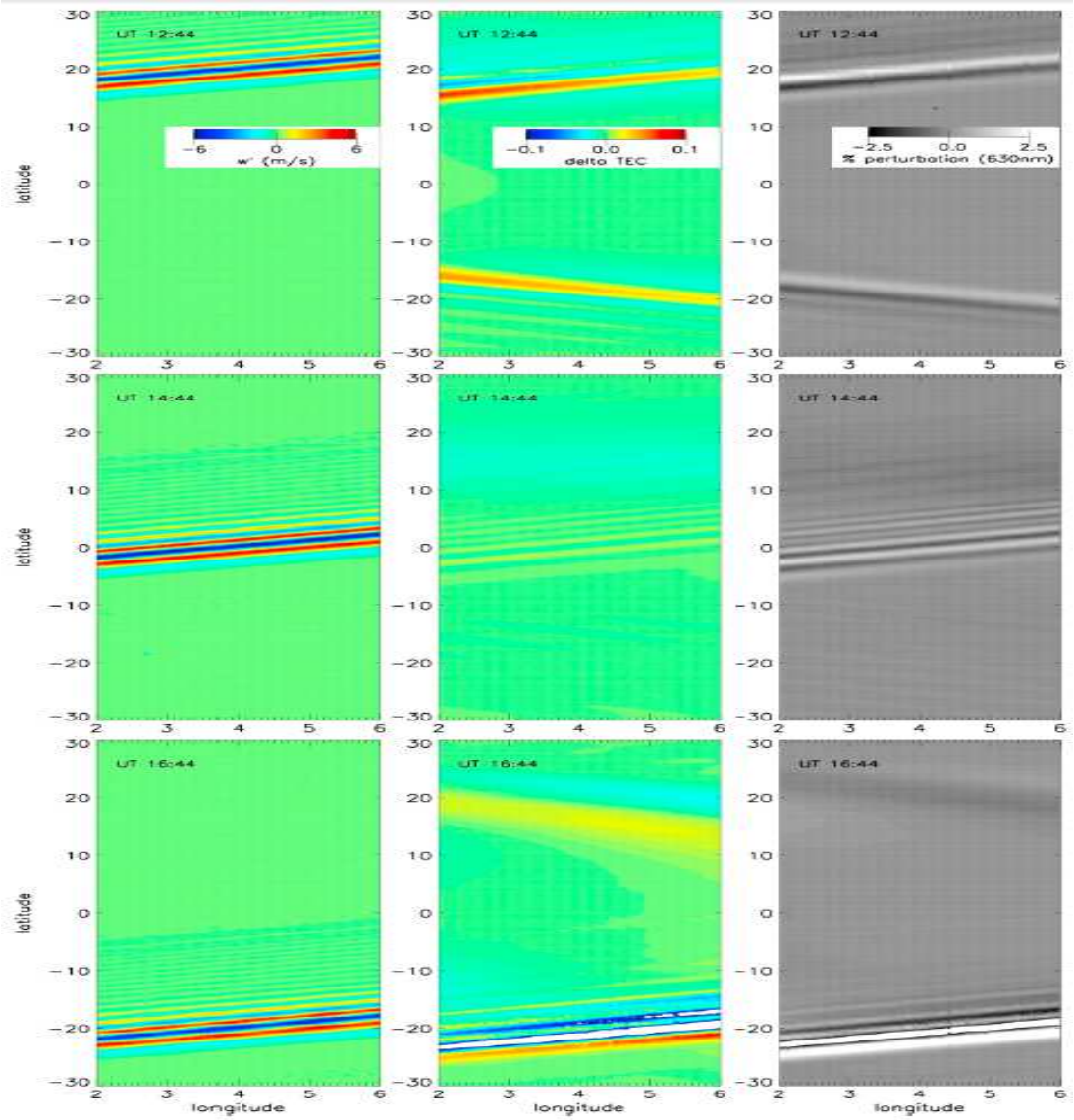

Figure 5.2 - Contour plots of the (left column) gravity wave-induced neutral vertical velocity at 272 km, (middle column) the differential TEC, and (right column) the fractional 6300 Å airglow emission as a function of latitude and longitude at times (top row) 12:44 UT, (middle row) 14:44 UT, and (bottom row) 16:44 UT.
Source: Adapted from Huba et al. (2015).

5.1 Results on the observed geomagnetic conjugate daytime MSTIDs

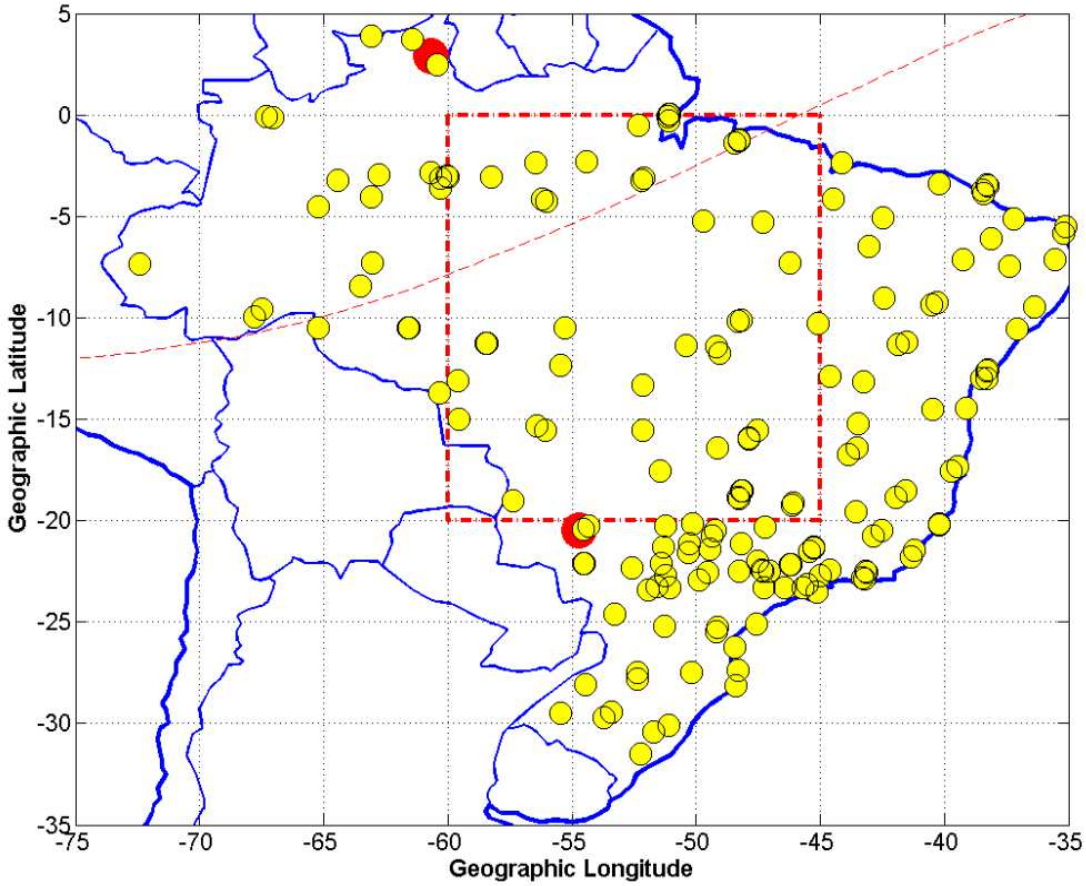

Figure 5.3 - The yellow circles in the red dash box show the distribution of the GPS receivers used, the red circles show the stations of the digisonde locations and the red-dash line shows the magnetic equator.

It is the first time that the geomagnetic conjugate daytime MSTIDs will be observed over the South America sector. To observed this characteristic, we used detrended TEC at Brazilian sector that cut along the northern and southern hemisphere geographically (i.e. -30°S to -20°S and -55° W to – 45°W) at Figure 5.3. The coordinate is later converted to geomagnetic coordinate by using the IGRF model.

Figures 5.4a – 5.4d present the derived TEC disturbances from the GNSS measurements during quiet geomagnetic conditions (Kp $\leq$ 3) on 17, December 2014 during 12-17 UT. The y axis represents the detrended TEC (TECU) and the x axis represents the hour of the day in universal time. Figures 5.4a and 5.4c are derived by equation (3.4) and they depict the temporal variation (UT) of the TEC disturbances (ΔTEC) extracted in latitude and longitude respectively. Each line plot represents the latitudinal oscillation for each 0.5°. It is important to note that a constant value is added to each detrended Vertical TEC (VTEC) value at Figure 5.4a and 5.4c in order to give a clear offset between the lines latitudes and longitudes plot. On the other hand the corresponding cross-correlation map, quantified by the color bar, in latitude and longitude and represented by Figures 5.4b and 5.4d respectively, are derived using equation (3.5). Figures 5.5 (a-d) to 5.7 (a-d) represent the same corresponding parameters but for days 18, 27, 28 December 2014. For easy comprehensive discussion, we refer 17, 18, 27 and 28 December 2014 as D17, D18, D27 and D28.

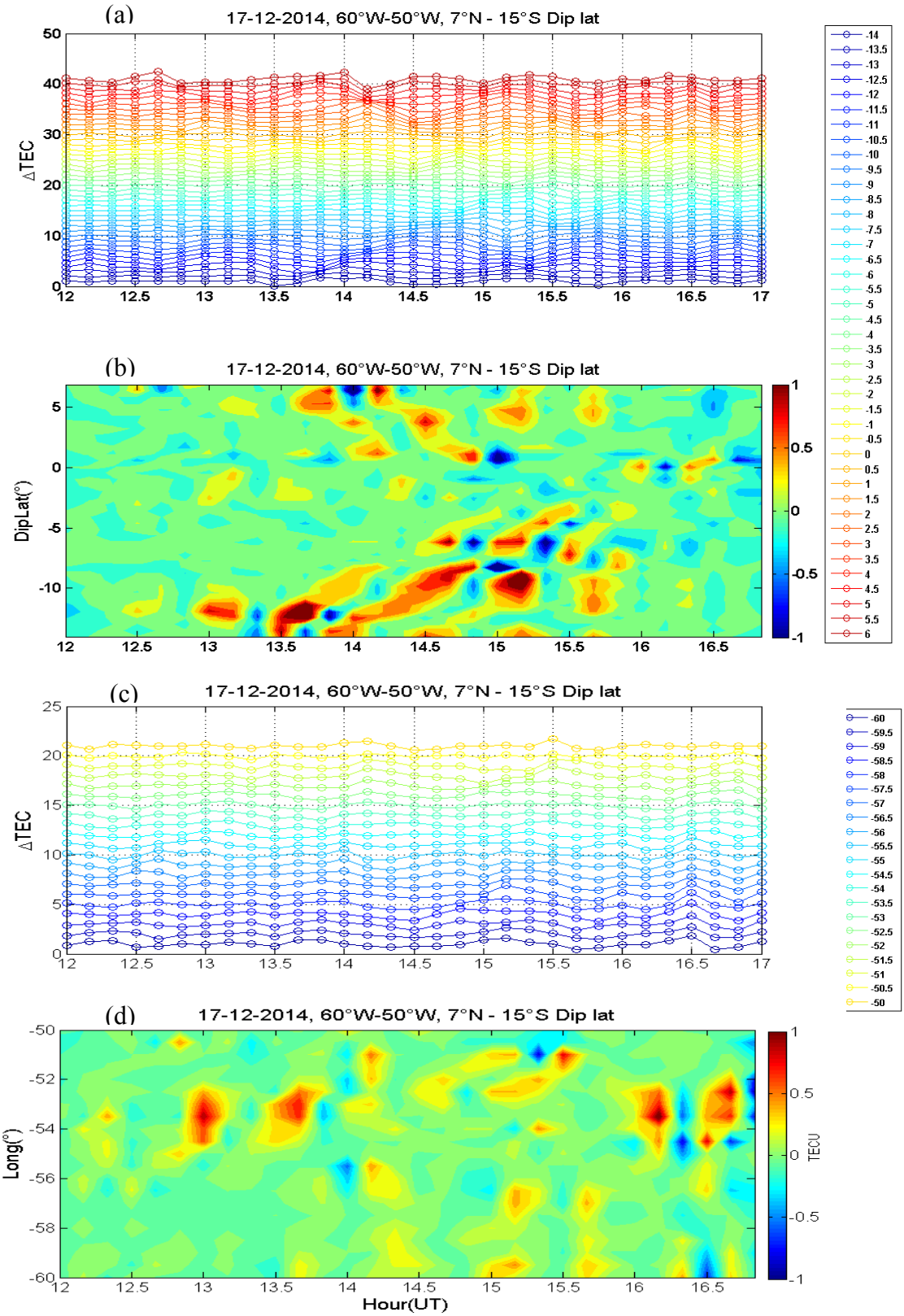

Figure 5.4 From top to bottom, the first and third panels represents the TEC disturbance, in latitude and longitude respectively. Each line represents latitude and longitude as indicated in the legend. The second and fourth panels represent MSTID propagation derived from the cross-correlation coefficients in latitude and longitude respectively.

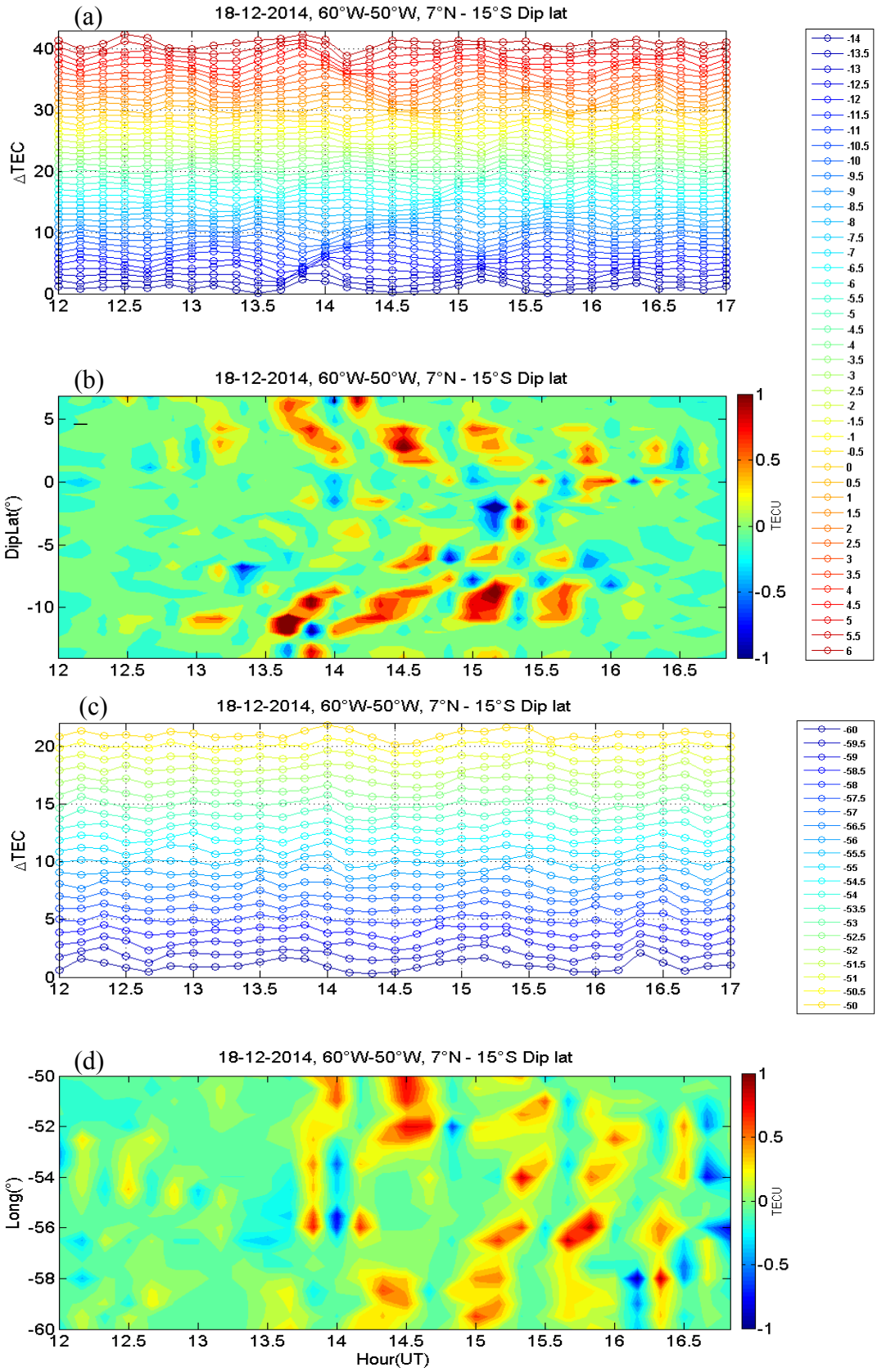

Figure 5.5 - The same as Figure 5.4 but for day 18, Dec. 2014.

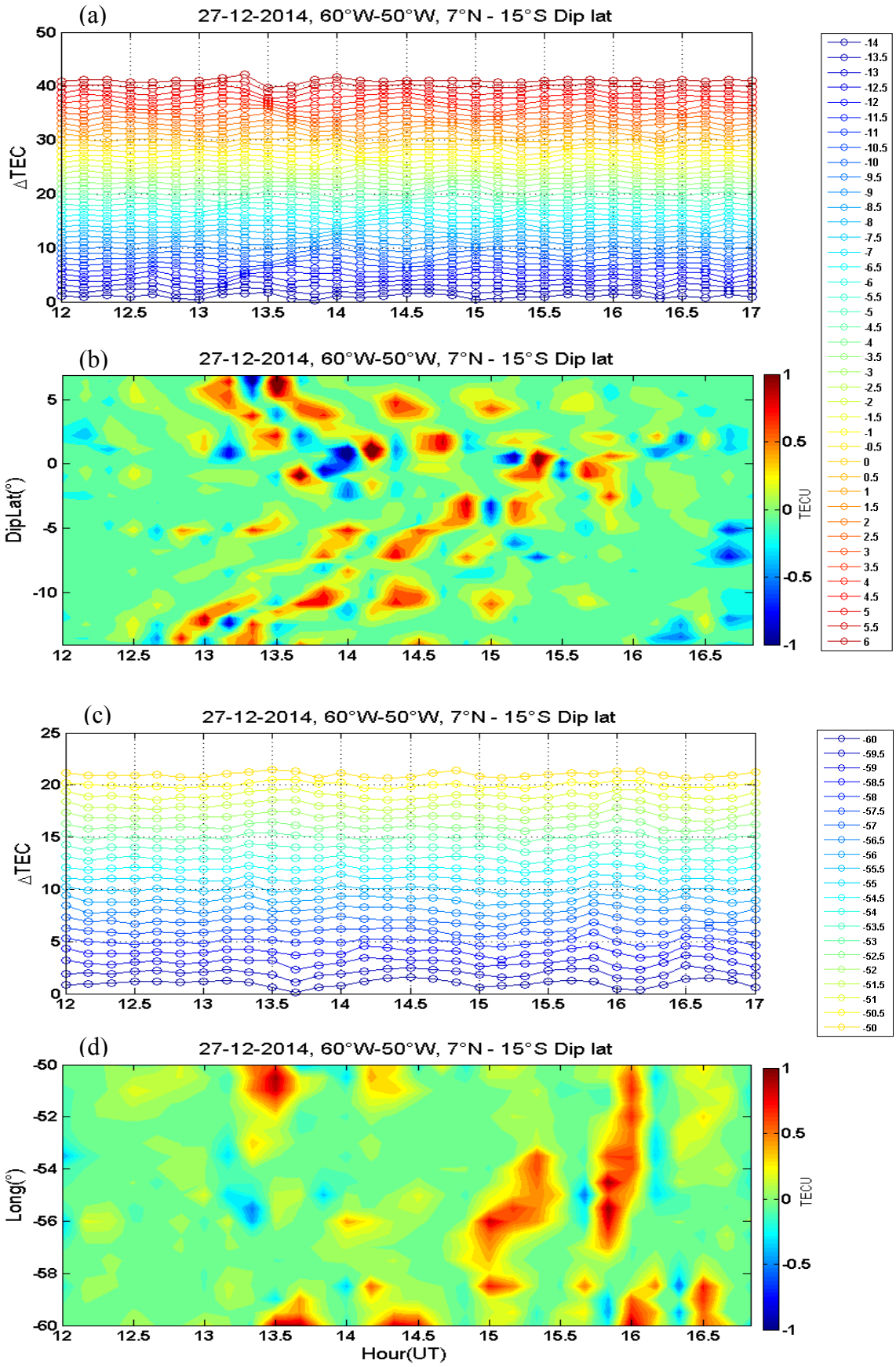

Figure 5.6 - The same as Figure 5.4 but for day 27, Dec. 2014.

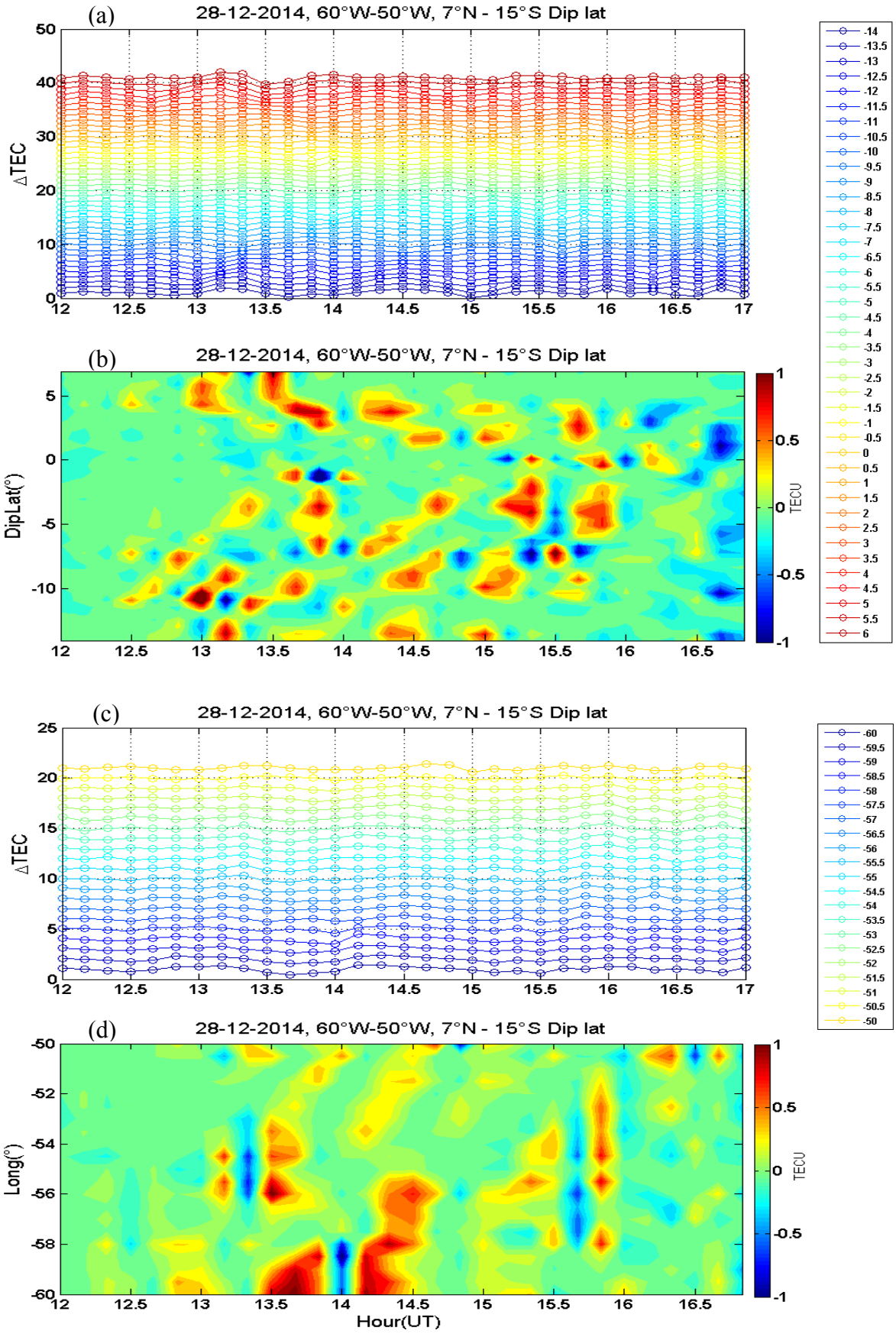

Figure 5.7 - The same as Figure 5.4 but for day 28, Dec. 2014.

We note the following features in Figures 5.4a – 5.4d on D17: (A) ΔTEC disturbance oscillates in time at a chosen location with periods covering between 15-55 minutes, (B) the phase of the oscillation shifts in time while going towards equator and eastward, (C) corresponding cross-correlations maximize sometime during 13-16 UT, (D) the maxima are observed to commonly shift towards equatorward/eastward with time in both hemispheres, (E) these MSTIDs are well defined and last longer in latitude than in longitude. (F) MSTIDs generated at the southern hemisphere map to the conjugate hemisphere. (G) the mirrored/mapped MSTIDs occurs around 0° geomagnetic equator as expected. (H) It is clear that the MSTIDs are generated at the southern hemispheres because cross-correlation amplitude is stronger at source hemisphere. Qualitatively, similar features are noted during D18, D26 and D27 at Figures 5.5, 5.6, and 5.7 respectively. Noteworthy quantitative differences are the following: (I) there are more events and mappings of MSTIDs on D28 (maximizing from 12:30UT unlike others which maximize from 13UT) and lesser events and mappings are observed on D17, (J) maximum cross-correlation occurs more towards eastward on D18-D27 while occurs more towards westward on D17 -D28.

5.1.1 Mechanism responsible for the daytime MSTIDs mapping:

It may be noted that the major features at A to E are similar to those discussed at section 4.1. The new important characteristics for this result are mentioned at (F-H) and discussed below (JONAH et al, submitted to JGR):

The mapping of nighttime MSTIDs to the conjugate hemisphere and the mechanisms responsible has been explained by both observation (Otsuka et al, 2004) and simulation (HUBA et al, 2015) (see section 5.0). However, these explanations only hold for nighttime MSTIDs and cannot be applicable to the daytime behavior because the electrodynamics of sunset and nighttime ionosphere are quite different from that of sunrise and daytime ionosphere. There are no literatures yet that explain the mechanism of a simultaneous

observation of MSTIDs mapping from one hemisphere to the other hemisphere during daytime. The conjugate nighttime MSTIDs mapping were explained by the polarization electric field observed at either hemisphere and mapped along magnetic field to the conjugate hemisphere through $\vec{E} \times \vec{B}$ drift.

The polarization electric field is possible during nighttime, because electric field generally generated by the F region dynamo mechanism is no longer short circuited by the E region due to the famous sunset terminator mechanism. Moreso, as explained by Otsuka et al. (2004), current $\vec{J}$ would flows to the almost same direction as $\vec{U} \times \vec{B}$. Since $\vec{J}$ traverses the perturbations of integrated Pederson conductivity (wavefront of MSTIDs over one hemisphere), polarization electric fields ($\vec{E}_P$) should be generated to maintain a divergence-free of ionospheric currents. For this reason, $\vec{E}_P$ should be perpendicular to the wavefronts of MSTIDs.

On the other hand, for daytime MSTIDs mapping structures, the mechanism responsible could be similar to the generating mechanism during nighttime if the E region is not short circuited (i.e. if the F region controls). The conventional perception is that there is always short circuit effect in the E region during daytime which would not allow the mapping of polarization electric field but this is not always the case as recently shown by Abdu et al. (2015).

Abdu et al. (2015) observed polarization electric field in the F region during the time interval of 13 to 21 LT, and investigated the phenomenon by using the model (SUPIM) simulation results to calculate the field line-integrated conductivity ratio. The polarization electric field is given by the following equation:

$$\vec{E}_y = -\Delta \vec{U}_z \times \vec{B}_o \left[\sum\nolimits_F \Big/ \left(\sum\nolimits_F + \sum\nolimits_E \right) \right] \qquad (5.1)$$

where E_y is the zonal polarization electric field, ΔU_z is the vertical perturbation wind, B_o is the magnetic field intensity, $\sum_F and \sum_E$ are the field line-integrated Pederson conductivities of F and E regions respectively.

In their methodology they show that equation (5.2) can be used as a rough approximation of the LT variation of the integrated conductivity ratio,

$$\left[\sum_F \Big/ \left(\sum_F + \sum_E\right)\right] \approx \left[\frac{Ne8MHz}{\left(Ne8MHz + NmE\right)}\right] \qquad (5.2)$$

where Ne8MHz is the electron density at the F region plasma frequency of 8 MHz and NmE is the E layer peak density. These parameters are obtained from digisonde.

Additionally, their results on both observation and simulation show that the zonal polarization electric field produced by the gravity wave wind perturbation in the F region is sustained when the conductivity ratio (in bracket on equation 5.1) is around 0.8 (80%).

Based on the above methodology, we used the parameters Ne8MHz and NmE from the digisondes at magnetically conjugate sites of Boa Vista (2.62°N, 60.7°W, dip lat: 4.74° N) and Campo Grande (20.55°S, 54.7°W, dip lat: 12.38° S) to further investigate our results on daytime MSTIDs mapping to conjugate hemisphere. The stations are shown in red circle at Figure 5.3.

In Figure 5.8 the following parameters are plotted: Ne8MHz, the electron density at the F region plasma frequency of 8 MHz, the values of its heights (hF8MHz) and those of the E layer peak density (NmE) for days 27 and 28 (the available days) over both Boa Vista and Campo Grande, as well as the ratio Ne8MHz/ (Ne8MHz + NmE) (in the bottom plots for each day). Note that there are no complete digisonde data for the rest of the MSTID event days.

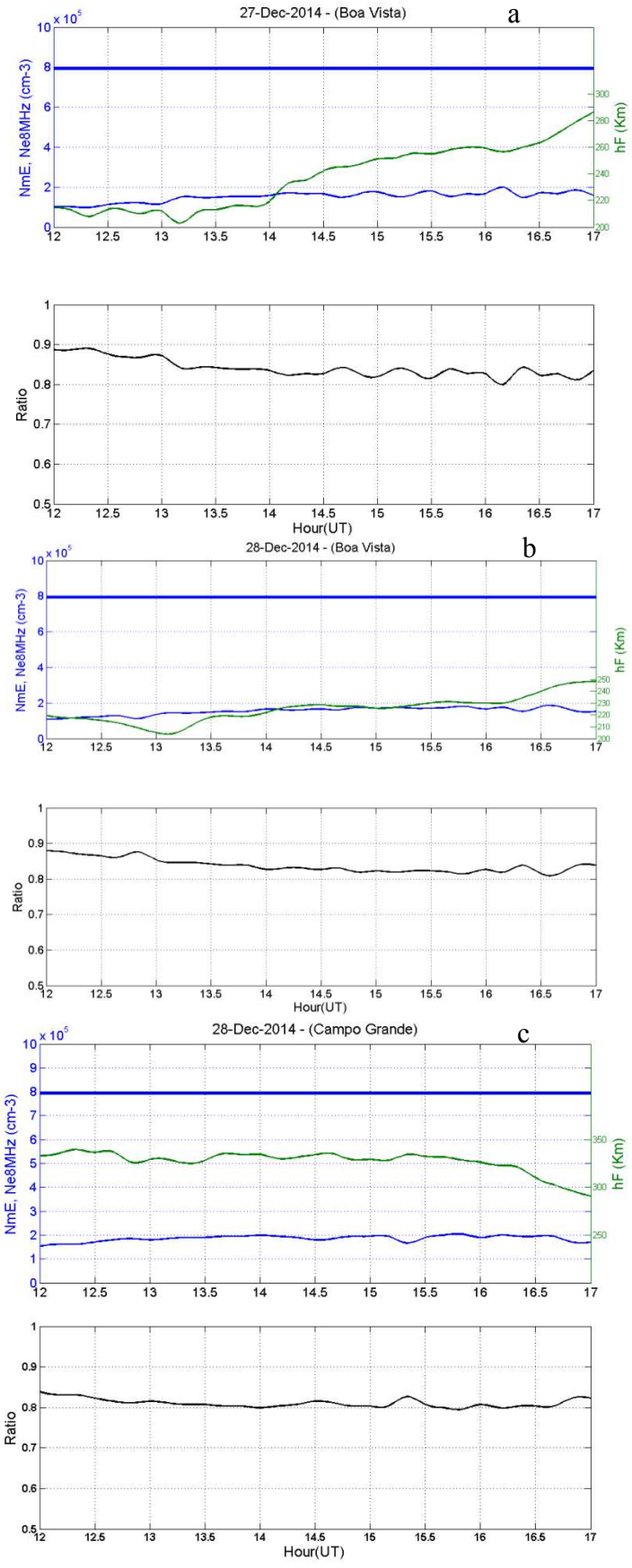

Figure 5.8 - Electron density (thick blue) at the F region plasma frequency of 8 MHz (Ne8 MHz), the heights at 8 MHz plasma frequency (green curve) and the E layer peak density (NmE) (thin blue curve), as well

as the ratio of Ne8MHz/ (Ne8MHz + NmE) (black curve at the bottom plots for each day).

It is possible to observe from the bottom panels of Figure 5.8a, b, and c that the curve representing the conductivity ratios are between 0.88 to 0.80, which means approximately 80% of the zonal polarization electric field is produced by the wind perturbation in the F region during the observed conjugate daytime MSTIDs mapping events. To support this hypothesis, we show at Figure 5.8d similar results of Figure 5.8(a-c) but for day 30 Dec. 2014 (a day without MSTIDs mapping). Figure 5.8d shows that the rough approximation for the conductivity ratio on this day dropped from less than 0.8 (around 13UT) to 0.5 (around 17UT). This daytime characteristic implies that, similar to nighttime mapping, the daytime polarization electric field due to gravity waves in the daytime F region could be responsible for daytime MSTIDs conjugate mapping. Furthermore, investigations show that AGW is the main generation source of this zonal polarization electric field during daytime as illustrated and discussed in the following sections (JONAH et al, submitted to JGR).

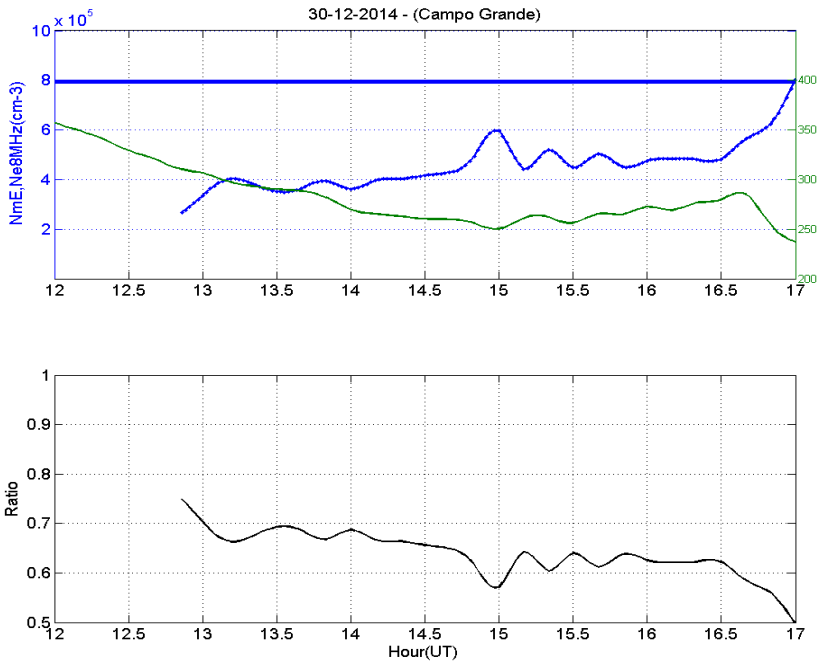

Figure 5.8d - The same as Figure 5.8 but for day 30.

It is well know that the E layer of the ionosphere is sometimes attributed with the presence of enhanced ionized density known as the sporadic E (Es) (RISHBESTH AND GARRIOTT, 1969). This layer sometimes could also be attributed with much higher density known as blanketing type sporadic E (Esb) which could sufficiently block the upper ionospheric F layer from radio wave propagation and causes the disappearance of the F trace in an ionogram (TSUNODA, 2008). During this period of blanketing type Esb, the electric field in the F region is totally short circuited because of a very large conductivity in the geomagnetically connected E region. As a consequence, the F conductivity at this period is expected to be very low (compared to the E region conductivity) such that electric field in the F region is minimum and mapping of electric field from one hemisphere to the other in the F region would be impossible. On this basis, in the following discussion, we investigate this above hypothesis as a possible evidence of the daytime MSTIDs mapping mechanism.

To provide support to the above hypothesis, we use the critical frequency of Es layer (foEs) and the blanketing frequency of the Es layer (fbEs). The fbEs corresponds to the frequency from which the reflections from a higher layer than the Es layer begins to appear. This allows us to determine if there are strong or weak Es during the period of the observed MSTIDs mappings (i.e. 12 – 17 UT). The results of foEs and fbEs for 17, 18, 27, 28 and 30 December 2014, which correspond to days with MSTIDs mapping (17, 18, 27 and 28) and the day without MSTIDs mapping (30) are shown in Figure 5.9.

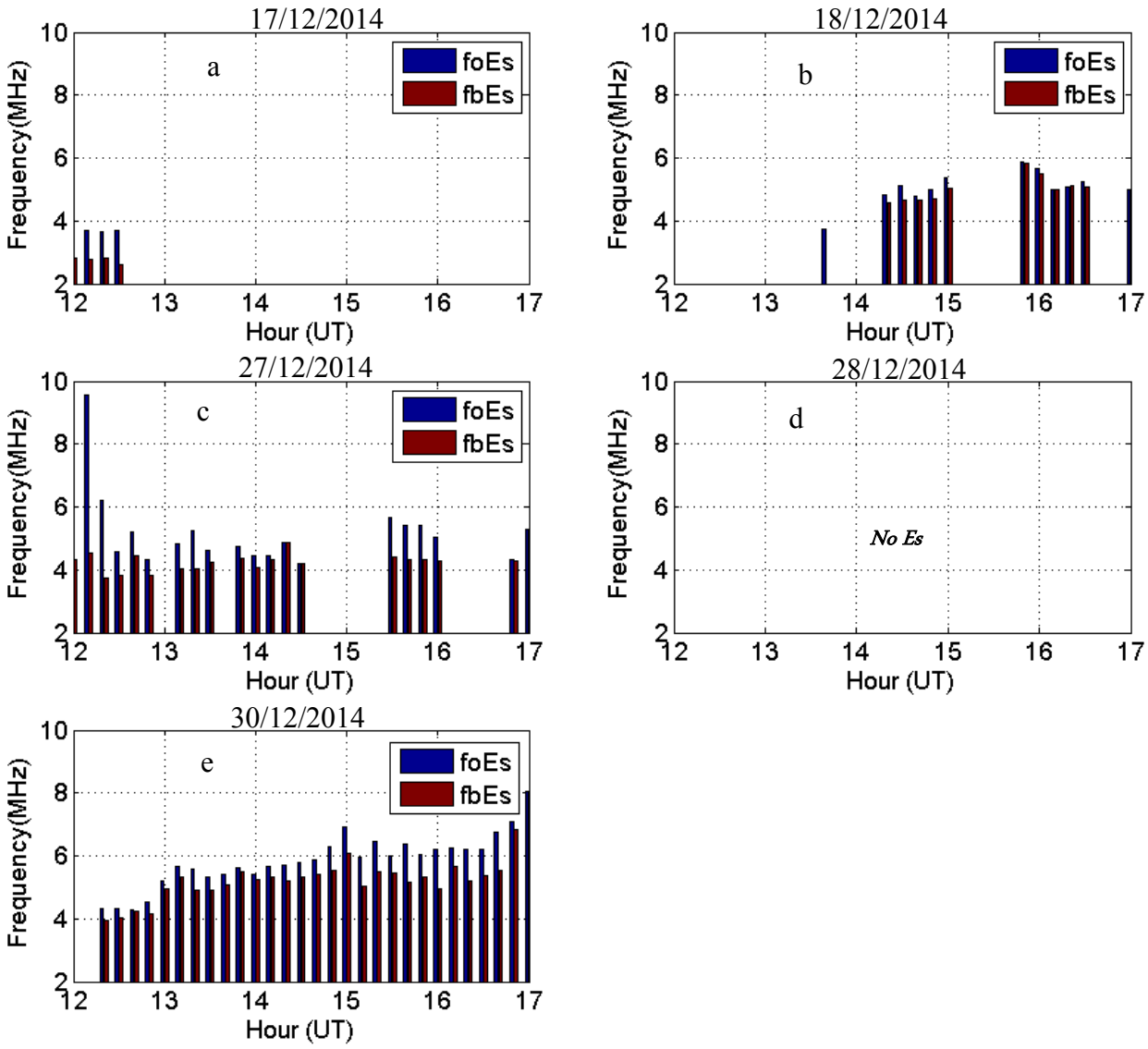

Figure 5.9 - Results of foEs (blue) and fbEs (red) for days 17, 18, 27, 28 and 30 December 2014

Figure 5.9 (a,b,c, and d) show weak activities of Es during the period of the MSTIDs mapping on days 17, 18, 27, and 28 respectively, while Figure 5.9(e) shows strong Es activity and provides the reason why there are no MSTIDs mapping activity during this same day as show in Figure 5.10. The Figure 5.10

shows no mapping activity as a result of the strong Es activity which is believed to have prevented the Ep generation/mapping in the F region during the period.

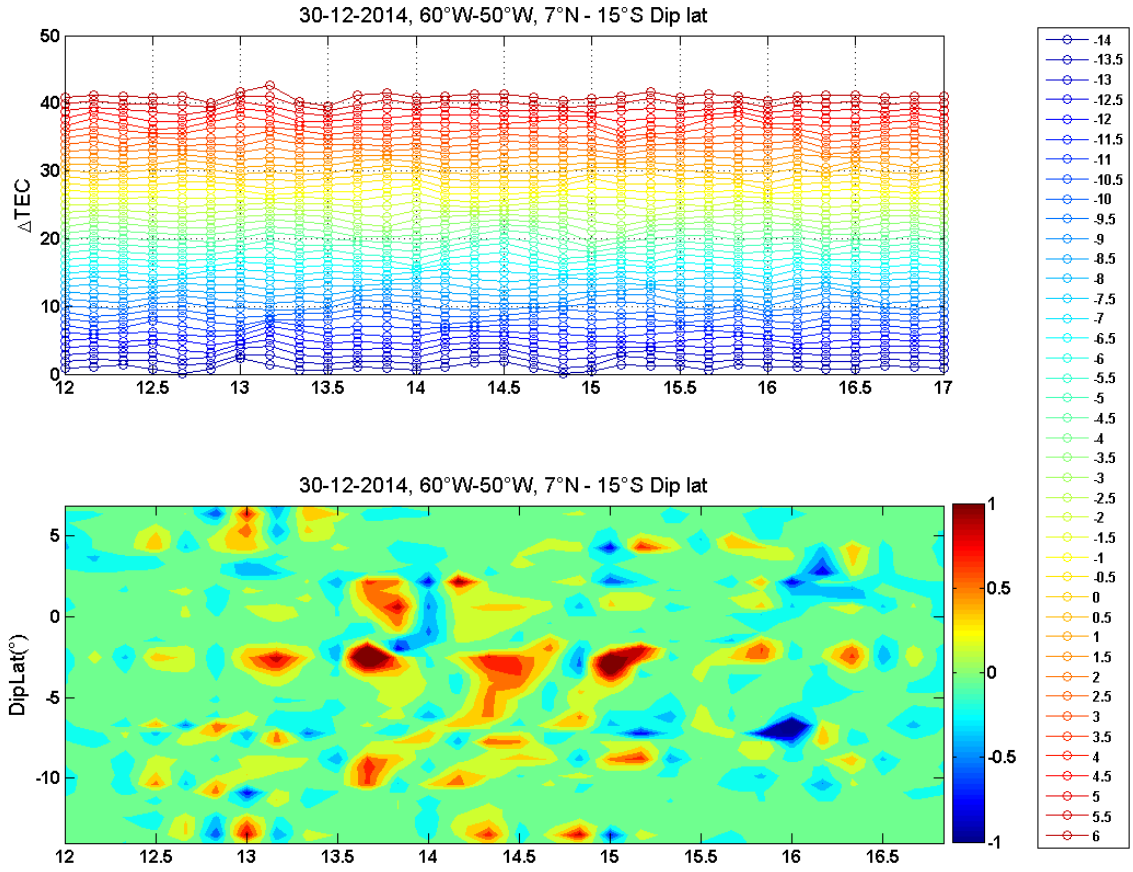

Figure 5.10 - MSTIDs activity on 30 Dec. 2014 showing no clear MSTIDs mapping.

Figure 5.10 is the MSTIDs activity on 30 Dec, 2014 during 12 to 17 UT which shows a clear MSTIDs activity without mapping to the conjugate hemisphere. This non mapping activity is believed to be as a result of strong Es layer which made a total blockage of the F region during this period of time. This provides a clear evidence that the strong Es activity overwhelmed the F region conductivity and prevented the Ep generation/mapping in the F region during the MSTIDs activity period and prevent the mapping of MSTIDs to conjugate hemisphere.

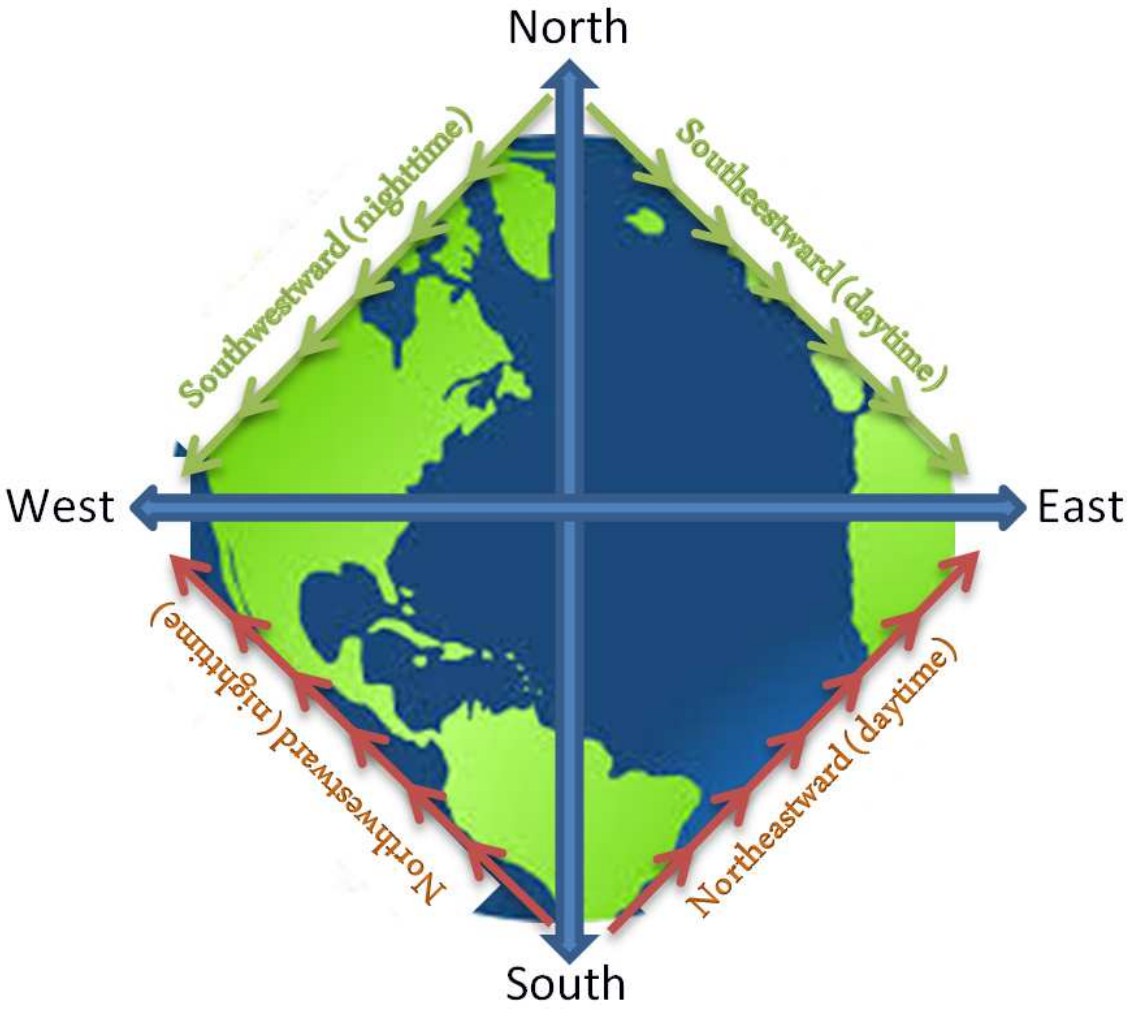

Figure 5.11 - The green arrows represent the MSTIDs preferred directivity during nighttime (top left) and during daytime (top right) at the northern hemisphere; the red arrows represent the preferred directivity of MSTIDs during nighttime (bottom left) and during daytime (bottom right) at the southern hemisphere.

Figure 5.11 shows that most nighttime MSTID propagating directions are equatorward and southwestward in the northern hemisphere and equatorward and northwestward in the southern hemispheres (on the LHS). This property of MSTIDs has been well accepted in the northern hemisphere. However, with the contributions from Hernandez-Pajares et al. (2006, 2012) and from our present study (JONAH et al., 2016), it is clear that the daytime MSTIDs also propagate to the same direction in both hemispheres that is, the MSTIDs are equatorward and eastward in the southern hemisphere (on the RHS).

6.0 GRAVITY WAVES OBSERVATION AND THEIR SOURCE INVESTIGATION

Based on the observations of MSTIDs using primarily the GNSS data, this chapter focuses on AGW observation and their source investigation. The source mechanisms of AGW responsible for the MSTIDs are investigated by identifying GWs signatures from isolines of digisonde, identifying few tropospheric events based on convection activities (GOES satellite) and finally comparing a tropospheric convective day to a non-tropospheric convective day.

TIDs are known to be the manifestation of the Atmospheric Gravity Waves (AGWs) arising either from underlying troposphere or from the auroral region (HUNSUCKER, 1982; HUANG et al., 1994; MILLER et al., 1997). We use geomagnetic quiet days only to eliminate the forcing from auroral region. In recent years, the MSTIDs are observed during the tsunamis and they are diagnosed as owing to the AGWs forcing from below (MAKELA et al., 2011; KHERANI et al., 2011). Therefore, the AGWs are preferred forcing to generate the daytime MSTIDs. The sources for the AGW have been proposed to be largely from upward propagating meteorological processes (e.g. orography and convection activities in the troposphere and stratosphere). Recently studies have attempted to provide various sources for AGW/TID. According to MacDougall et al., (2009b) AGWs could be driven by wind component along the magnetic field direction, or through longitudinal mobility which are indirectly produced via convergence–divergence of ionization. The AGW can also be generated by the sunrise and sunset terminators (MACDOUGALL et al., 2009a) or be seeded by the Inter Tropical Convergence Zone (ITCZ) (MACDOUGALL et al., 2011). Hence, it is possible to infer that mechanisms causing AGW depend on the location, period or season of the AGW/TIDs event. In the section that follows, we first show the signature of AGW during the same period of the observed MSTIDs as a clear link between AGW-MSTIDs, and later investigate the possible mechanism responsible for the AGW generation.

6.1 AGW activity during day 5 and day 6

According to Lanchester et. al., (1993) and Hocke and Schlegel (1996), one can verify AGW by looking at data from two frequencies and checking that they show downward phase motion. For this objective we selected a low-to-mid-latitude station Cachoeira Paulista (45°W, 23°S, shown as red circle in Figure 4.1) and we examine the time variation of the ionospheric height observed by the digisonde during days Dec 5 and 6, corresponding to days of observed MSTIDs.

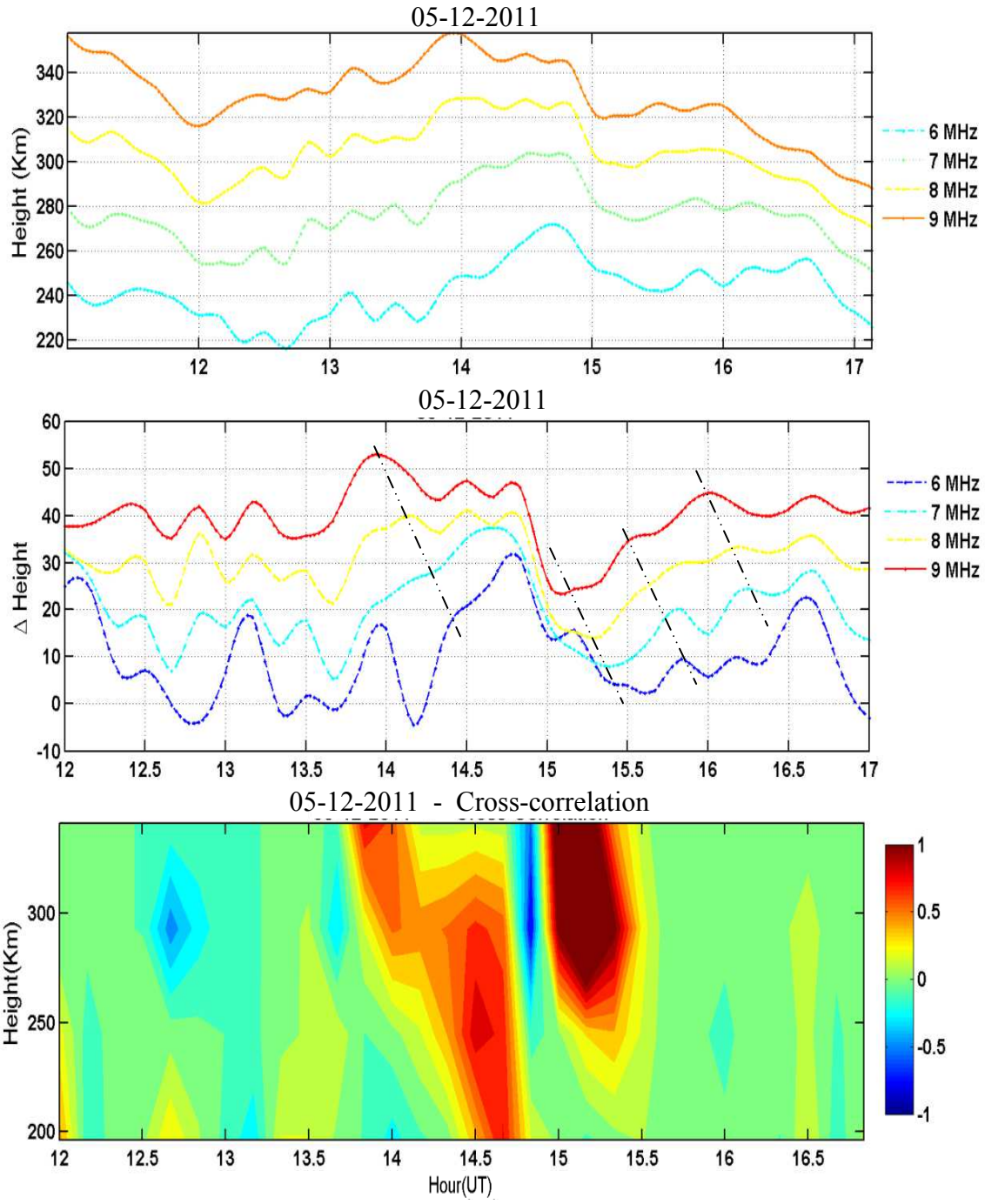

Figure 6.1 - From the top, the first panel shows for D5 the hF (height) of 6 to 9 MHz as a function of time, the second panel represents the Δheight and the third panel represent the cross-correlation coefficient map of Δheight in space and time using the same method of section 3.0.

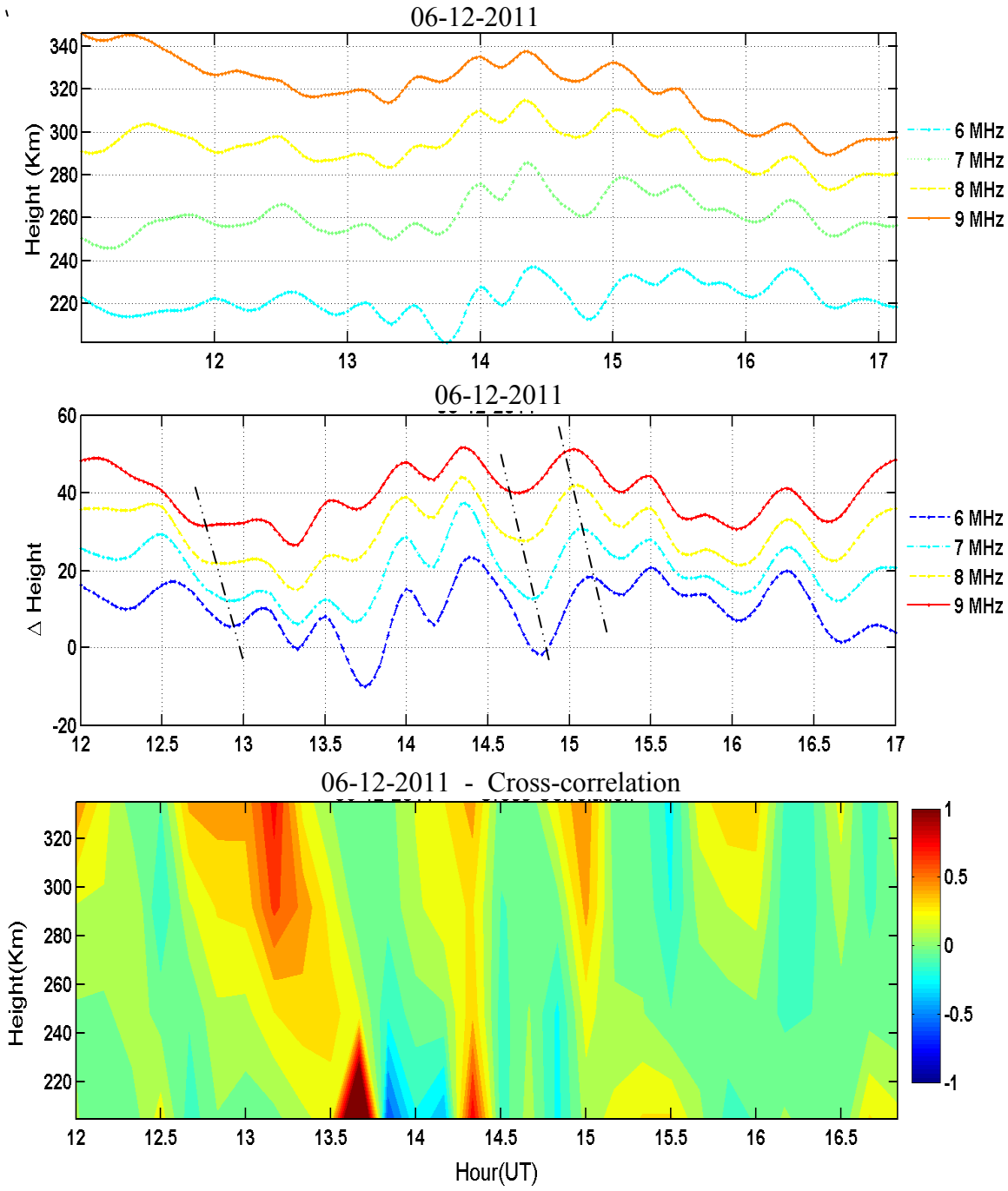

Figure 6.2 - The same as Figure 6.1, but for D6.

Figures 6.1 and 6.2 present the results from the digisonde on these two days during 12-17 UT. In these figures, the top-to-bottom panels depict the temporal variation of the height *(h)* of the F region at 6-9 MHz frequencies, corresponding Δh variation and the cross-correlation map of Δh, respectively. The Δh is defined as the *h* deviation from the best-fitted (polynomial of order 7) h at each frequency.

From these figures, we note that the Δh acquires the oscillatory nature with large amplitude during 14-16 UT on day 5 and during 13-15 on day 6. Moreover, the cross-correlation of Δh maximizes in these time intervals when the peak of Δh shifts downward as time progresses to the lower altitude suggesting the downward phase propagation of the wave responsible for the oscillation. The downward phase propagation is a unique characteristic of the upward propagating AGWs and therefore the noted oscillations of the height of the F region ionosphere during 14-16 UT on D5 and during 13-15 UT on D6 (see Figures 4.1 and 4.2) are caused by the upward propagating AGWs. It is important to point out that the MSTIDs begin to appear at 14 and 13 UT, respectively on D5 and D6. Therefore, their appearance coincides with the appearance of the downward phase propagation of Δh. This is an important experimental outcome of this thesis which supports the possible association between AGWs and MSTIDs. More evidences of this association will be provided by simulation in chapters 7 and 8 of this study.

6.1.1 AGW activity during day 27 for the conjugate MSTIDs

The investigation carried out at section 6.1 to investigate the AGW activity during the MSTIDs event, is also carried out for the conjugate MSTIDs observations discussed in section 5.1. For this, we use the conjugate digisonde instruments located at Boa vista (northern hemisphere) and at Campo Grande (southern hemisphere) as shown in Figure 5.3.

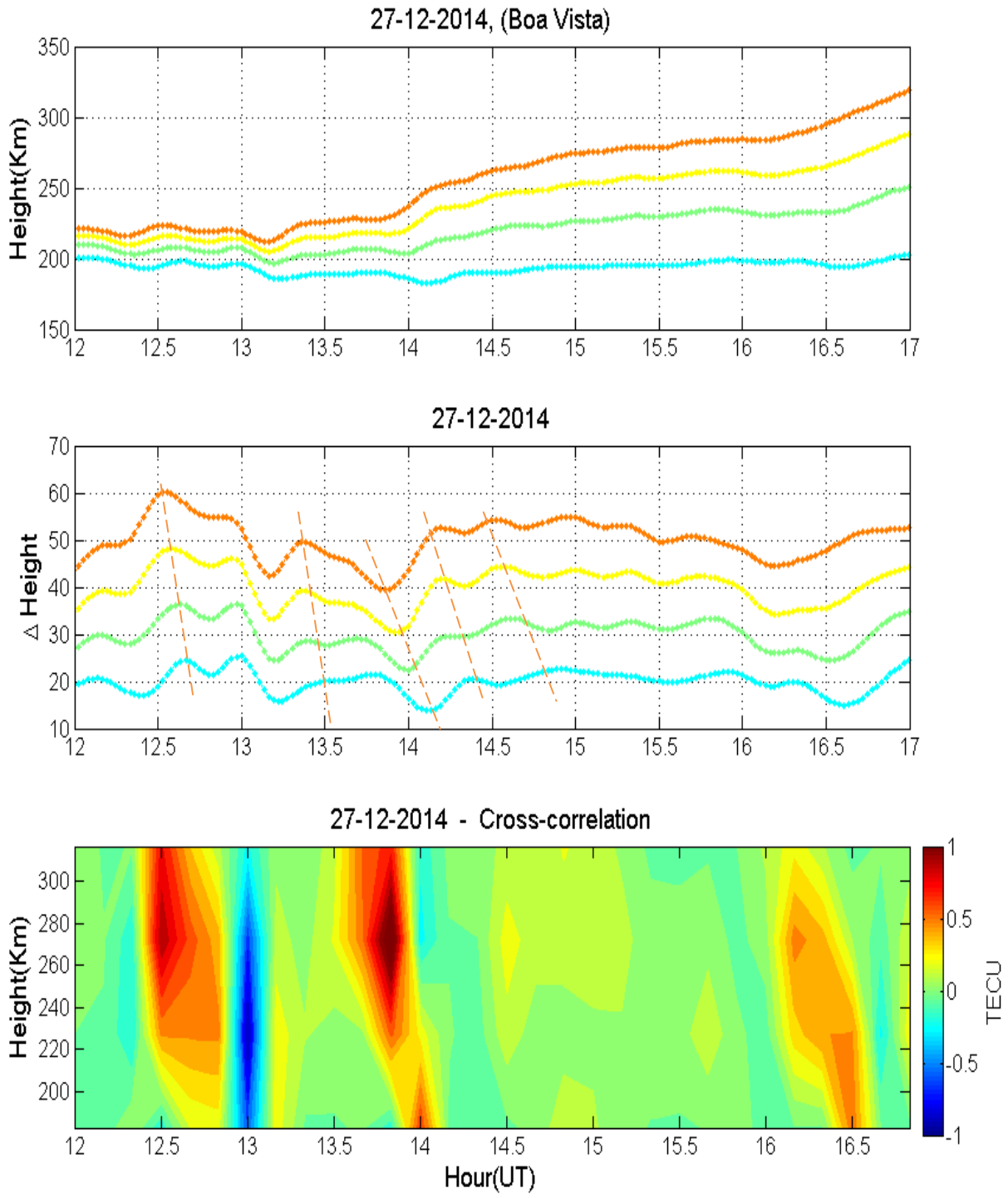

Figure 6.3 - The same as Figure 6.1, but for day 27 – Boa vista.

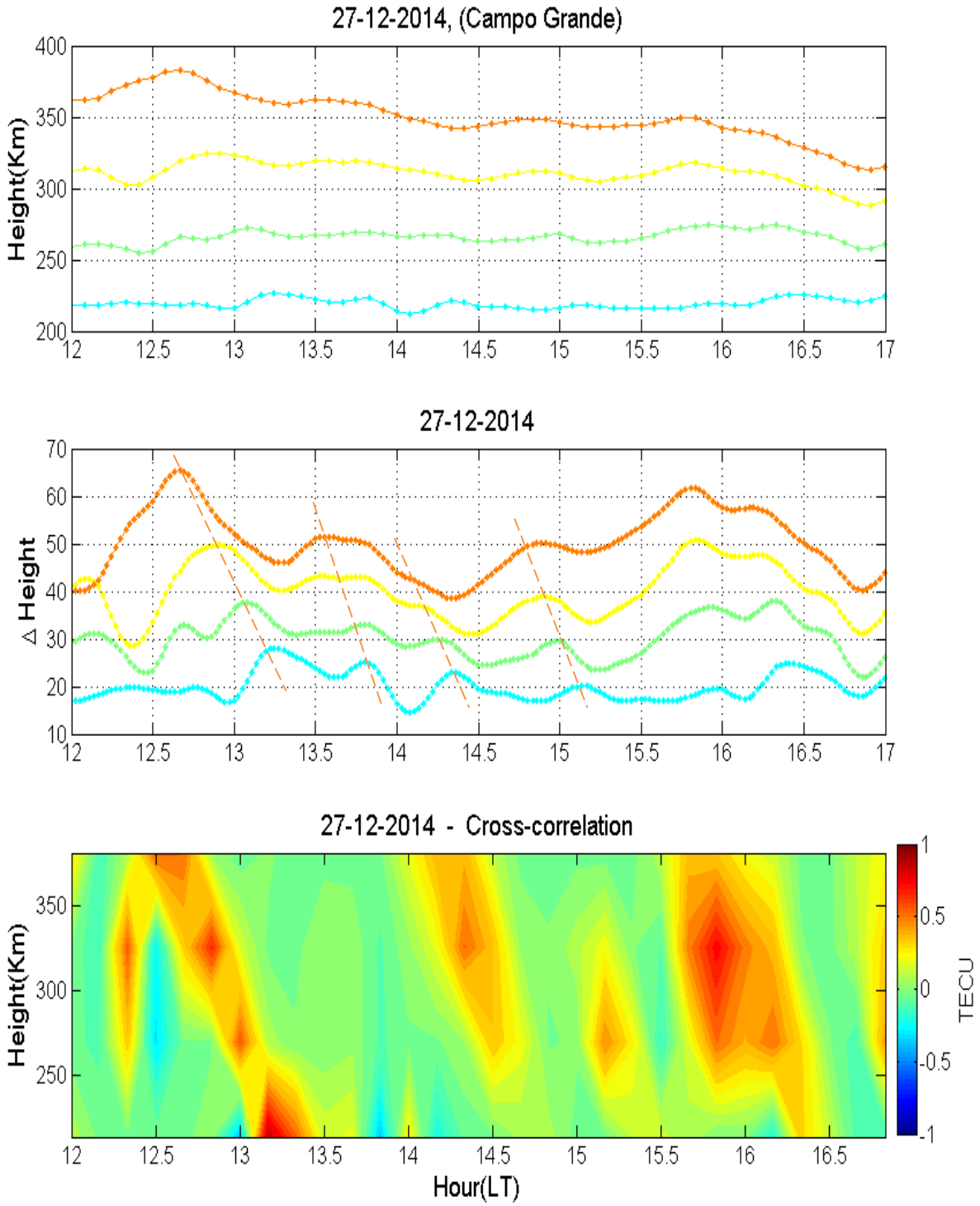

Figure 6.4 - The same as Figure 6.1, but for day 27 – Campo Grande.

At both Figures 6.3 and 6.4, it is possible to note the presence of AGW as shown by the downward propagation in the Δh and the cross-correlation at both hemispheres (i.e. at Boa vista and Campo Grande). However, the Campo Grande cross-correlation shows stronger downward propagations than the Boa Vista. This is a significant evidence that the AGW forcing is stronger at the southern hemisphere therefore the observe MSTIDs discussed at section 5.0 are actually generated from the southern hemisphere. It is also important to note that the MSTIDs which begin to appear at ~12 UT on D27 coincides with the appearance of the downward phase propagation of Δh. Similar characteristics were noted in section 6.1 (Figure 6.1 and 6.2), and this gives consistent supports on the possible association between AGWs and MSTIDs.

6.2 Possible AGW mechanism and coupling

As discussed in section 6.0 and 6.1, convective activity is one of the most important seeding for AGW. According to Vadas et. al. (2009) deep clouds near the tropopause region are indicative of regions of active convection and a likely source of gravity waves. Cold brightness temperature suggests deep convective plumes and convective overshoot which are a convenient launching platform for gravity waves (FRITTS et al., 2009). AGW generated from the convective sources can propagate into the higher altitude and penetrate deep into the upper atmosphere (YIGIT et al., 2008; FRITTS et al., 2009). In this section we extend our investigations on the findings of the enhanced MSTIDs around noon time due to AGW enhancement at the same time period as presented above. Using GOES 13 and COSMIC satellite data, our convective activity is defined from the water vapor and infrared temperature data which are obtainable from the CPTEC/INPE web site. A strong convection activity implies that the difference in water vapor (WV) and infrared (IR) is greater than 0°C, i.e. WV – IR > 0°C, while a weak convection activity implies that WV – IR < °C. We selected 7 days of strong tropospheric convection and 2 days of weak tropospheric convection (as shown in Figures 6.5 and 6.6). First we show the evidence of tropospheric convection as an important factor for gravity wave

generation by showing the correlation between the GOES13 satellite data, digisonde and GPS-TEC data during the period of MSTID observations, and later present how these gravity waves propagate from the tropospheric altitudes upward to regions of the thermosphere by using the COSMIC satellite data to represent the amplitude, period and energy propagation of AGW around the regions of the observed MSTIDs.

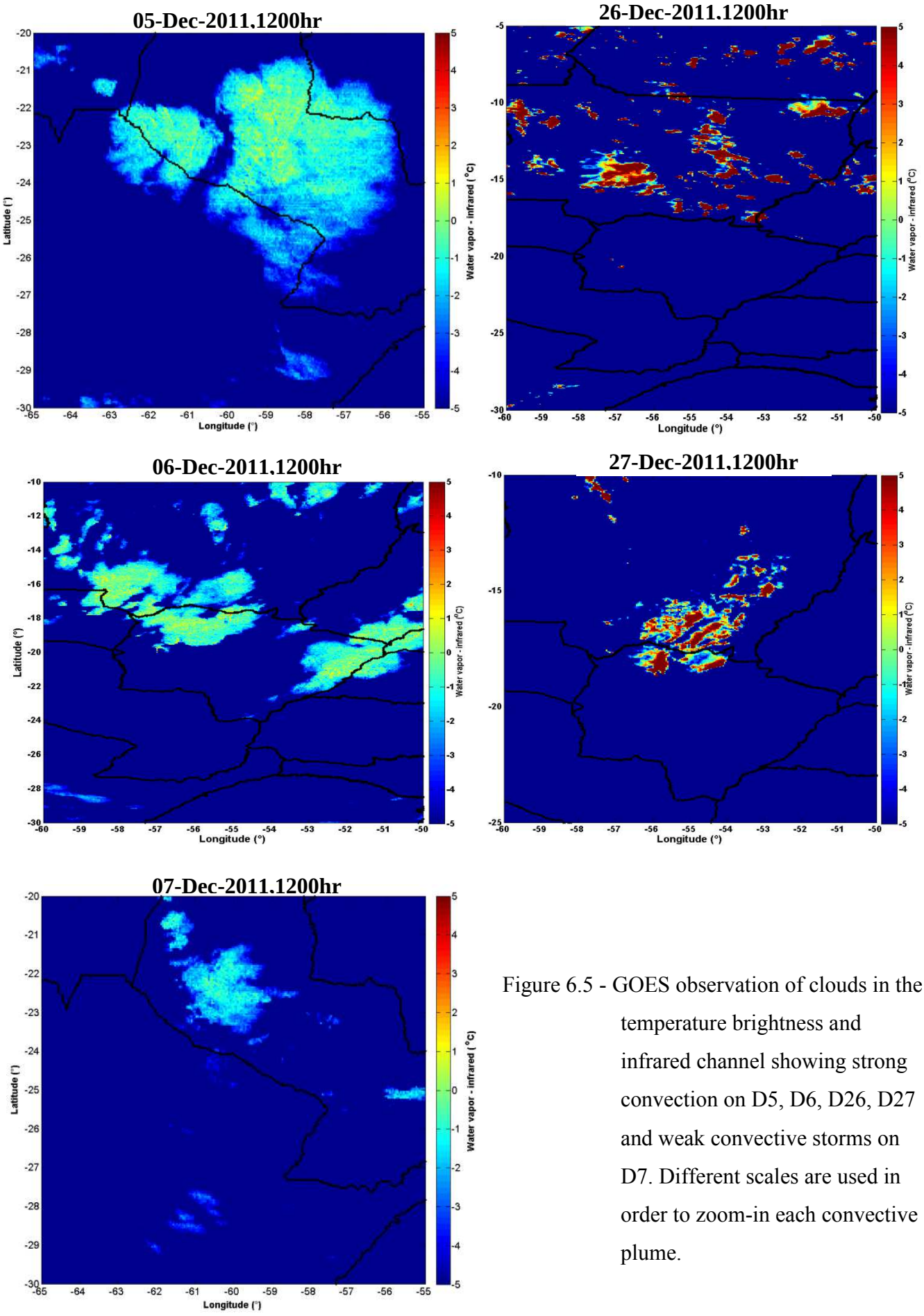

Figure 6.5 - GOES observation of clouds in the temperature brightness and infrared channel showing strong convection on D5, D6, D26, D27 and weak convective storms on D7. Different scales are used in order to zoom-in each convective plume.

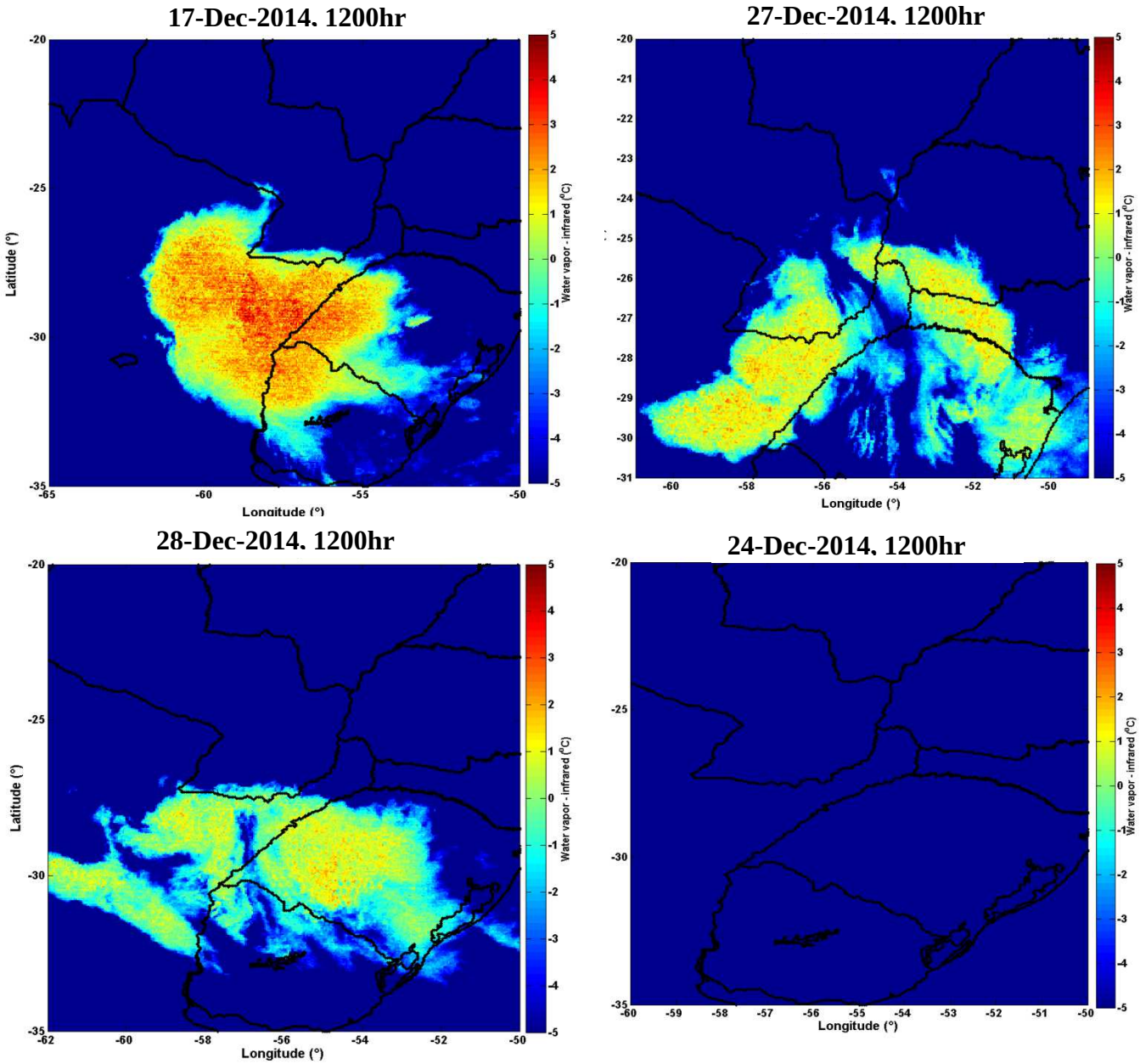

Figure 6.6 - GOES satellite observation of clouds in the temperature brightness and infrared channel showing strong convection on D17, D27, D28 and weak convective storms on D24.

Figure 6.7 shows the comparison of strong convective activity (panel a), gravity wave activity presented by variation in the true height (panel b) and the MSTIDs represented by the GPS data (panel c) on day 5 of 2011 and with weak convection activity (panel d), gravity wave activity presented by variation in the true height (panel e) and the MSTIDs represented by the GPS data (panel f) on day 7 of 2011. The deep and weak convection activities are seen very close to the site of the AGW and MSTIDs observation. By comparing Figure 6.7a to 6.7c, it is possible to clearly observe that the AGW and the MSTIDs activities on a strong convection day is much well defined than on a weak convection day represented by Figure 6.7d to 6.7f. This suggests clear evidence of strong convection activity as an important factor of AGW seeding and consequent MSTIDs activity. It is also possible to note that the cloud distribution locations are correlated with the observed propagation direction of the MSTIDs particularly that of the eastward directions.

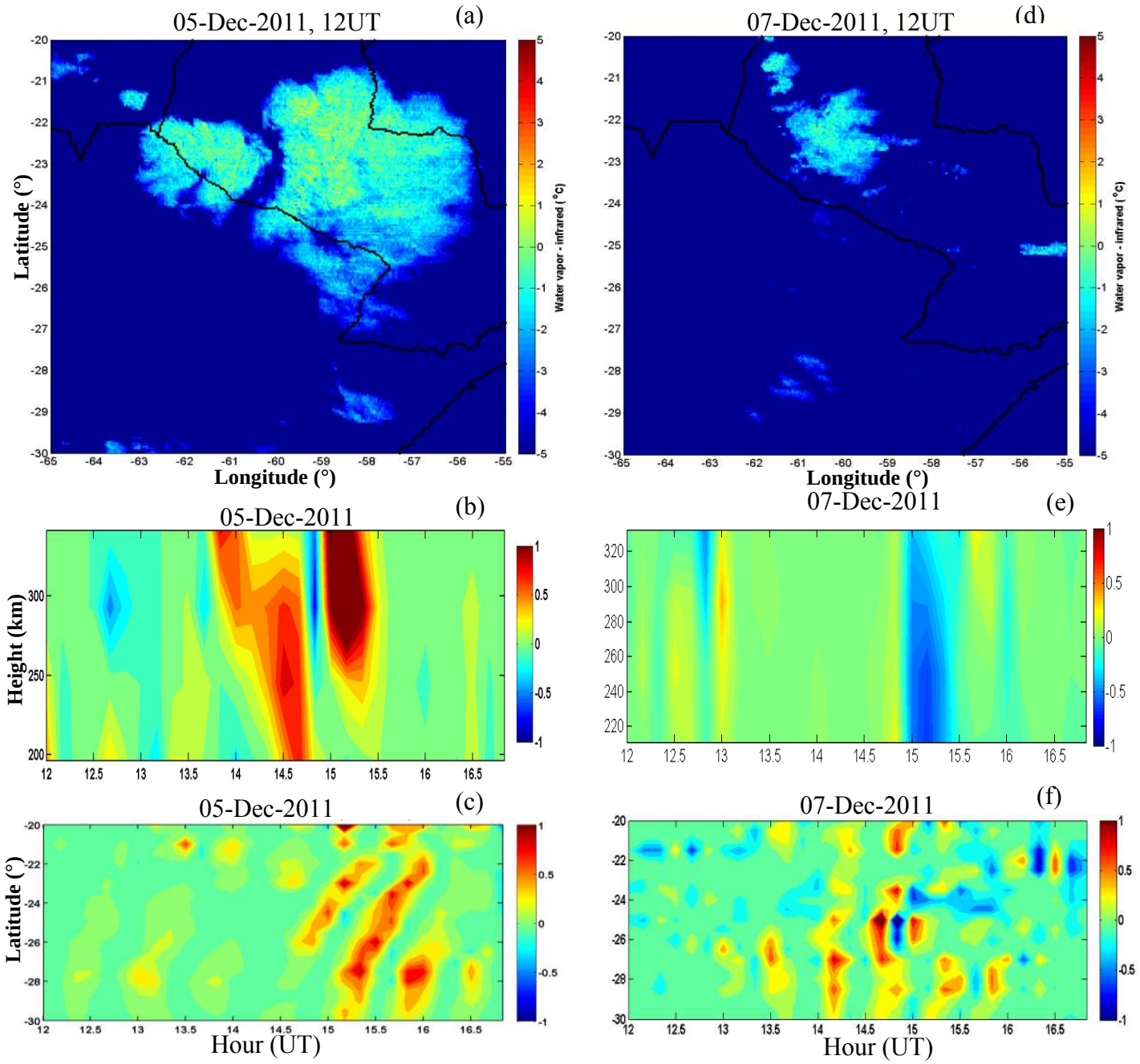

Figure 6.7 - Comparison of the observed strong convective storm on D5 and the weak convective storm on D7 with their respective cross-correlation of Δh and ΔTEC.

A similar investigation is made for the conjugate MSTIDs during 16th and 24th 2014 as shown in Figure 6.8. They show the comparison of strong convective activity (panel a), gravity wave activity presented by variation in the true height (panel b) and the MSTIDs represented by the GPS data (panel c) on day 16 of 2014 and with weak convection activity (panel d), gravity wave activity presented by variation in the true height (panel e) and the MSTIDs represented by the GPS data (panel f) on day 24 of 2014.

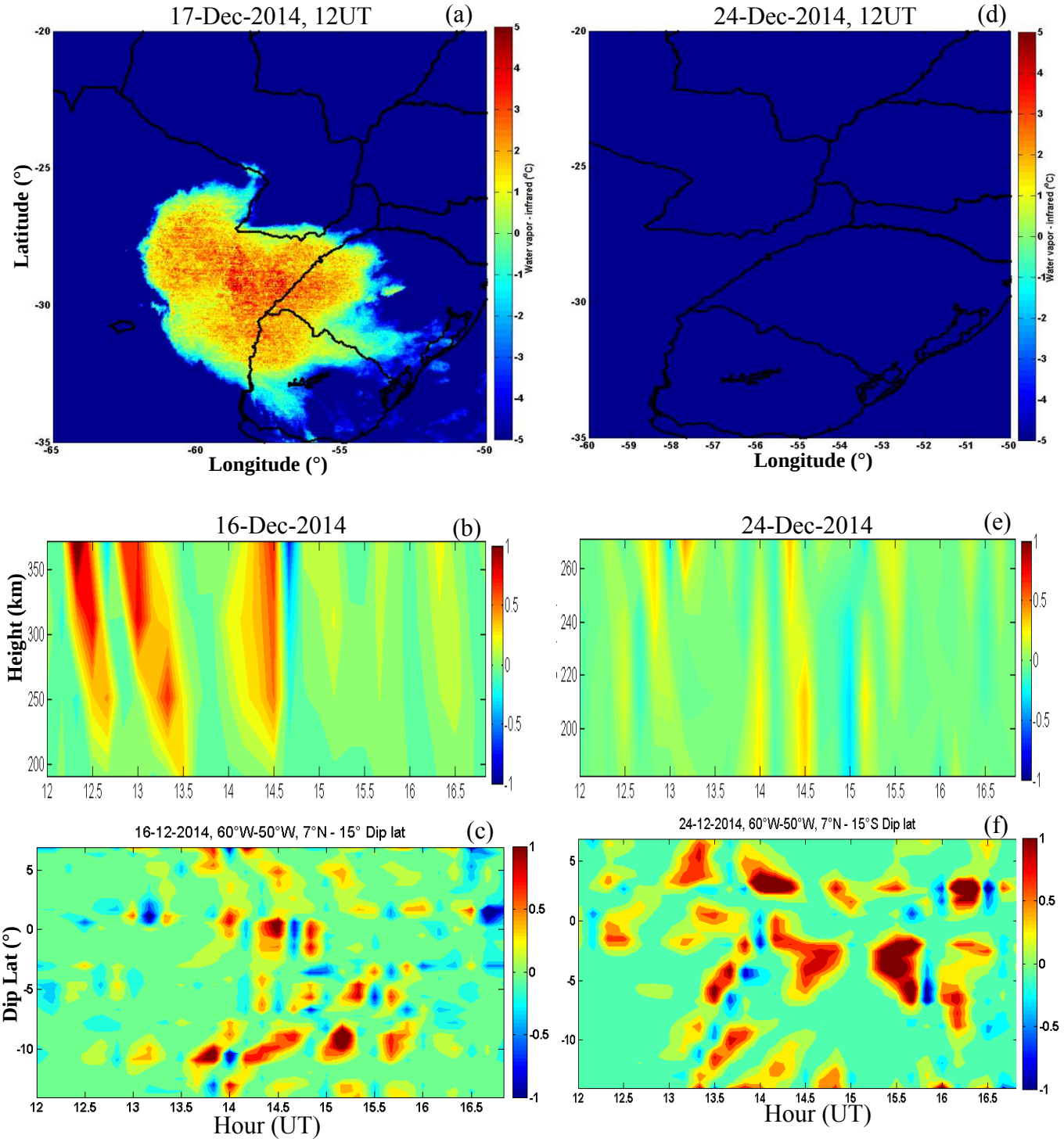

Figure 6.8 - Comparison of the observed strong convective storm on D17 and the weak convective storm on D24 with their respective cross-correlation of Δh and ΔTEC.

Figure 6.8a to 6.8c, show a clear and well defined AGW and MSTIDs activities on a strong convection day. On the other hand, Figure 6.8d to 6.8f it is possible to also observe some MSTIDs activities at Figure 6.8f even though Figure 6.8d shows no convection activity. Such activity could only be caused by strong convection activity in the northern part which is confirmed in the Figure 6.9 below.

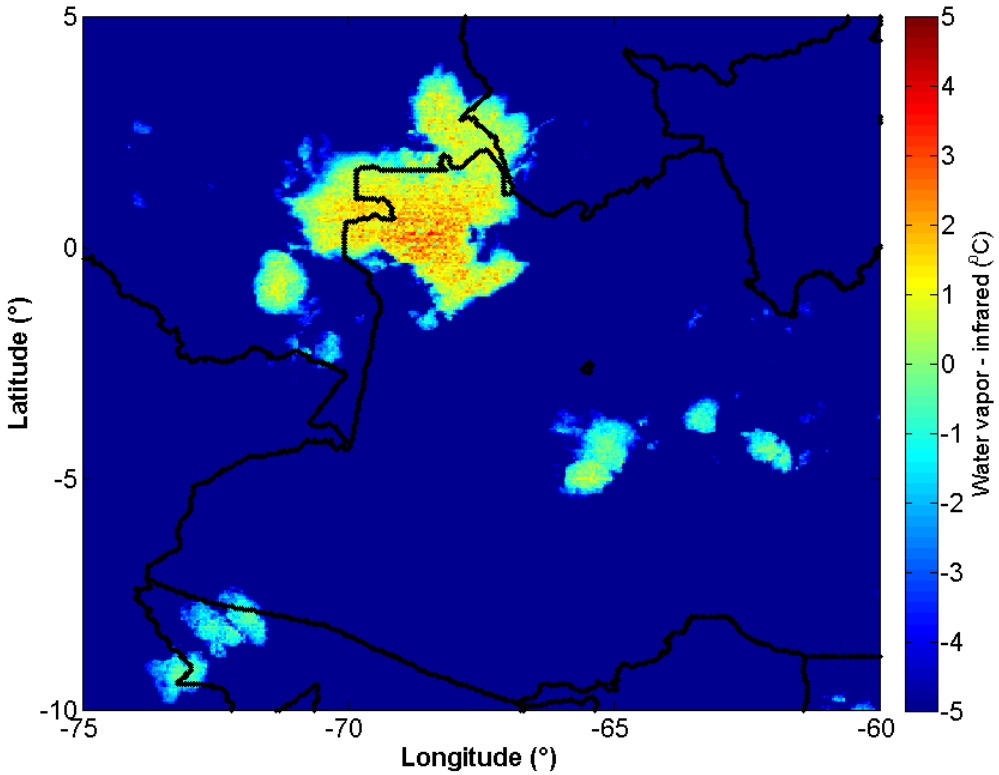

Figure 6.9 - GOES satellite observation of clouds in the temperature brightness and infrared channel showing deep convection activity on D24 over the north of Brazil.

It is important to mention that the convection activities shown above are not stationary but move in time as expected. Their movement is what excites the gravity waves. According to Vadas and Liu (2009), gravity waves could be excited when the air parcels (i.e. the deep convection plume) push the

stratospheric air upward just below and above the troposphere. An example of convection plume is shown in Figure 6.9a. The movement of the convective plume has also motion in the horizontal direction. This convective plume (showed in Figure 6.9a) moves ~5 ° in ~6 hour. This implies that it is moving with the velocity of ~25m/s or ~92 km/h. These movements could be one possibility of the AGW excitement observed in this study.

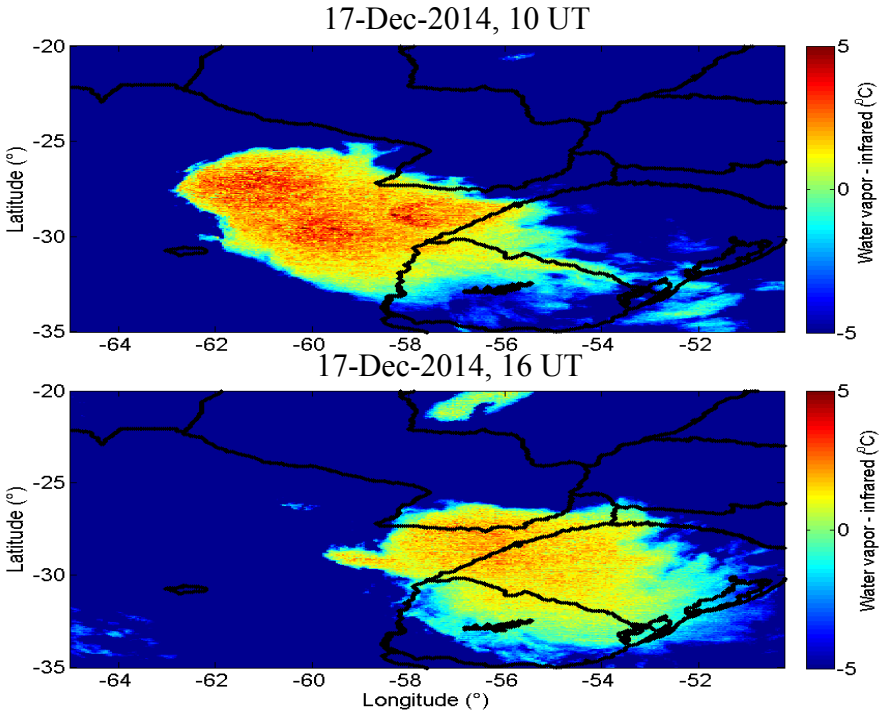

Figure 6.9a - Evolution of the tropospheric convection from 10 UT to 17 UT on day 17 of Dec. 2014.

6.3 Gravity wave propagations

The Constellation Observing System for Meteorology, Ionosphere, and Climate (COSMIC) mission provides ~2500 GPS radio occultation sounding per day which is good for carrying out climate analysis and ionospheric research (Fong et al, 2008). The radio occultation technique can be used to derive profile of electron density in the ionosphere, temperature profile up to 60 km height and temperature and water vapor in the tropospheric height. In this study we used

fluctuation in the temperature profile obtained by this radio occultation technique from COSMIC mission within the area (60°W- 40°W, 20°S 0°N) under investigation (see Figure 4.1) to study the gravity wave propagation from ground up to the stratospheric height. Figure 6.10. Illustrates our data analysis method.

Figure 6.10 (top) the pink solid curve represents the temperature profile (T) as recorded by the COSMIC mission. A polynomial filter (order = 7) is applied to yield a smooth background temperature profile (T_{mean}, Figure 6.10, blue curve). Figure 6.10 (middle) shows percentage of normalized temperature variations ($\%\delta T/T$), where δT is the differences between the pink and blue curves in Figure 6.10 (top). The power series using the Fast Fourier Transform (*FFT*) was used to determine the wavelength of the gravity waves as represented in the bottom panel. Figure 6.11 to Figure 6.20 represent the same corresponding parameters but for days 6, 26, 27, 7 December 2011 and 17, 18, 27, 28 and 25 December 2014. For easy comprehensive discussion, we refer 5, 6, 26, 27 and 7 December 2011 and 17, 18, 27, 28 and 25 December 2014 as D5, D6, D26, D27, D7 and D17, D18, D27, D28 and D25 respectively.

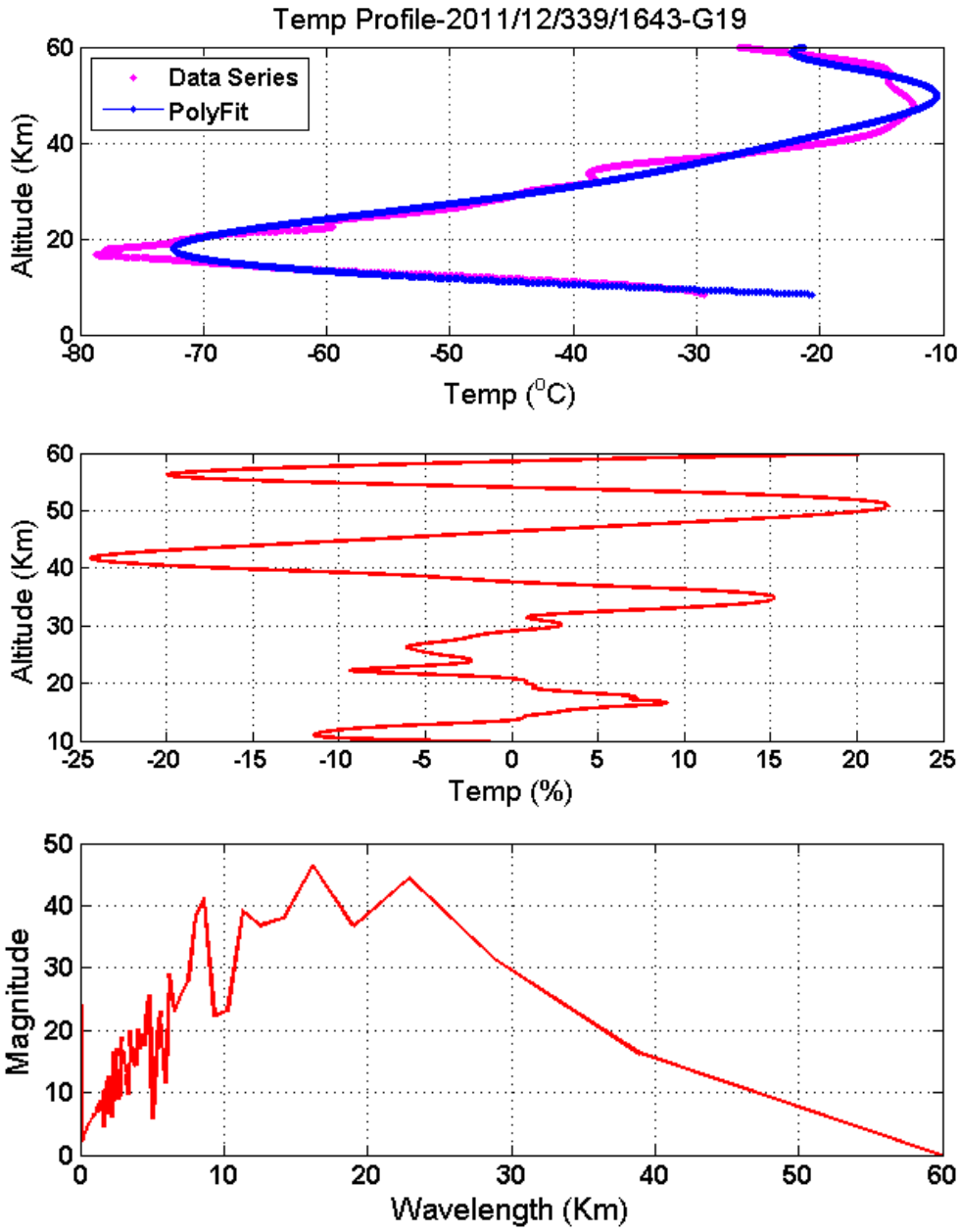

Figure 6.10 - From top panel, the temperature profile from COSMIC satellite (pink color) and it polynomial fit (blue color), middle panel - signature of upward AGW propagation as obtained from the detrended temperature profile, bottom panel - the peak of the wavelength obtained by taken the *FFT* analysis of the temperature profile for 5/12/2011.

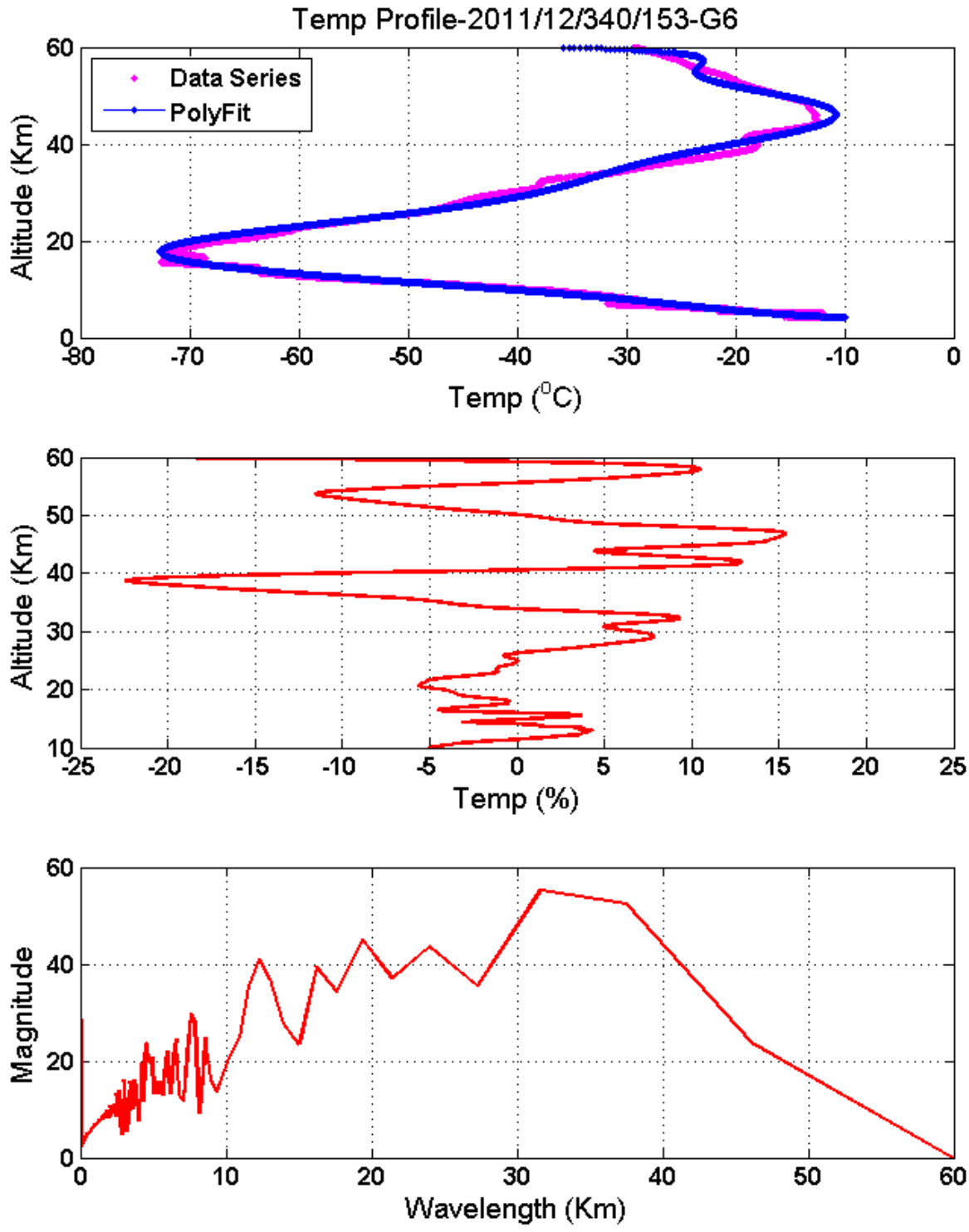

Figure 6.11 - The same as Figure 6.10 but for 6/12/2011.

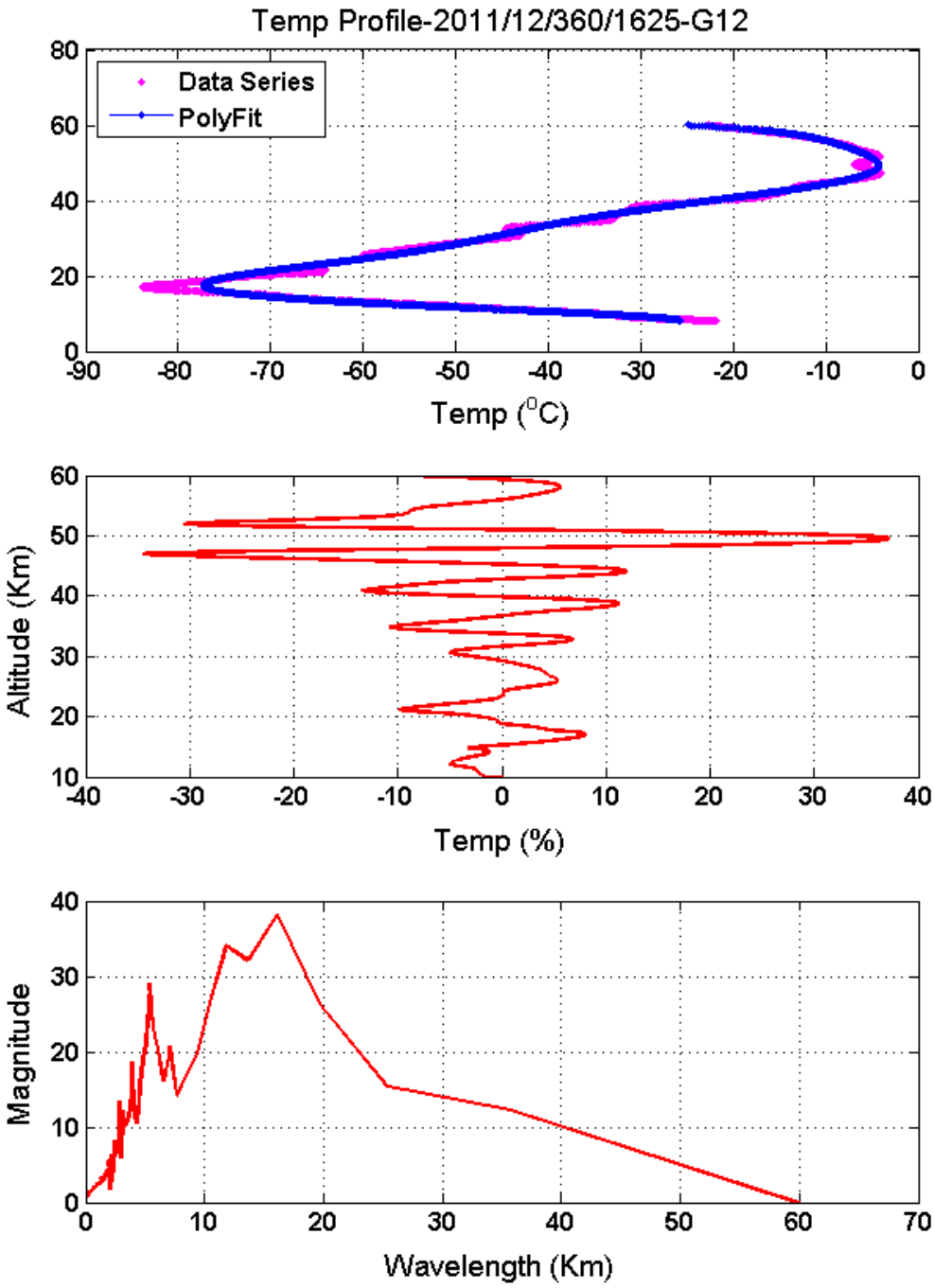

Figure 6.12 - The same as Figure 6.10 but for 26/12/2011.

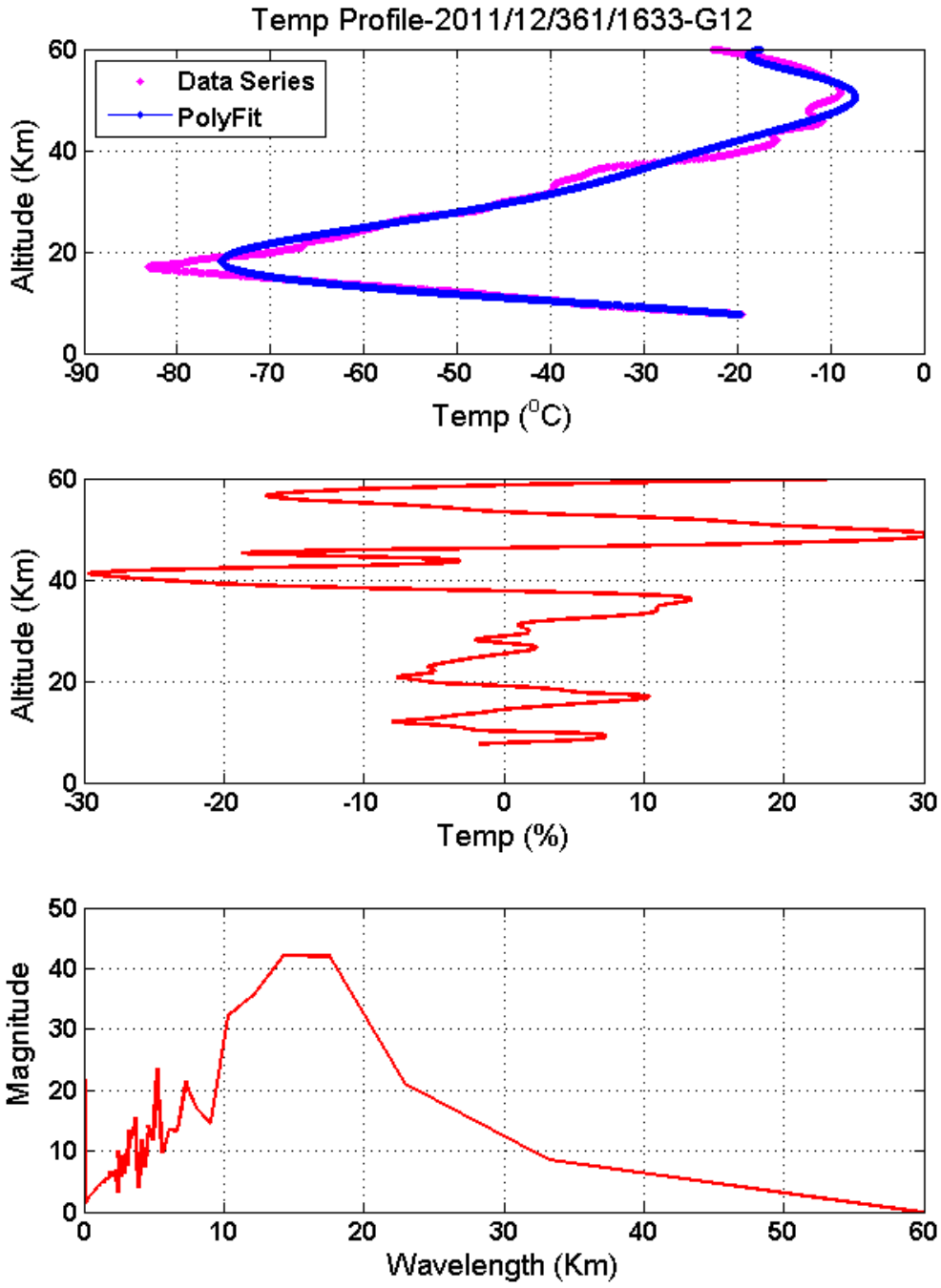

Figure 6.13 - The same as Figure 6.10 but for 27/12/2011.

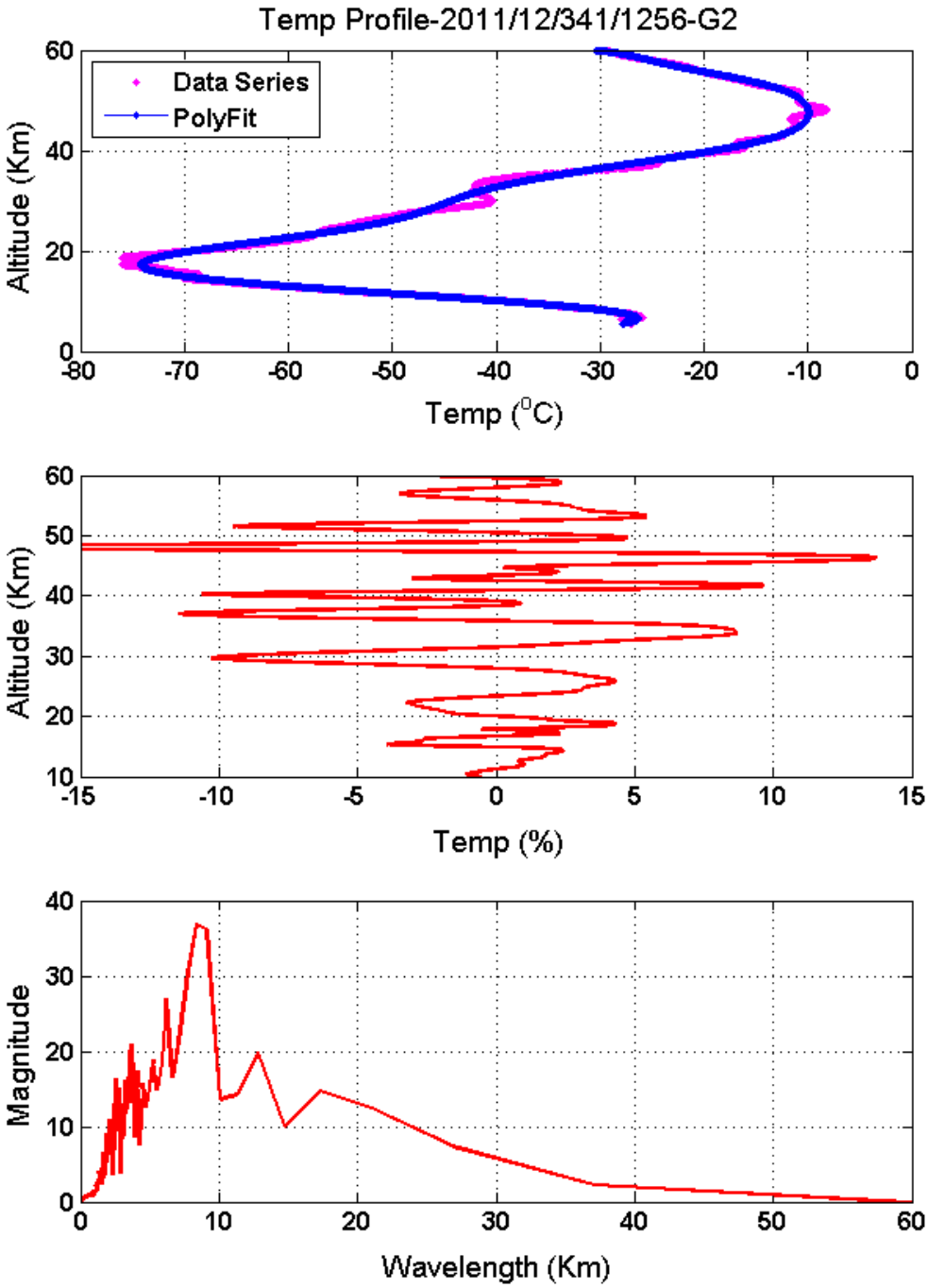

Figure 6.14 - The same as Figure 6.10 but for 7/12/2011.

The vertical mean temperature profiles below 8 km height are characterized by large difference in the measurements due to the presence of water vapor and large error probability of temperature retrieval at these heights. Hence, we have restricted our comparisons to height range between 10 km to 60 km. Many studies have shown that large-scale gravity waves (known as secondary gravity waves) are ubiquitous in the thermosphere during geomagnetic quiet periods (FORBES et al., 1995, BRUINSMA AND FORBES, 2008). These types of gravity waves are likely caused by the dissipation of upward propagating small-medium scale gravity waves (known as primary gravity waves) at the altitudes of 120 – 250 km, excited from tropospheric deep convection plume (VADAS AND LIU, 2009).

Figure 6.10 (middle panel) shows a percentage temperature increase from $\pm$10% at 10 to 20 km to $\pm$ 25% at 50 km. This type of altitude increase of change in temperature data can be interpreted as signature of vertical AGW propagation (WANG AND ALEXANDER, 2009). It is also possible to observe the wavelength of the AGW at the bottom panel. There are two prominent peaks of 18 and 23 km wavelength with a magnitude of 43-47. According to Fritts and Alexander (2003) gravity wave with this type of amplitudes would survive to the thermosphere region then dissipate energy in form of thermospheric body force (thermospheric body forces are the energy dissipation in the thermosphere as a result of kinematic viscosity, thermal diffusivity and ion drag). It could likely generate medium scale or large scale gravity waves and thus may be a source of MSTIDs and LSTIDs respectively (VADAS AND LIU, 2009). The same characteristics are observed at Figure 6.11 to Figure 6.13 with Figure 6.11 having the highest wavelength peak of 32 km, which is believed to be the strongest of the 4 events. These events shown in Figures 6.10 to 6.13 are corresponding to the days of strong tropospheric convections and MSTIDs activities as shows in section 4 and 5. However, Figure 6.14 shows the AGW activity on a weak tropospheric convection day (7/12/2011). It is possible to

observe from the middle and bottom panels of Figure 6.14 that the percentage temperature was less than +15% and the wavelength peak was less than 10 km. This is consistent with the weak tropospheric convection and the weak activity of MSTIDs on this day. It also proves that convection, AGW, and MSTIDs activities are connected and correlated.

To further investigate this connection between the convection, AGW and MSTIDs, we make similar plots using the COSMIC data for the days with strong convection (17, 18, 27, and 28, December 2014) and for the weak convection activity day of 25 December, 2014. The Figures are show in Figure 6.15 to Figure 6.19. The analysis for these Dec 2014 days provides supports for the conclusions inferred from the Dec. 2011 data.

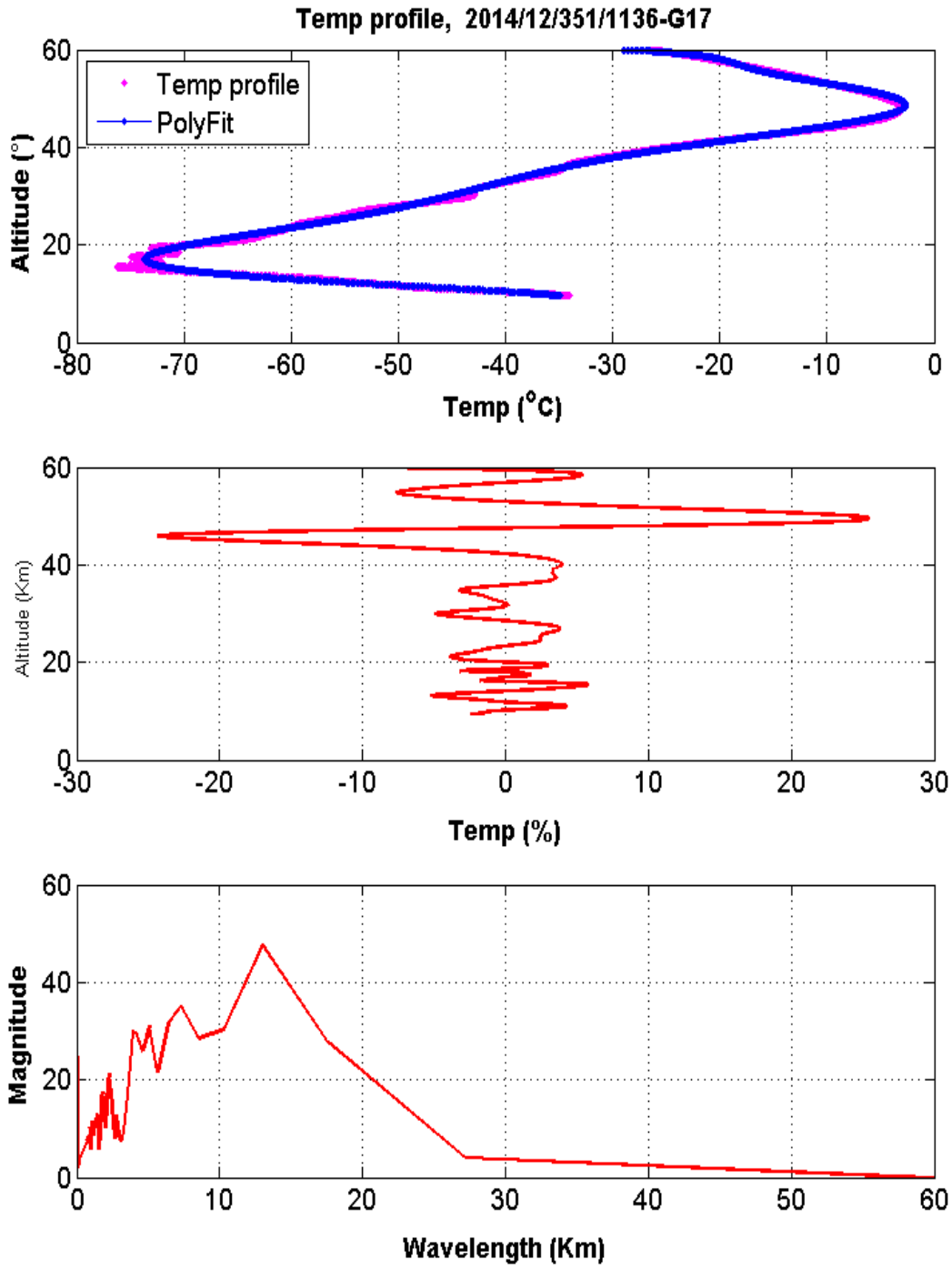

Figure 6.15 - The same as Figure 6.10 but for 17/12/2014.

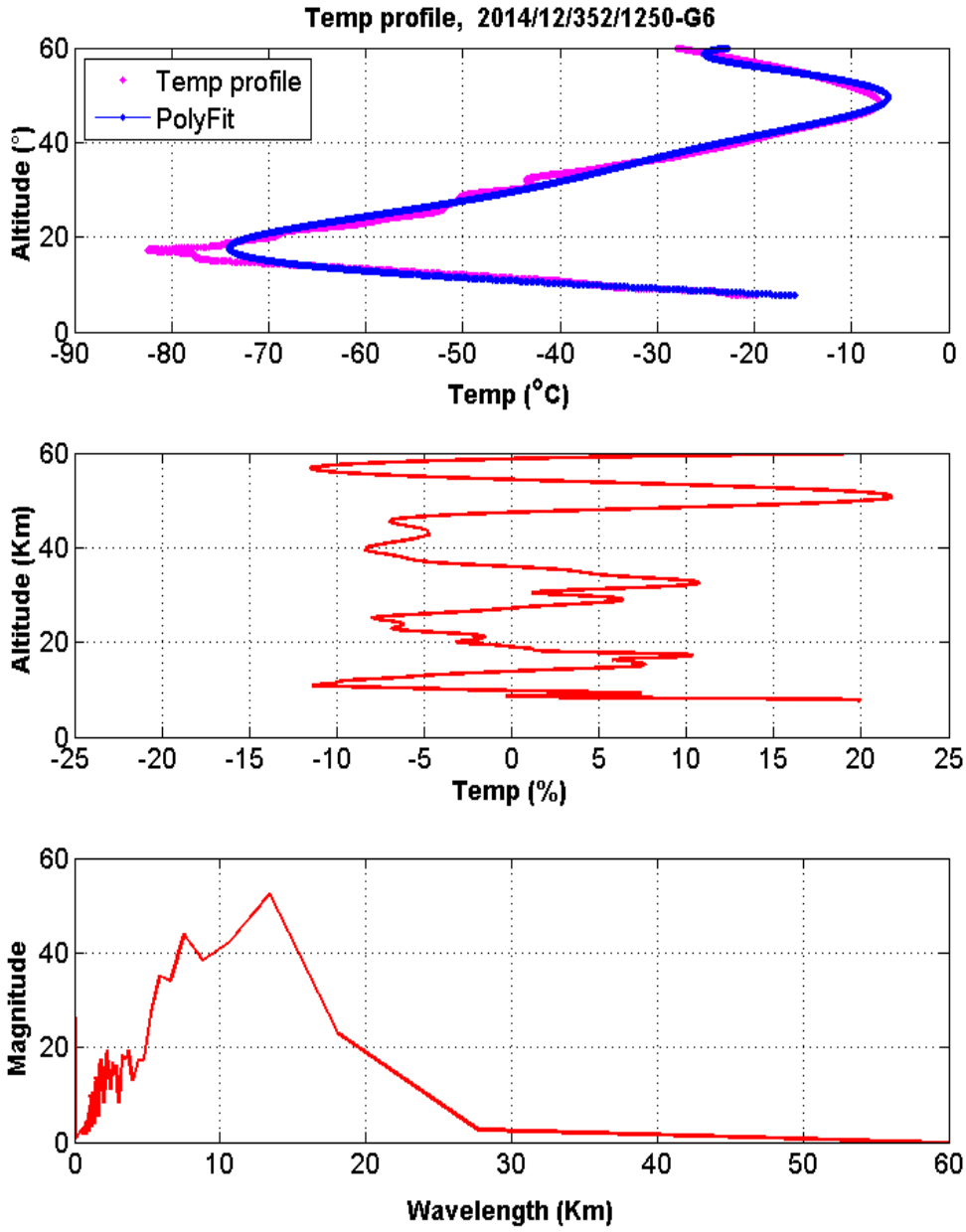

Figure 6.16 - The same as Figure 6.10 but for 18/12/2014.

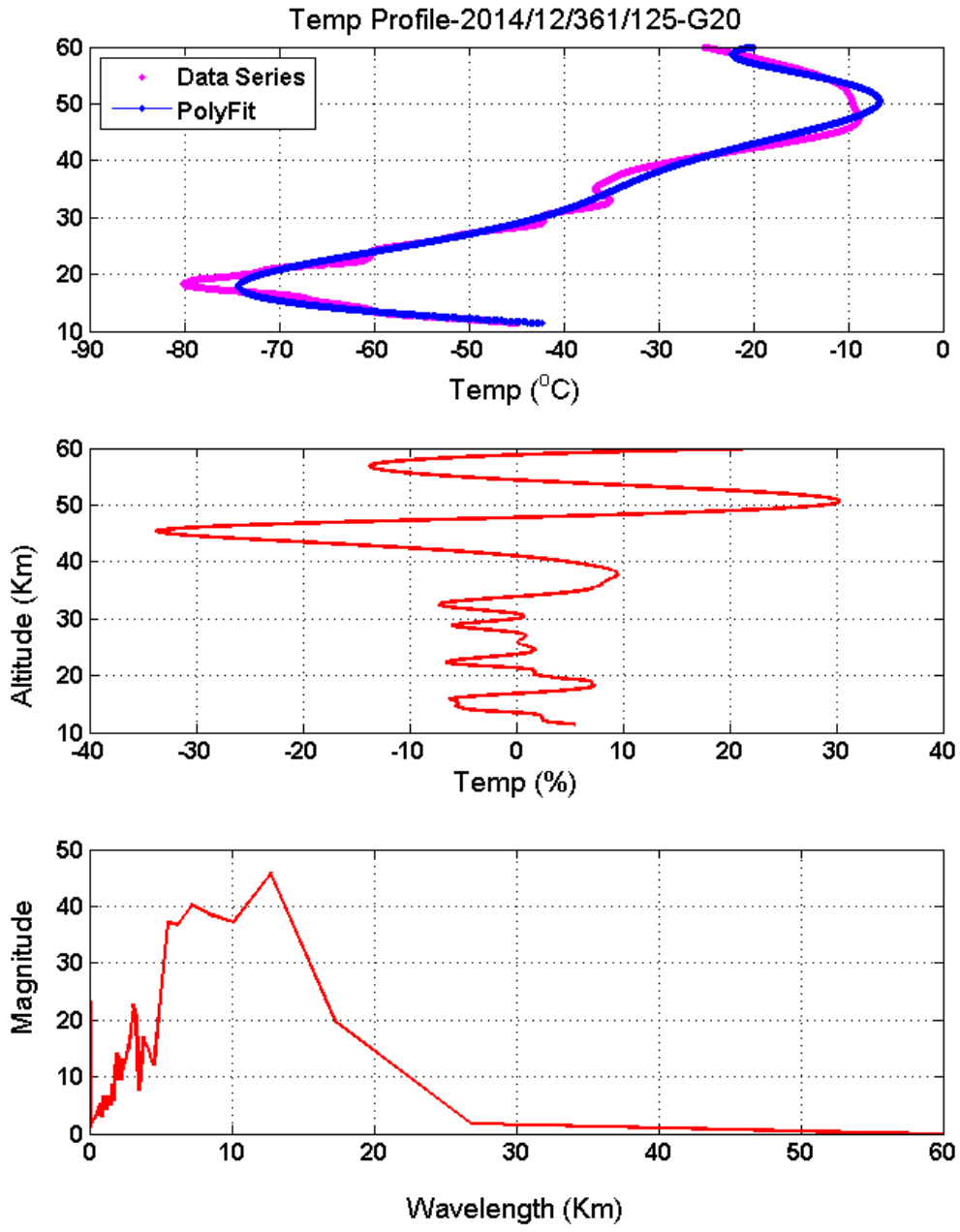

Figure 6.17 - The same as Figure 6.10 but for 27/12/2014.

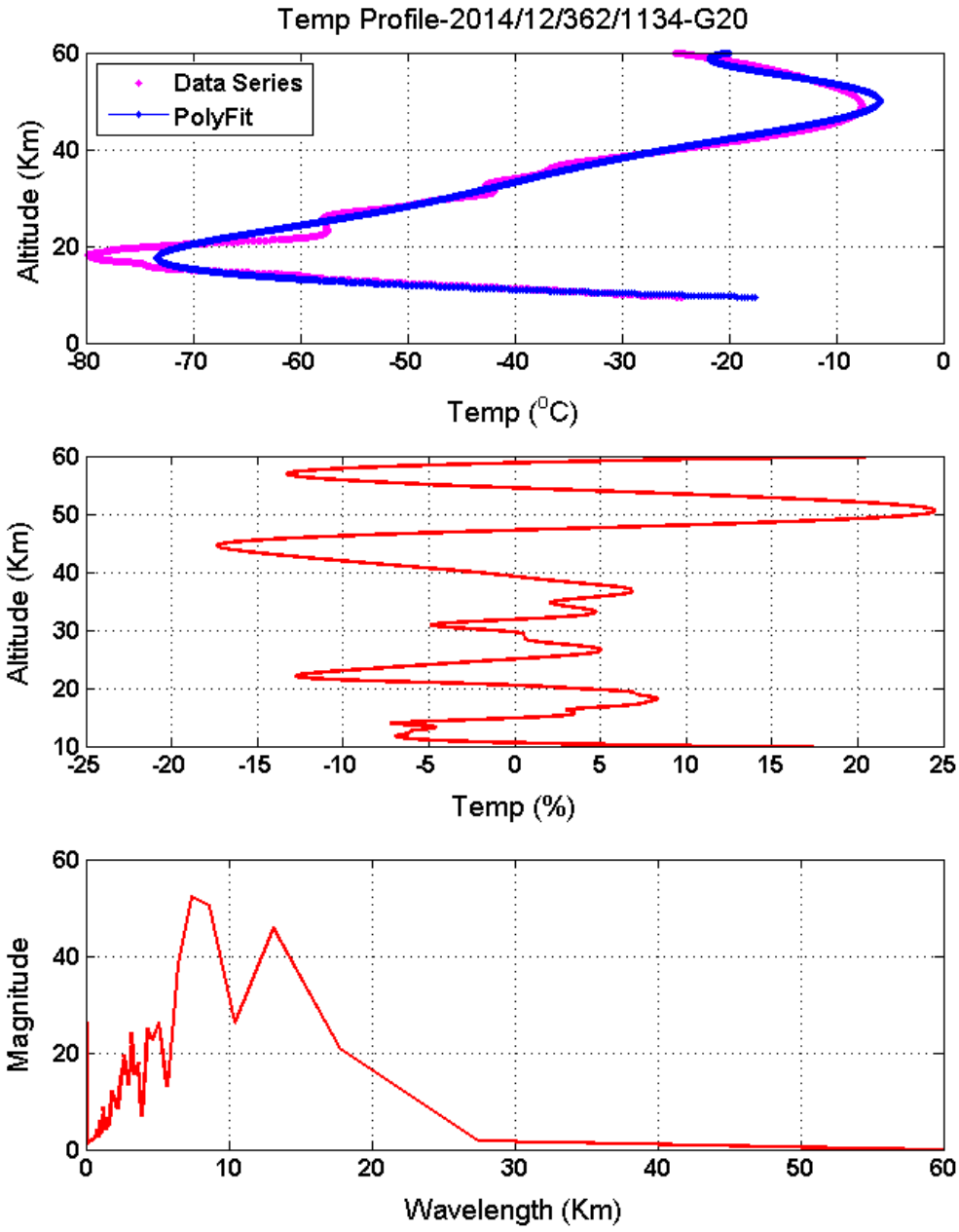

Figure 6.18 –The same as Figure 6.10 but for 28/12/2014.

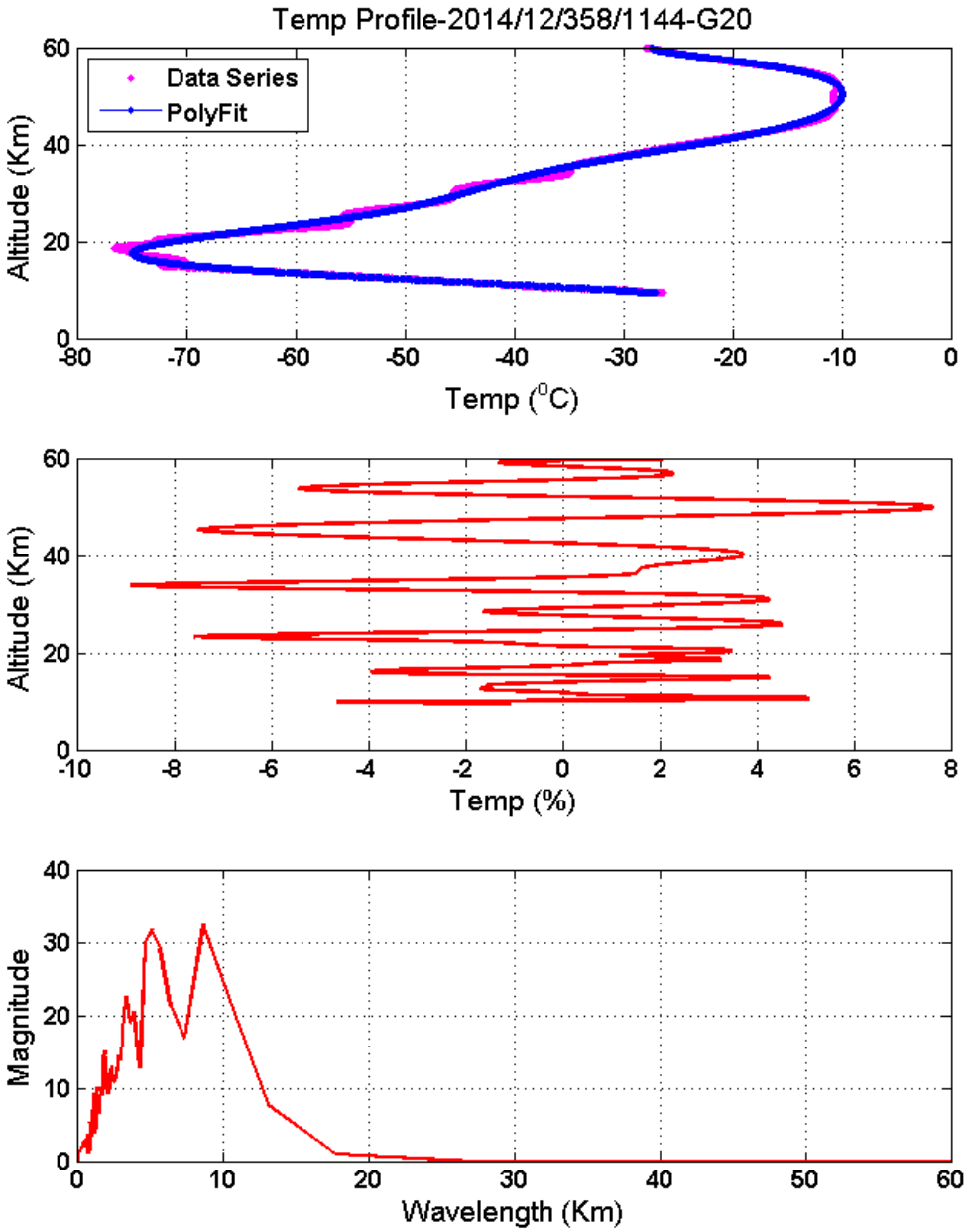

Figure 6.19 - The same as Figure 6.10 but for 25/12/2014.

7.0 SIMULATION STUDY OF AGW-MSTIDs INTERACTION DURING CONVECTIVE WEATHER USING CONVECTIVE ATMOSPHERE-IONOSPHERE COUPLING MODEL (CAI-CM)

In order to further understand the generating mechanism of AGW-MSTIDs, we present a unified approach where coupling of acoustic-gravity wave (AcGWs) and associated dynamics of the polarization electric field are considered. First, we give brief theoretical and physical descriptions of the model. Then, two numerical experiments were carried out (1) by using a strong convective forcing and (2) by using a weak convective forcing.

Kherani et al. (2016) have derived the hydrodynamic wave equation of AGWs using Navier-Stokes equations, namely the Continuity, Momentum and Energy equations in the atmosphere. By taking the time derivative of the momentum equation for the wind, and again substituting time derivatives of the density (ρ), wind perturbation ($\vec{W}'$) and pressure (p) from the Navier-Stokes equations, the wave equation for the wind perturbation $\vec{W}'$ of AGW is obtained in the following form:

$$\frac{\partial^2 \vec{W}'}{\partial t^2} = \frac{1}{\rho}\left(\gamma p \nabla \cdot \vec{W}'\right) - \frac{\nabla p}{\rho^2}\ \nabla \cdot \left(\rho \vec{W}'\right) + \frac{1}{\rho}\nabla\left(\vec{W}' \cdot \nabla\right)p$$

$$+ \partial/\partial t\left(\left[\eta \nabla^2 \vec{W}' + \left(\varsigma' + \frac{\nu}{3}\right)\nabla\left(\nabla \cdot \vec{W}'\right)\right]\right) - \partial/\partial t\left(\vec{W}' \cdot \nabla \vec{W}'\right) \qquad (7.1)$$

$$\vec{W}' = \vec{W} + \vec{W}_b$$

$$\frac{\partial \rho}{\partial t} + \nabla \cdot \left(\rho \vec{W}'\right) = 0 \qquad (7.2)$$

$$\frac{\partial \rho}{\partial t} + \left(\vec{W}' \cdot \nabla\right)p + \gamma p\ \nabla \cdot \vec{W}' = 0 \qquad (7.3)$$

Where η is the dynamic viscosity coefficient, $\vec{W}'$ is the perturbation wind, $p = R\rho T$ is the pressure, ρ, T are the atmospheric mass density and temperature. From the right hand side of equation (7.1), the first term corresponds to the acoustic wave, second and third terms correspond to the gravity wave, the fourth term with the dynamic viscosity coefficient η corresponds to the viscous dynamics and last term corresponds to the inertial force. ς represents the ratio of second viscosity coefficient to kinematic viscosity coefficient.

The ionospheric simulation is performed using set of hydromagnetic equations given below. These set of equations closely follows the governing equations described in section (1.3) of this thesis. The full explanations for the equations are found in Kherani et al. (2016) and Huba et al. (2000).

$$\frac{\partial \vec{u}_s}{\partial t} = \frac{q_s}{m_s}\left(\vec{E} + \vec{u}_s \times \vec{B}_o\right) - \nu_s \vec{u}_s + \nu_s \vec{W}', \tag{7.4}$$

$$\frac{\partial n_s}{\partial t} + \nabla \cdot \left(n_s \vec{u}_s\right) = P - L, \tag{7.5}$$

$$\nabla^2 \vec{E} - \nabla(\nabla \cdot \vec{E}) = \frac{1}{c^2}\frac{\partial^2 \vec{E}}{\partial^2 t} = 0, \tag{7.6}$$

$$\vec{J} = \tilde{\sigma} \cdot \vec{E} + \vec{J}_w; \qquad \vec{J}_w = e\left(n_i \vec{u}_i^{\,w} - n_e \vec{u}_e^{\,w}\right), \tag{7.7}$$

Where $(n_s, \vec{u}_s)$ are, respectively, the number density and velocity of plasma fluid 's' is the ions (i), electrons (e), $(q_{i,e} = Z_{i,e} - e)$, $\vec{B}_o$ is the Earth's magnetic field and $\vec{J}_w$ is the ionospheric current density caused by the AGWs, $(\vec{E}, \vec{J})$ in above equations are the electric field and net ionospheric current, ν_s is the frequency of collision between species s to neutral, $\tilde{\sigma}$ is the ionospheric conductivity

tensor and $c = \frac{1}{\sqrt{\mu_o \varepsilon_o}}$. P and L are the production and loss of ions and electrons by photoionization and chemical reactions. The production term 'P' in (7.5) is derived from SAMI2 model. The chemical loss term, 'L', in equation (7.5) is retained through effective recombination rate as taken by Kherani et al (2016). In addition to wave equation (7.6), $\vec{E}$ also satisfies the charge neutrality condition given by the following equation (Kherani et al., 2012).

$$\nabla \cdot \vec{J} = 0 \ or \ \nabla \cdot \left(\tilde{\sigma} \cdot \vec{E} + \vec{J}_w\right) = 0 \Rightarrow \ \nabla \cdot \vec{E} = -\tilde{\sigma}^{-1}\left(\nabla \tilde{\sigma} \cdot \vec{E} + \nabla \cdot \vec{J}_w\right) \tag{7.8}$$

At t = 0, ambient atmosphere and ionosphere (P_o, ρ_o, n_o, v_o, T) are obtained from SAMI2 model (Huba et al., 2000). The Earth's magnetic field, $\vec{B}_o$, is obtained by using IGRF model within the SAMI2 model.

Equations (7.1 to 7.8) are solved numerically using finite-difference method in three dimension simulation domain in spherical polar coordinate that consists of altitude (r), latitude (θ) and longitude (ϕ). The implicit Crank-Nicholson scheme is employed to perform the time integration leading to a matrix equation that is subsequently solved by the Successive-Over-Relaxation method. The magnetic dipole coordinate system (*p, q, ϕ*) is adopted where *p, q, ϕ* represent the coordinates outward normal to the Earth's magnetic field, northward directed parallel to the Earth's magnetic field and azimuth angle (+ve towards west) respectively. The N-S and E-W boundaries of simulation domain are 45°S −5° S and 75°−35°W which covers the region of interest. The lower boundary for the atmosphere and ionosphere are chosen to be the 10 km and 160 km respectively. The upper boundary is chosen to be 600 km for both the atmosphere and ionosphere.

The flow chart for the Convection Atmospheric-Inonspheric Coupling Model is shown below. The Atmospheric part of the model is first initiated using the

hydrodynamic equations as given in equations 7.1 to 7.3.In the presence of convective forcing at tropospheric height a primary gravity wave is generated which propagates upward. With the given dissipation terms, a secondary gravity is excited around 120 to 250 km altitude. Then the coupling of atmosphere with ionosphere is conducted next using equation (7.4) and by solving the hydromagnetic equations (7.5) to (7.8) the electric field is calculated to give a divergent free current. Finally the MSTIDs are generated as TEC perturbation and the code is updated again for the next time.

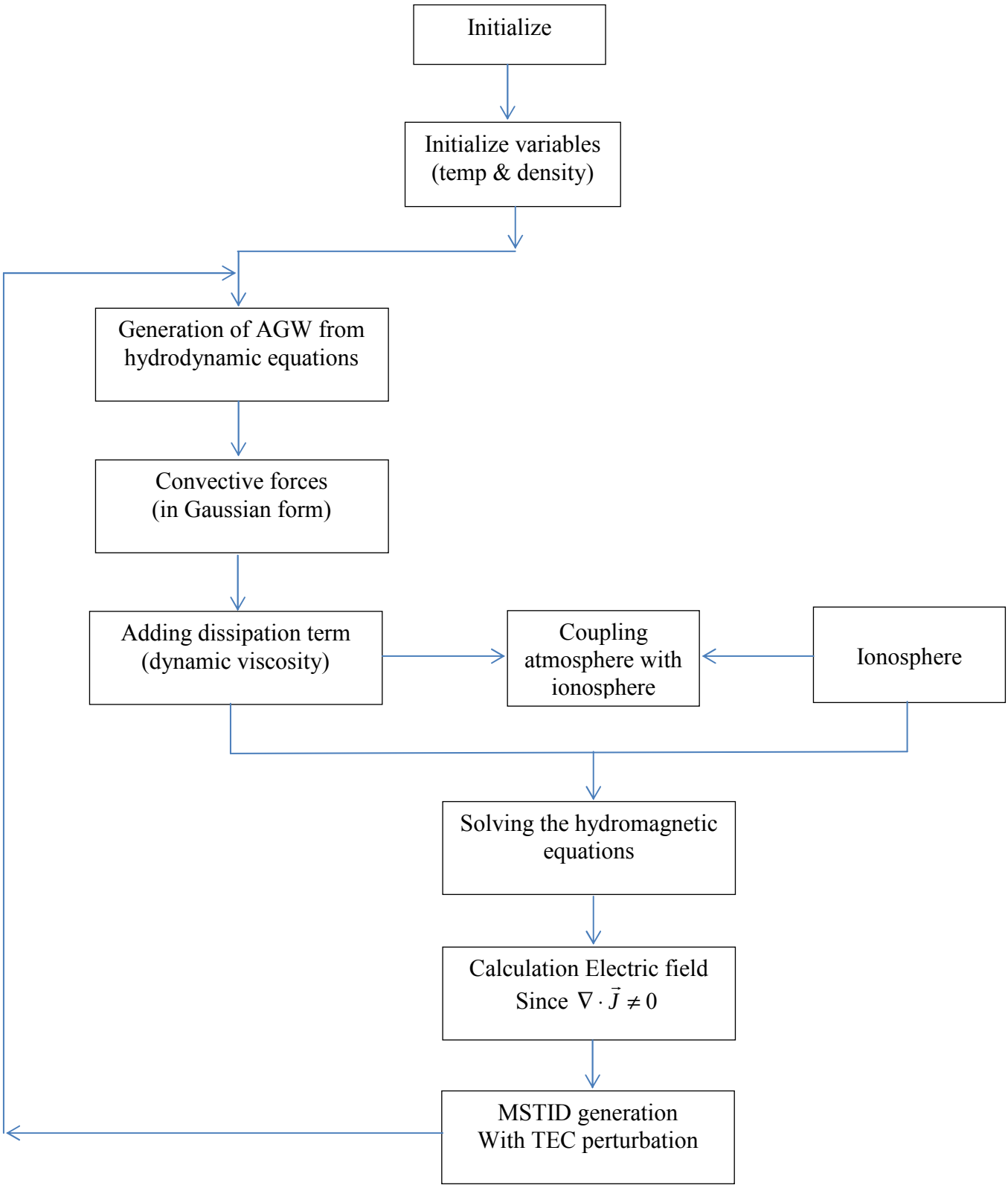

Figure 7.1 - Dynamic flow chart of the Convection Atmosphere-Ionosphere Coupling Model

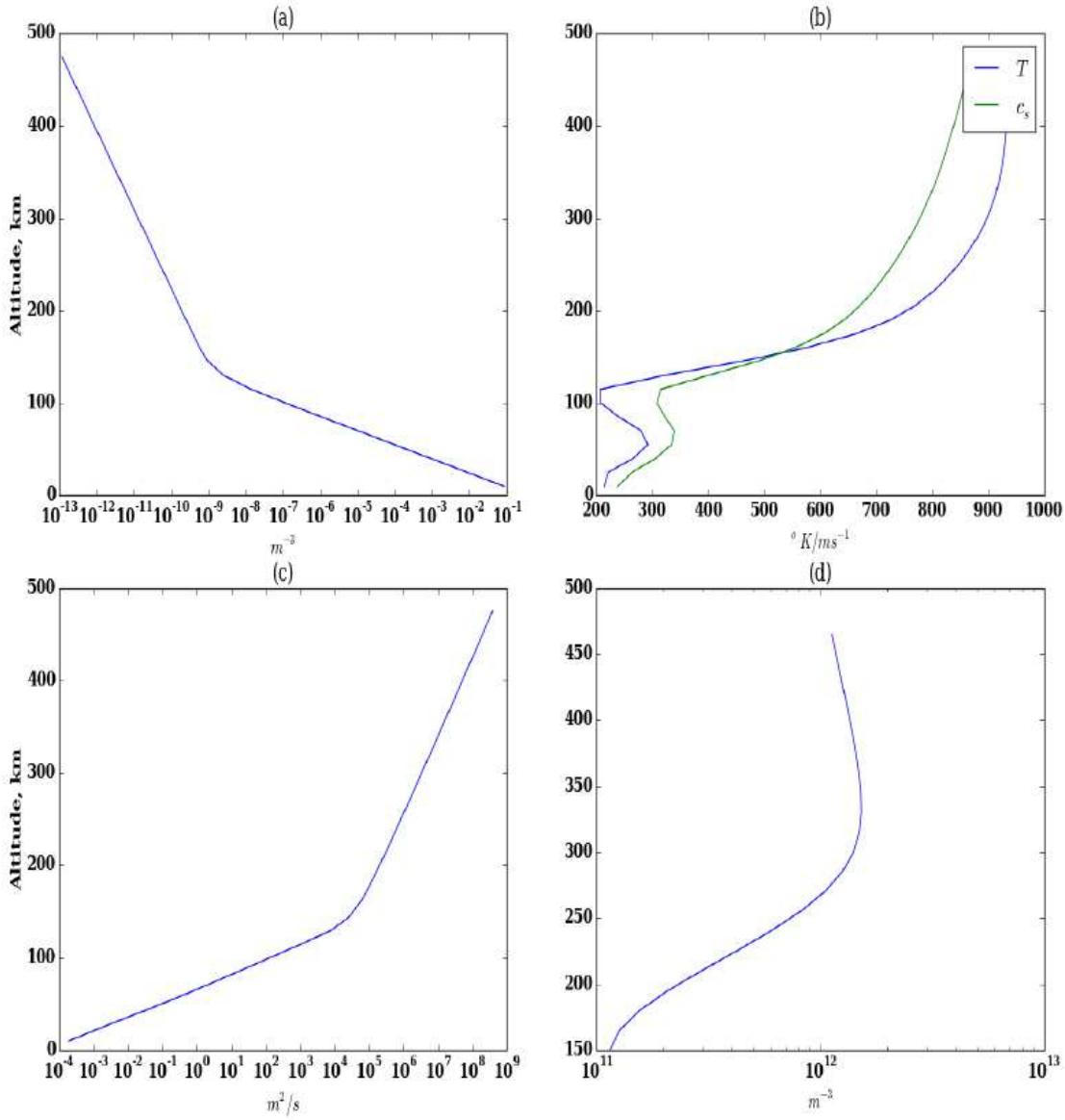

Figure 7.2 - Ambient atmospheric and ionospheric conditions: (a-d) Altitude profiles of Atmospheric density (ρ_o), Temperature/Sound speed (T_o / c_s), Dynamic viscosity ($\eta = \mu / \rho_o$) and Ionospheric density (n_o). To the first order, atmosphere and ionosphere are considered to be horizontally stratified at the simulation beginning time t = 0.

In Figure 7.2, from (a) to (d), the atmospheric mass density (ρ), acoustic speed ($\sqrt{\gamma p / \rho}$) kinematic viscosity (η) and ionospheric number density (n_o) are shown. The ambient electric field is considered to be zero.

In order to understand the MSTIDs dynamics as observed and presented in the previous chapters, we focus on comparative study of MSTIDs observed on 05 (D1) and 07 (D2) December 2011 as represented by Figures 6.7(a) and 6.7(d) in chapter 6 of this thesis. These two days represent the extreme conditions of convective and MSTIDs dynamics. For example, on D1 (D2) the convective activity is strong (weak), manifested by large (small) convective cloud. The MSTIDs observed on these two days reveal positive correlation with the convective activity such that on D1 (D2), they have distinct (not so obvious) propagation characteristics on keograms.

The convective forcing is considered to be of Gaussian form as follows (Zettergren and Snively, 2015):

$$W_r = (r = 0, \theta, \varphi, t) \equiv W_F = 10^{-3} e^{-(t-t_o)^2/\infty_t^2} e^{-(\theta-\theta_o)^2/\infty_\theta^2} e^{-(\varphi-\varphi_o)^2/\infty_\varphi^2} m/s, \quad (7.9)$$

where (t_o = 4000 seconds, θ_o = −22.5°, φ_o = −57.5º) are the coordinates of maxima of W_r and ($\infty_t, \infty_\theta, \infty_\varphi$) are the half-maximum-full-width of Gaussians in respective coordinates. In the present study, ∞_t =2000 seconds is considered, based on common convective forcing characteristics. Based on ($\infty_\theta = \infty_\varphi$), two case studies, D1 and D2, are classified. In D1 (D2), ∞_θ is considered to be 2^o (1^o) respectively. In Figure 7.3, 3D view of the convective forcing is shown for D1. We may note that the effective size of convective forcing is $\sim 10^o$ which is noted in observation on 05 December 2011 as presented in Figures 6.7a. Accordingly, for D2, the size is $\sim 5^o$ as also consistent with the observation on 07 December 2011. We refer simulation exercises of D1 and D2 as numerical experiment NE1 and NE2.

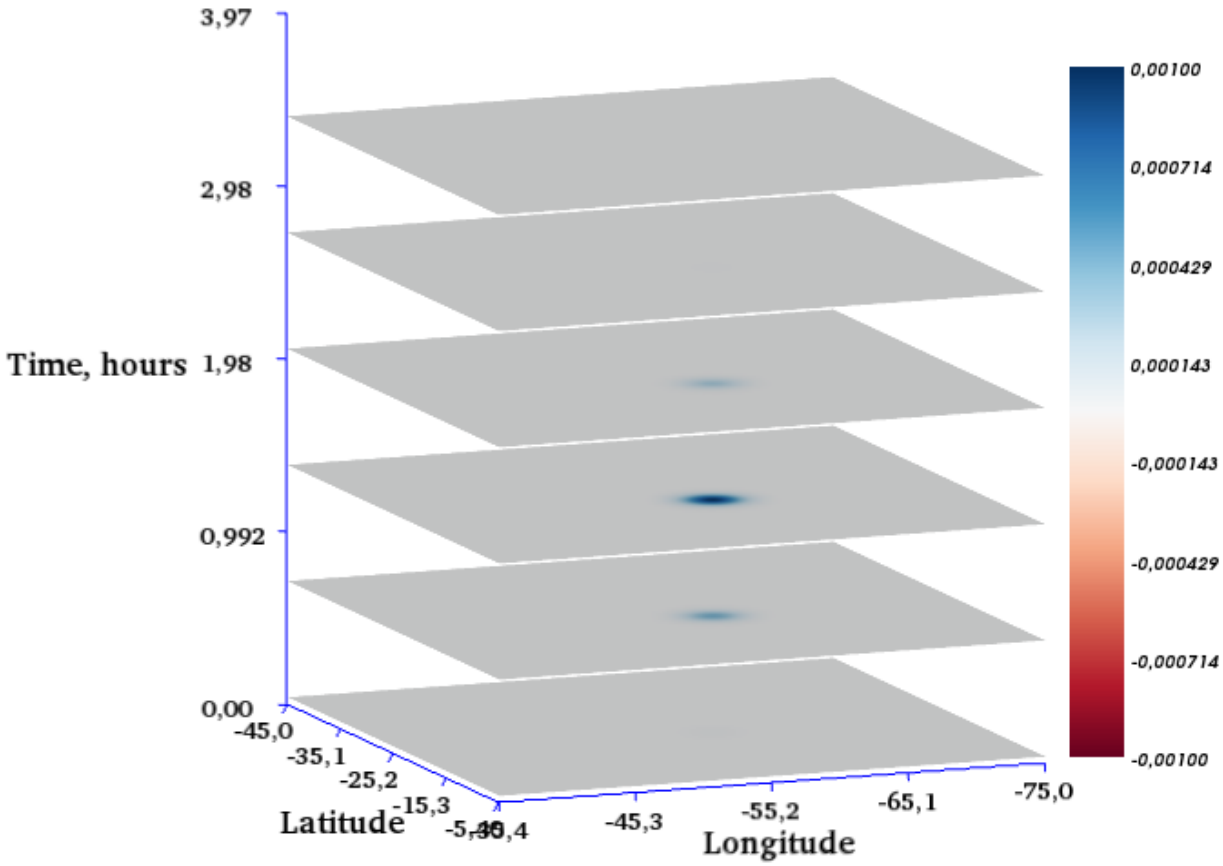

Figure 7.3 - Convective Forcing characteristics: 3D view demonstrates the forcing, in the form of uplift i.e., W_r at the lower boundary of simulation volume which is at 10 km height. It is of Gaussian type in time (t), longitude (φ) and latitude (θ). The color bar unit is in m/s.

At the lower boundary i.e., at 10 km altitude, the outward normal component W_r of the wind $\vec{W}$ is continuous and equals to W_F for all time. The lower boundary condition $W_r = W_F$ at all time acts as the driving source for the excitation of AGWs. At the subsequent time, other wind components W_θ, W_φ in entire simulation domain and W_r in entire simulation domain except at the lower

boundary are self-consistently determined from the equation (7.1). The presence of AGWs modifies the atmosphere and ionosphere which in turn alters the characteristics of AGWs itself. This cause-effect mechanism continues for next 3 hours which is the time chosen to stop the simulation.

7.1 Simulation results (Numerical Experiment 1)

Recall that our first and second simulation exercises as mentioned earlier are D1 and D2 and are referred to as numerical experiment 1 and 2 (i.e. NE1 and NE2). In Figures 7.4 – 7.5, we present the simulation results of AGWs for D1. In Figure 7.4, the three dimensional distribution of vertical wind amplitude (W_r) of AGWs at few selected times are shown. In Figure 7.5, snapshots of the horizontal distribution of W_r at the altitude of 200 km altitude is shown.

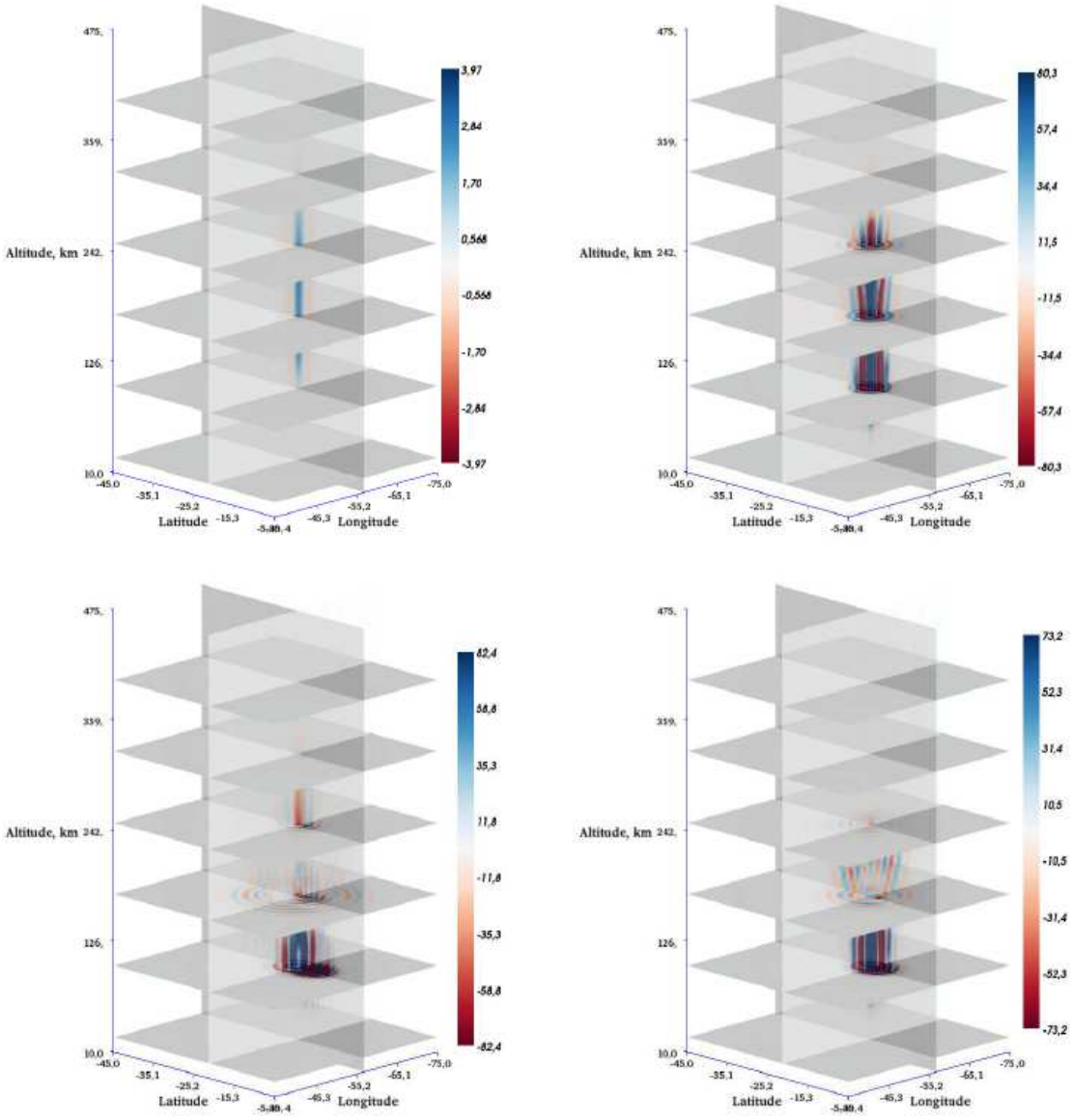

Figure 7.4 - AGW simulation: 3D volume snapshots of amplitude (W_r) of AGWs at four selected times t=2000, 4000, 6000, 8000 seconds organized in clockwise direction.

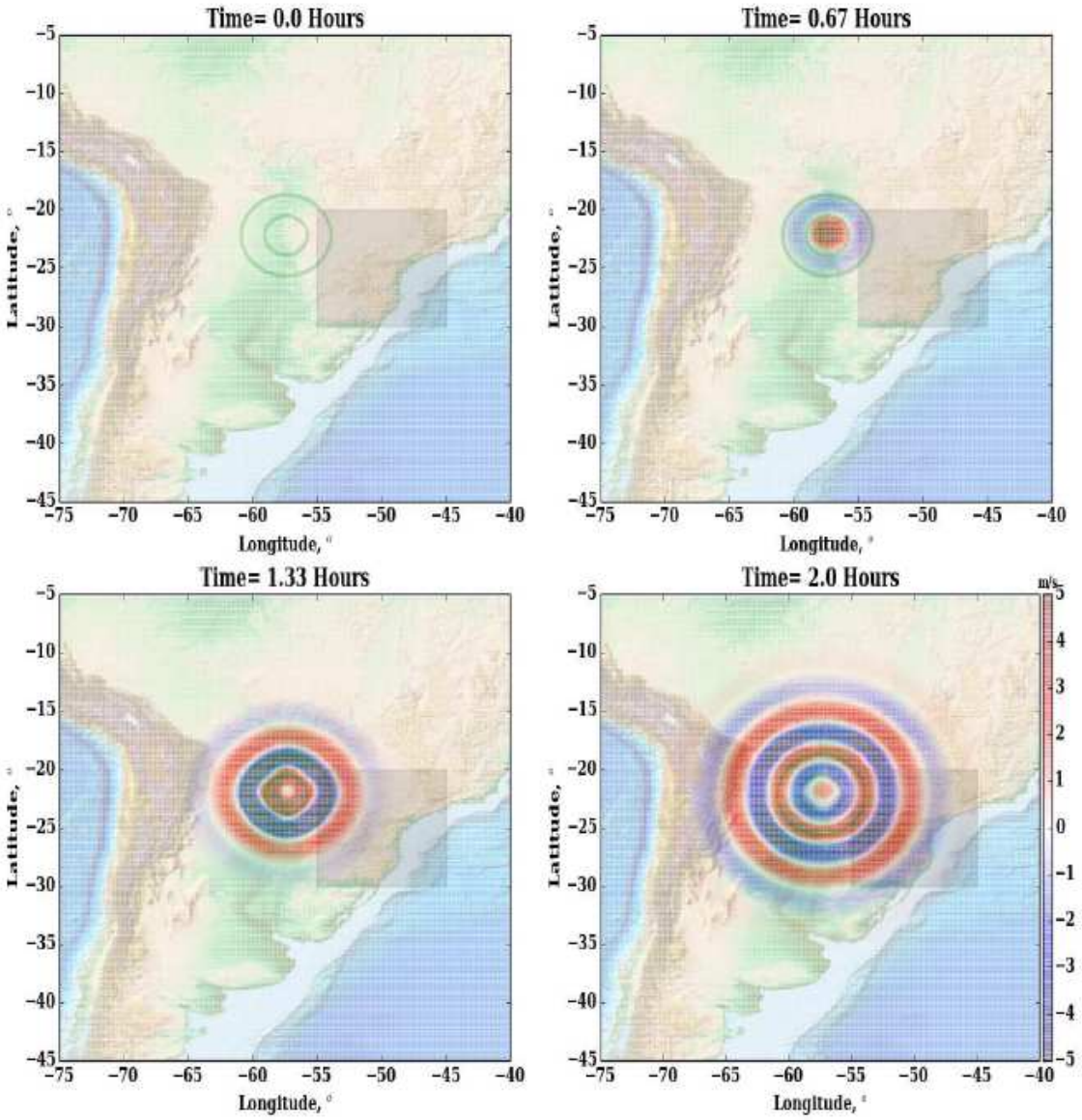

Figure 7.5 - AGW simulation: 2D horizontal snapshots of amplitude (W_r) of AGWs at four selected times t = 2000, 4000, 6000 , 8000 seconds and at altitude of 200 km altitude. The green contours represent the convective forcing at 10 km altitude. The shaded rectangle represents the GNSS receiver locations used in the observations.

We note in Figure 7.4 – 7.5 that the forcing at 10 km altitude that is, the disturbance introduced at 10 km altitude propagates in space and time such that its amplitude and horizontal coverage increases with altitude up to 300 km and then decreases. This is because in the thermosphere, the horizontal coverage is much wider (∼30°) than the forcing size (∼10°) itself which is a result of viscous dissipation and secondary generation of AGWs in the thermosphere (this process that generates the secondary AGWs is refers as the thermospheric body force as discussed in the previous chapters). The horizontal propagation is accomplished in the form of concentric circular wavefronts with wavelength of $\sim 3^\circ - 5^\circ$, as noted in Figure 7.5 that progressively propagate outward from the convective forcing.

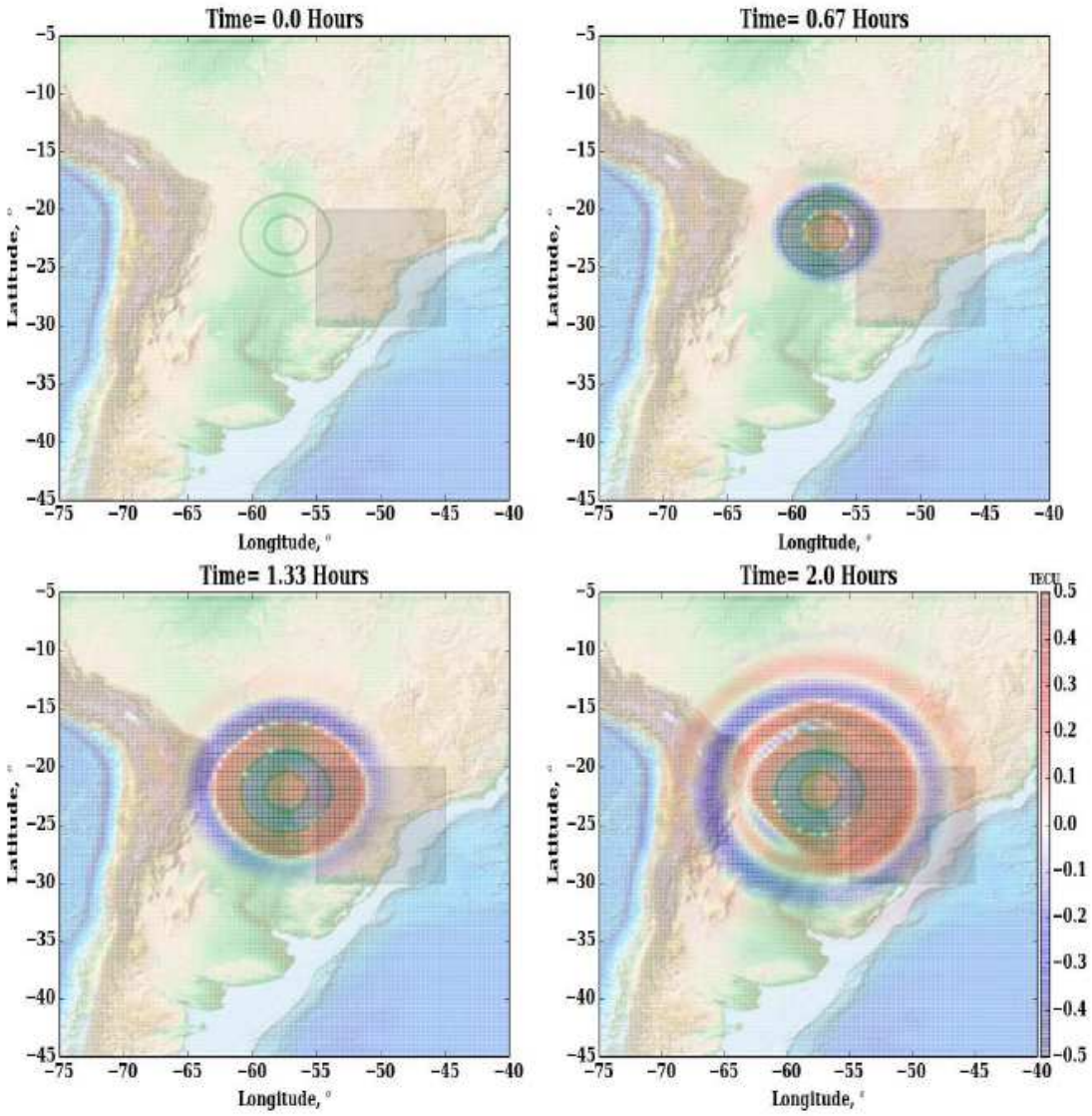

Figure 7.6 - TEC simulation: 2D snapshots of ΔTEC at four selected times t=2000, 4000, 6000, 8000 seconds.

In Figure 7.6, the simulation results for ΔTEC is presented. Where ΔTEC = TEC(t) − TEC_{amb}(t) where (TEC(t) and TEC_{amb}(t)) are derived from ionospheric density by solving the continuity equation with and without including AGWs. The simulated TEC is obtained by integrating the density along the path perpendicular to the field lines. In this figure, it is possible to observe snapshots of ΔTEC distribution in form of radial propagation. Interestingly, TEC disturbance in Figure 7.6 also reveals similar evolution and propagation characteristics as the AGWs in Figure 7.5. We may note that W_r of ~50 m/s and

ΔTEC of ~0.5 TECU is excited, as a result of convective forcing of $\sim 10^{-3}$ m/s.In Figure 7.7, latitude and longitude keograms of W_r and ΔTEC just as observed in the experimental study of the previous chapters are shown.

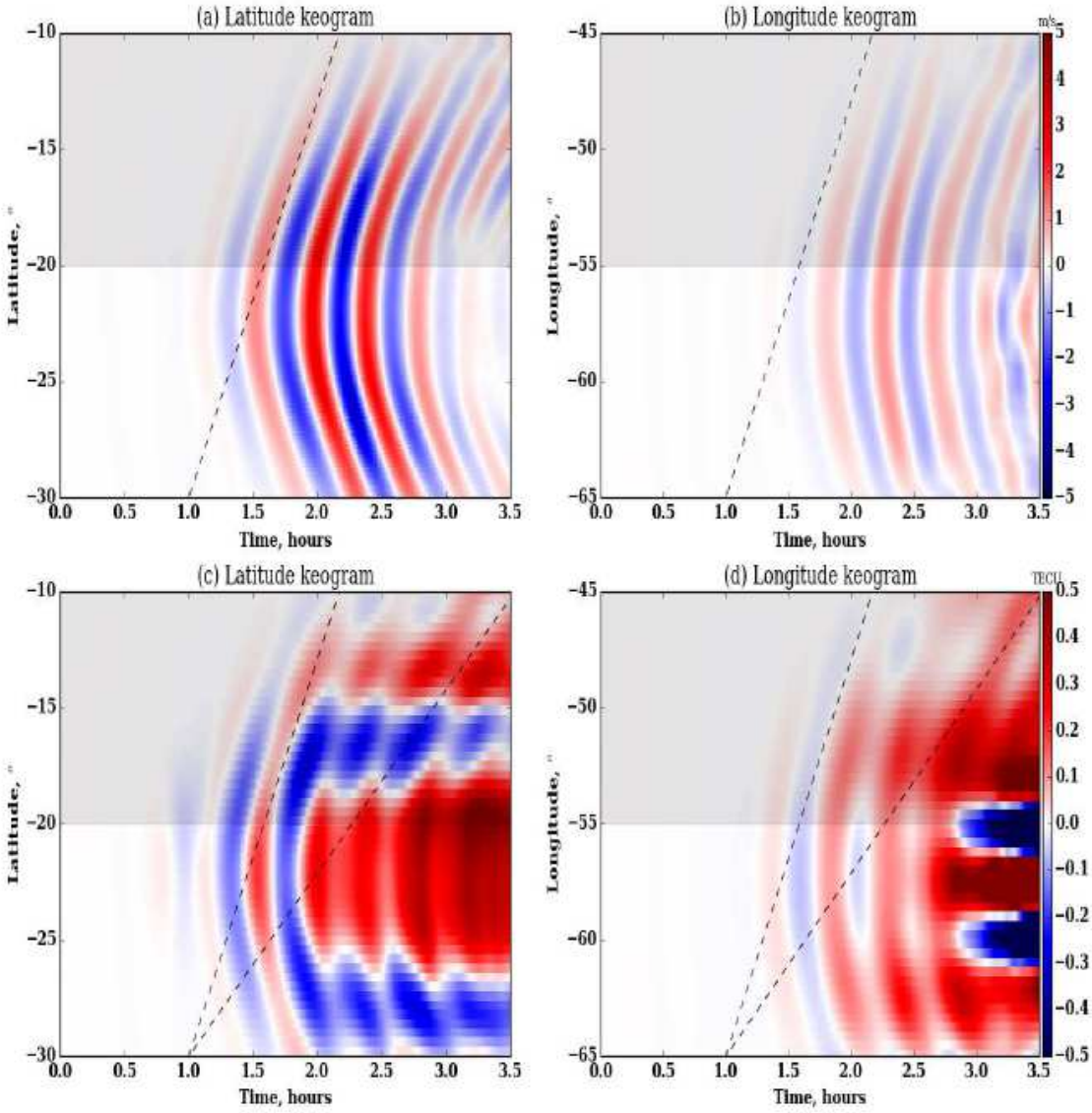

Figure 7.7 - Keograms: Latitude keograms at fixed longitude (φ = −50.4°) and longitude keograms at fixed latitude (θ = −12.4°) for W_r in the upper panel and for ΔTEC in the lower panel. The dashed lines represent the slopes of 650 m/s and 300 m/s.

The keogram in Figure 7.7 reveals the equatorward-eastward propagation of ΔTEC, similar to the observed propagation of MSTIDs in the previous chapters. We also note the period of wavefront to be ~30 minutes which is another aspect similar to the observed results. Both wavelength of ~3° − 6° and period of ~30 minutes classify the simulated TEC disturbances as MSTIDs. In Figure 7.7, it is also possible to clearly identify the acoustic wavefront propagating horizontally with ~650 m/s as evident from the dashed line which has its slope equals to 650 m/s. In addition, we also identify the slower propagating gravity wavefront after 2.5 hours and their propagation speed is ~250 m/s. This wavefront is observed in the observation presented in the previous chapters. Our observation results are likely to miss the acoustic wavefront owing to the slower sampling rate >30 seconds. For this reason, the observed keogram reveals only the gravity wavefronts.

Another important difference we note between observed and simulated latitude keograms is the difference in the location of equatorward propagating wavefront. In contrast to their apparent observed location between −25° − -20°, the simulated location covers between −20° − −15°. It should be noted that the observed keogram is plotted with respect to the receiver location. However, the observed ΔTEC corresponds to the IPP locations which may be significantly different from the receiver location. In the present case, these IPPs seems to cover the northward of the area covered by the receiver and therefore in this case, the observed and simulated locations may not differ considerably. The differences noted between observed and simulated ΔTEC may be caused by various reasons, notable among them are the differences in the ambient conditions, convective forcing and the procedure of estimating ΔTEC

7.2 Simulation results (Numerical Experiment 2)

The simulation results for NE2 are presented in Figures 7.8 – 7.10 in same format as Figures 7.5 – 7.7 respectively. We note the excitation of AGWs and subsequent development of ΔTEC disturbances in the form of concentric

circular wavefronts, similar to NE1. However, in NE2, the wavefronts are weak and the horizontal coverage is limited in comparison to NE1. This difference arises from the weak convective forcing in NE2 that launches shorter horizontal wavelengths.

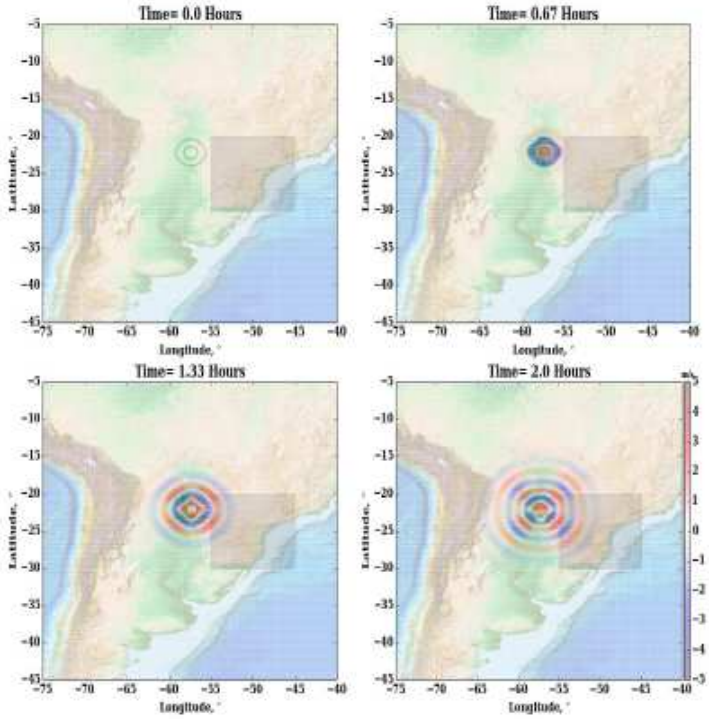

Figure 7.8 - NE2: same format as Figure 7.5.

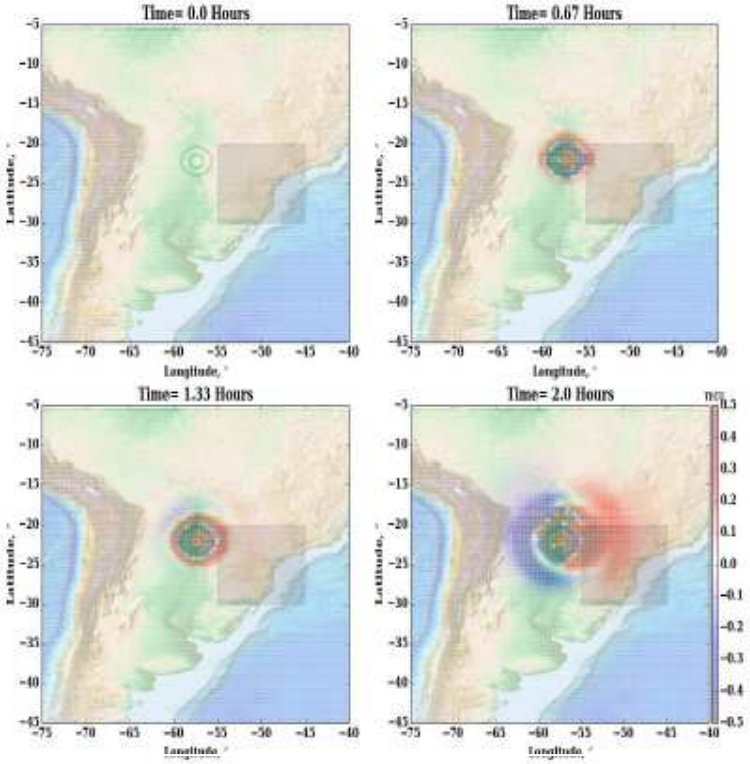

Figure 7.9 - NE2: same format as Figure 7.6

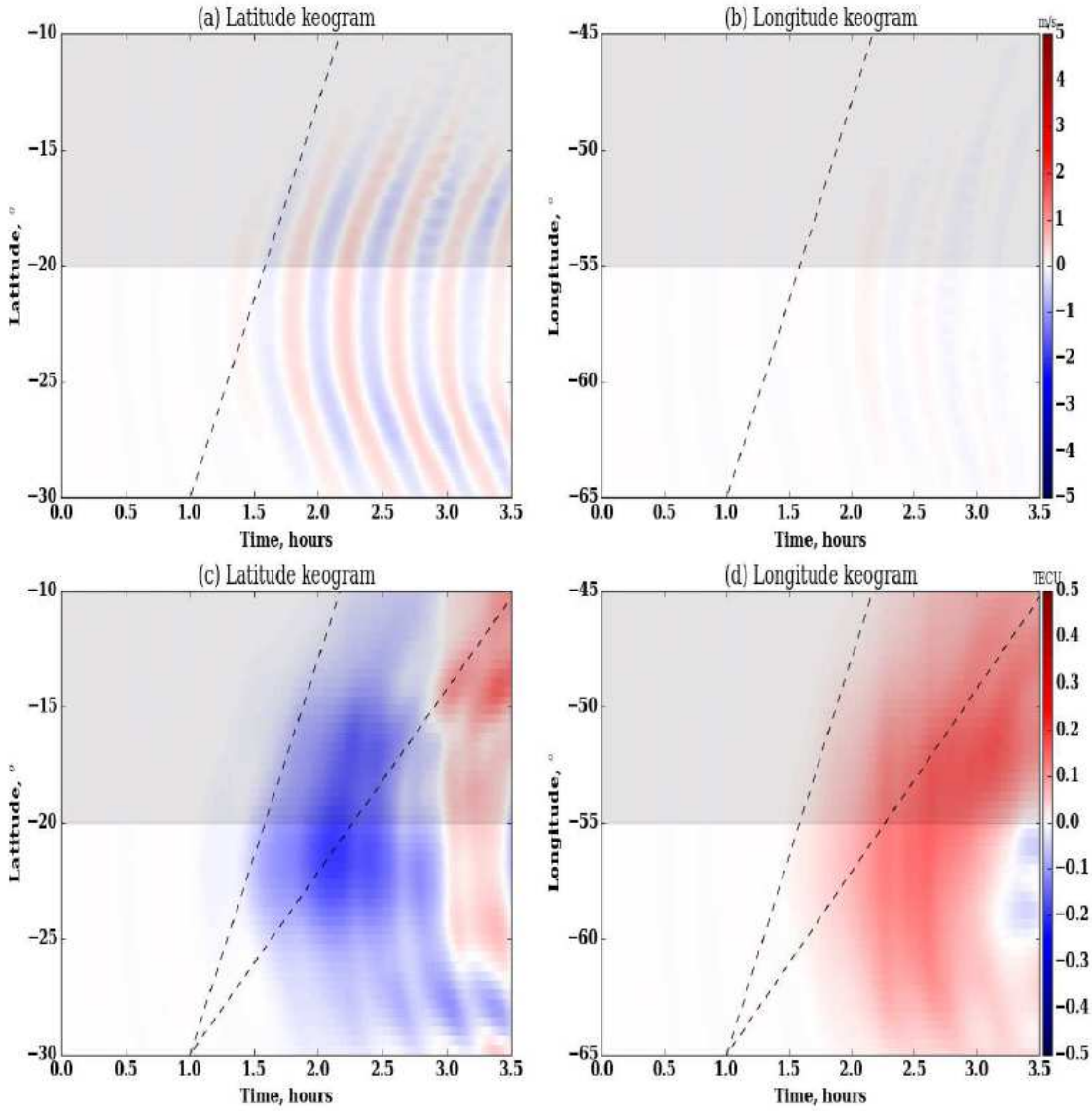

Figure 7.10 - NE2: same format as Figure 7.7

As mentioned earlier the simulated MSTIDs are located more towards equator than in the observation results. This difference is possibly due to the fact that IPPs of the observations are located more towards equator. At the same time, it is possible to bring these MSTIDs within the similar latitude region as the observation by relocating the convective forcing to more towards southward. The keograms and the circular propagation from this numerical experiment which we refer as NE1_2 are shown in Figure 7.11 and Figure 7.12 in which the convective forcing is located in 30°S – 25°S, in contrast to its location in 25°S –

20°S in NE1. We note that the MSTIDs are now located in similar region as the observation. Therefore for future research, it could be recommended to use the IPP position of TEC observations rather than using the receiver positions.

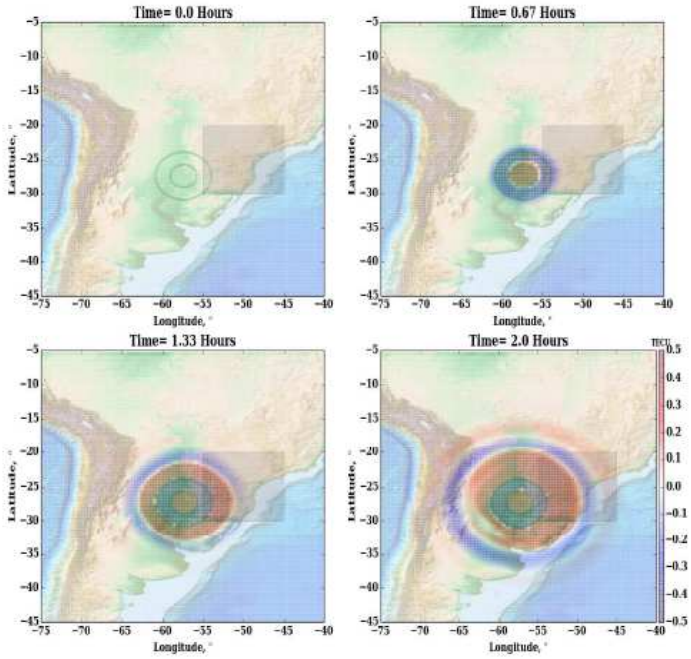

Figure 7.11. NE1_2 results: In same format as Figure 5.

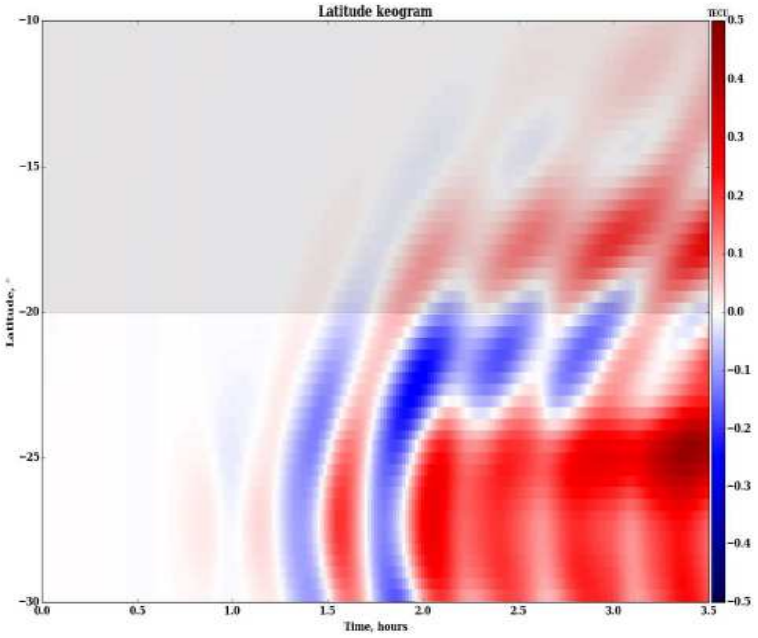

Figure 7.12. NE1_2 results: In same format as Figure 6.

7.3 Comparison between observational and simulation results

Table 7.1. The characteristics differences between the observed and the simulated MSTIDs.

Properties	**Observed MSTIDs**	**Simulated MSTIDs**
Wavelength	255 - 480 km	300 - 600 km
Period	20 - 55 min	$\leq$ 30 min
Velocity	122 - 260 m/s	250 - 600 m/s
Direction	Northeastward - SH	Northeastward - SH
Geomag. activity	Quiet	Quiet
Source	GW excited by convective weather	AcGW and AGW excited by convective weather in Gaussian form.

8.0 SAMI 3 NUMERICAL MODEL

In this chapter, we use the SAMI3 numerical model as a self-consistent model to reproduce our observed MSTIDs in the previous chapters. The description of the model is first presented, next, the physical developments of MSTIDs is described. Followed by how SAMI3 programming is implemented in parallel programming. The simulation results are then presented, using two cases: (1) by applying density perturbation and (2) by applying perturbation in the electrostatic potential.

The previous simulations work (e.g. DULY et al., 2014, HUBA et al., 2015) have established that SAMI3 numerical model can be used to generate MSTIDs and basic descriptions of nighttime MSTIDs from experimental observations (e.g. KOTAKE et al., 2006, OGAWA et al., 2009) agree well with the synthetic observations obtained from the model (e.g. DULY et al., 2014, HUBA et al., 2015). SAMI3 numerical model has its origins in a two-dimensional model named SAMI2 (Huba et al., 2008). SAMI2 was developed at the Naval Research Laboratory (NRL) as a tool to study the ionosphere. The SAMI2 model solves the ion-conductivity and momentum equations for seven ion species (H^+, He^+, N^+, O^+, N_2^+, NO^+, and O_2^+) in a longitudinal “slice" of the ionosphere for altitudes ranging from approximately 100 km to over 1000 km. SAMI3 is similar to SAMI2, except it includes grid spacing in the longitudinal direction and a potential solver, thus, modeling the ionosphere on a global scale. In the original SAMI2 code, the electric field is calculated from a climatological (e.g., FEJER , 1993), analytical, or data-driven model. However, SAMI3 solves for the potential self-consistently within the model. Also, the equations were updated to solve the ion and momentum equations in three dimensions. There is also a version of the code that models a “wedge" of the ionosphere and is commonly termed “SAMI3/ESF" for its primary use in Equatorial Spread F (ESF) studies (HUBA et al., 2015). For this study, we use the wedge model of SAMI3 for the numerical simulations as we are primarily interested in MSTIDs developing within a region spanning a few degrees in

longitude. Moreso, the wedge model of SAMI3 provides a large spatial domain extending to mid-latitudes in both hemispheres, enabling an investigation of MSTIDs developing in the conjugate hemisphere.

Furthermore, the electrostatic potential calculation in the model allows for conjugate effects of MSTIDs studies. Conjugate observations of MSTIDs have shown that the structures are mirrored along the geomagnetic equator and develop in conjugate hemispheres (OTSUKA, 2004). In this work, the conjugacy effect is numerically studied with SAMI3's grid covering both the Northern and Southern hemispheres. Along with the sophisticated equation solvers, the large 3D spatial domain of SAMI3 enables us to extend the previous numerical work to explore the development of MSTIDs grounded on fundamental, physics-based equations.

8.1 Coordinate System

In order to model MSTID in SAMI3, a coordinate system that provides an advantage for solving equations easily, and one that leads to a concise description of the instability were used. SAMI3 uses a dipole coordinate system for its grid. This allows equations to be broken down into calculations for both parallel and perpendicular to magnetic field ($\vec{B}$). Figure 8.1 is used to describe the coordinate system where q is along the magnetic field line direction. Magnetic east is described by ϕ while p following the right-hand rule, points radially outward from the magnetic field lines. In the southern hemisphere, this is commonly referred to as perpendicular and south because it is perpendicular to the field line and also points to the southern direction. Figure 8.1 gives an example of the coordinate system that is based on the direction of the geomagnetic field line. The SAMI3 model was used to develop realistic magnetic field lines for this plot and displays apex altitudes between approximately 100 and 3,000 km. The right-hand side of Figure 8.1 is a zoom view of the blue box region from the left-hand plot and highlights the coordinate system, where it is possible to see that q points along the magnetic field line,

and each (p, ϕ) pair describes a particular magnetic field line. The physical explanations behind the development and formation MSTIDs as adopted in SAMI3 are discussed next section.

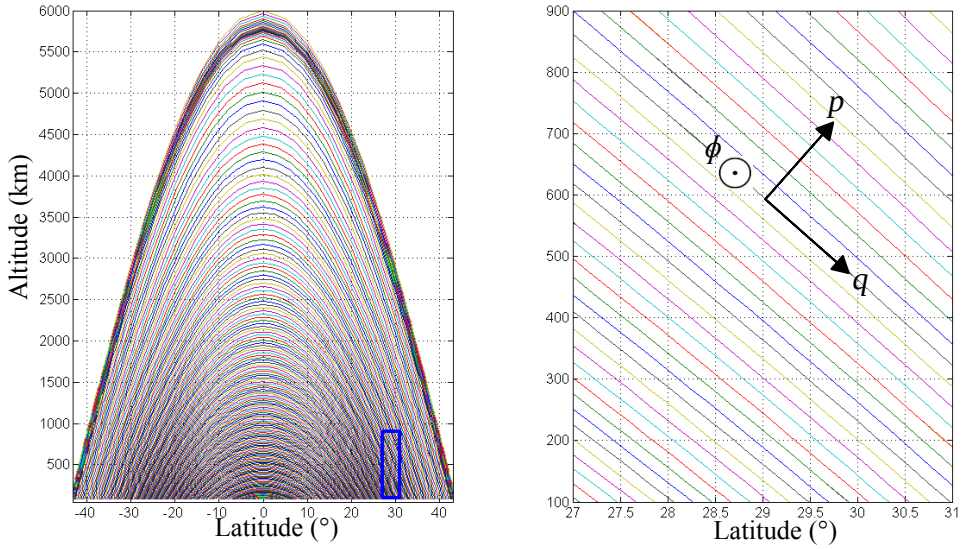

Figure 8.1 - Magnetic field lines as function of eccentric latitude and altitude (left). A zoomed-in version (right) shows that q is along the field line direction, and p represents a magnetic field line.

8.2 Physical Developments of MSTIDs

There are three principal ways by which instability leading to MSTIDs can be described: (1) by using the Perkins instability equations, (2) by using the basic governing equations as discussed in section 1.3, and (3) by using the physical development arguments discussed below.

MSTIDs are plasma instabilities that are characterized by raise and lowered bands of electron density with respect to altitude and have wavefronts at an angle to the magnetic field line. The instabilities occur when there is an unstable equilibrium due to the presence of a N-S component of the electric field or zonal component of the neutral wind. This phenomenon would cause ionospheric current to be non-divergent, hence there is a need to maintain divergent free

current to maintain the ionosphere. Therefore polarization $\vec{E}\times\vec{B}$ drifts are developed to transport plasma and to keep the $\nabla\cdot\vec{J}=0$. To explain this behavior we used the Figure 8.2 below.

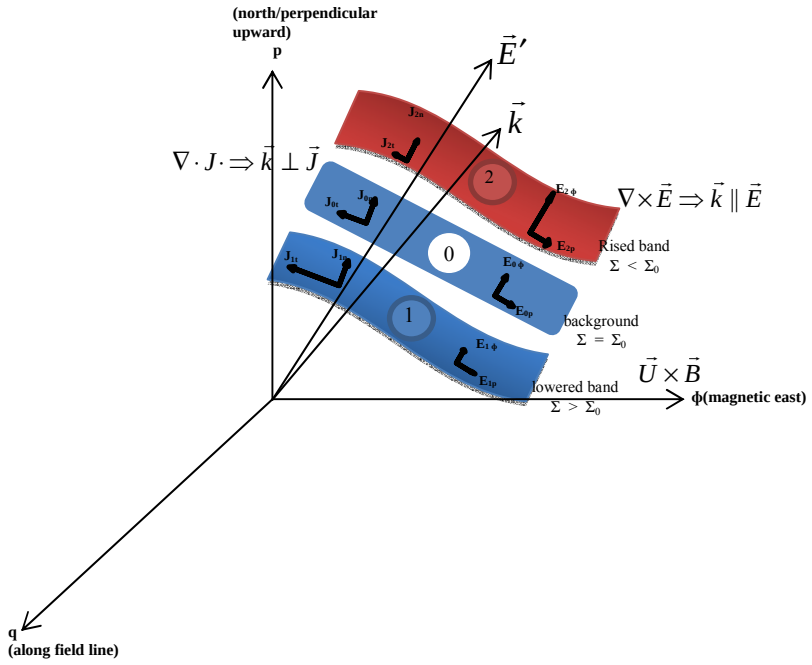

Figure 8.2 - The development of MSTIDs with normal (n) and tangential (t) current densities (upper left) and the magnetic east (ϕ) and perpendicular and north (p) electric field (right corner). The background region is displayed at the middle plate, the perturbed lowered region is displayed at the bottom plate and the perturbed raised plate is displayed at the upper plate.

Using the coordinate system explained in Figure 8.1, the configuration shows that there exists an effective electric field $\vec{E}'$ represented by the upper-right arrow in the p, ϕ plane. The $\vec{E}'$ contain the background electric field ($\vec{E}_0$) and the $\vec{E}\times\vec{B}$ term (i.e. $\vec{E}'=\vec{E}_0+\vec{U}\times\vec{B}$). The $\vec{U}\times\vec{B}$ is assumed to be dominant over the $\vec{E}_0$. The initial perturbation is given by the wave vector represented by ($\vec{k}$)

in the lower-right arrow in the *p, ϕ* plane. Region 0 is the equilibrium/unperturbated area which consists of background of the integrated Pederson conductivity. Under this set-up, $\vec{E}\times\vec{B}$ drift would propagate the MSTIDs structure in the southeast direction in the northern hemisphere (and northeastward in the southern hemisphere during daytime) creating a lower (region 1) and the raised (region 2) with altitude.

This Figure 8.2 also shows both current density at upper-right and electric field at bottom-right on each slab. The current densities normal to $\vec{k}$ according to $\nabla\cdot J\cdot\Rightarrow\vec{k}\perp\vec{J}$ are equivalent (i.e. J_{0n}=J_{1n}=J_{2n}). Using the relation $\vec{J}=\Sigma\vec{E}$ and the requirement that tangential electric field must be equal, then J_{1t}>J_{0t}>J_{2t}. on the other hand, in the bottom-right of each slab of Figure 8.2 and display the p and ϕ components. The electric field parallel to the $\vec{k}$ according to $\nabla\times\vec{E}\Rightarrow\vec{k}\parallel\vec{E}$ will be reduced (region 1) and increased (region 2). It is possible to see the eastward $E_{(\phi)}$ in the raised band (region 2) is larger compared to the background value (region 0), and through $\vec{E}\times\vec{B}$ drifts the layer will raise in altitude in an unstable manner. Conversely, the eastward electric field $E_{(\phi)}$ in the lowered band (region 1) is smaller with respect to the background electric field. Hence, the unstable process will continue in both region1 and 2. These processes are important to explain how instability is created and sustained for the maintenance of divergence free current density. Thus divergence free current density maintenances is important for the simulation of MSTIDs. Without this condition, the polarization electric fields are not generated or maintained and instability would not be generated. Figure 8.2a shows a clearer picture of how the daytime and nighttime MSTIDs are generated as earlier explained in section 2.4.

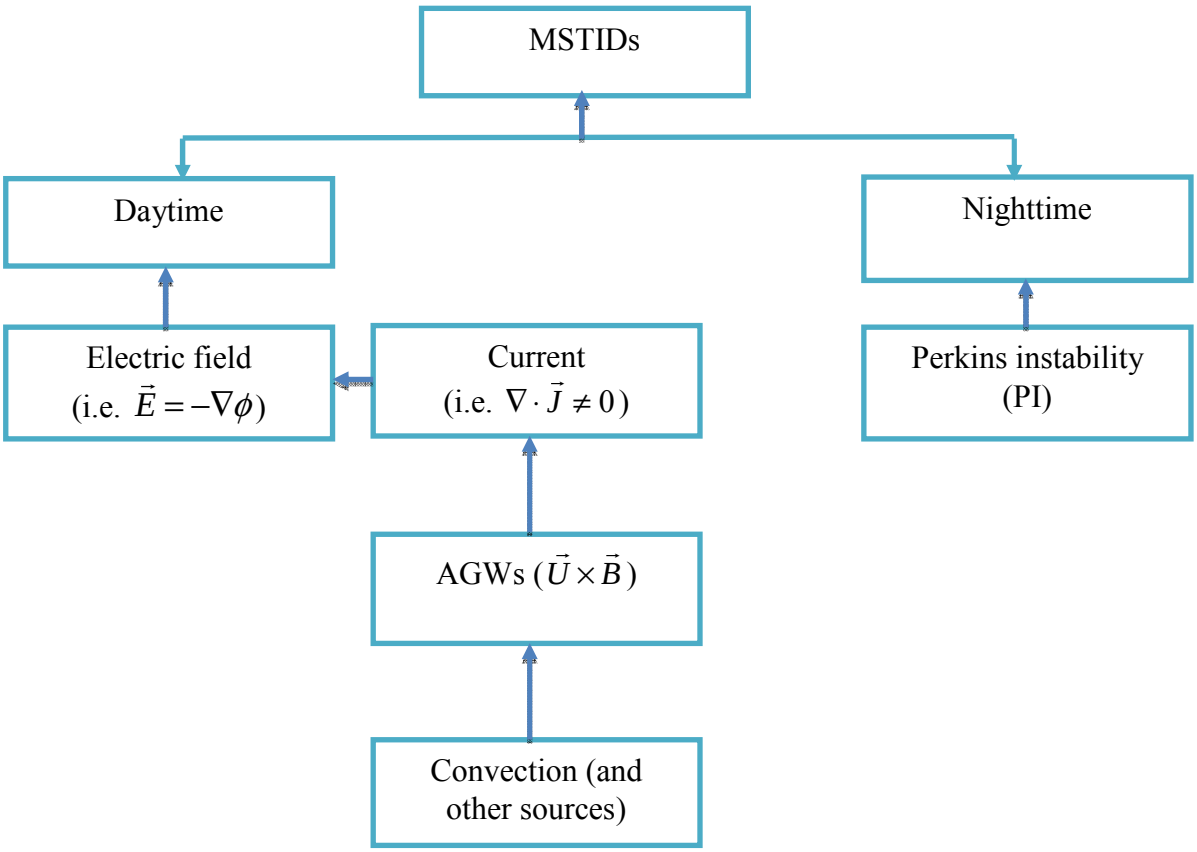

Figure 8.2a - Flow chart of the MSTIDs generation

8.3 IMPLEMENTATION OF SAMI3 IN PARALLEL PROGRAMING

SAMI3 3 consists of approximately 10,000 lines of FORTRAN programming language written in Message passing Interface (MPI) parallelization. The parallelization program is separated in two tasks: the “Master” task and the “Worker” task. An efficient computer system is required to the processing/running of the model. The computer system should have Linux operating system with Intel and openmpi installed on it. To run SAMI 3 model, it is necessary to first run the SAMI2 model which gives temperature and density

background as input to SAMI3 model. The flow chart of how SAMI3 model is executed is shown in Figure 8.3.

It begins with the namelist file, which consist of several input parameter options (e.g. time, solar conditions etc.). At this point an initial run from SAMI2 is necessary to load the background parameters. Then the program is divided into the two sections (i.e. the Master and the Worker task)

The Worker task first initialized the neutral constituents using the MSIS model and transport plasma along the field line by using the ion-continuity equation (equation 1.1)

Data from worker task are then sent to the master task where potentials are solved and solutions are distributed to the respective worker task. Once the worker task receives the potential from current time step, electric field is calculated as $\vec{E} = -\nabla\phi$ and plasma is transported across the magnetic field lines via an $\vec{E} \times \vec{B}$ drift. Thereafter the new time step is calculated from the courant condition, Neutral are updated and the process is repeated for the next time step.

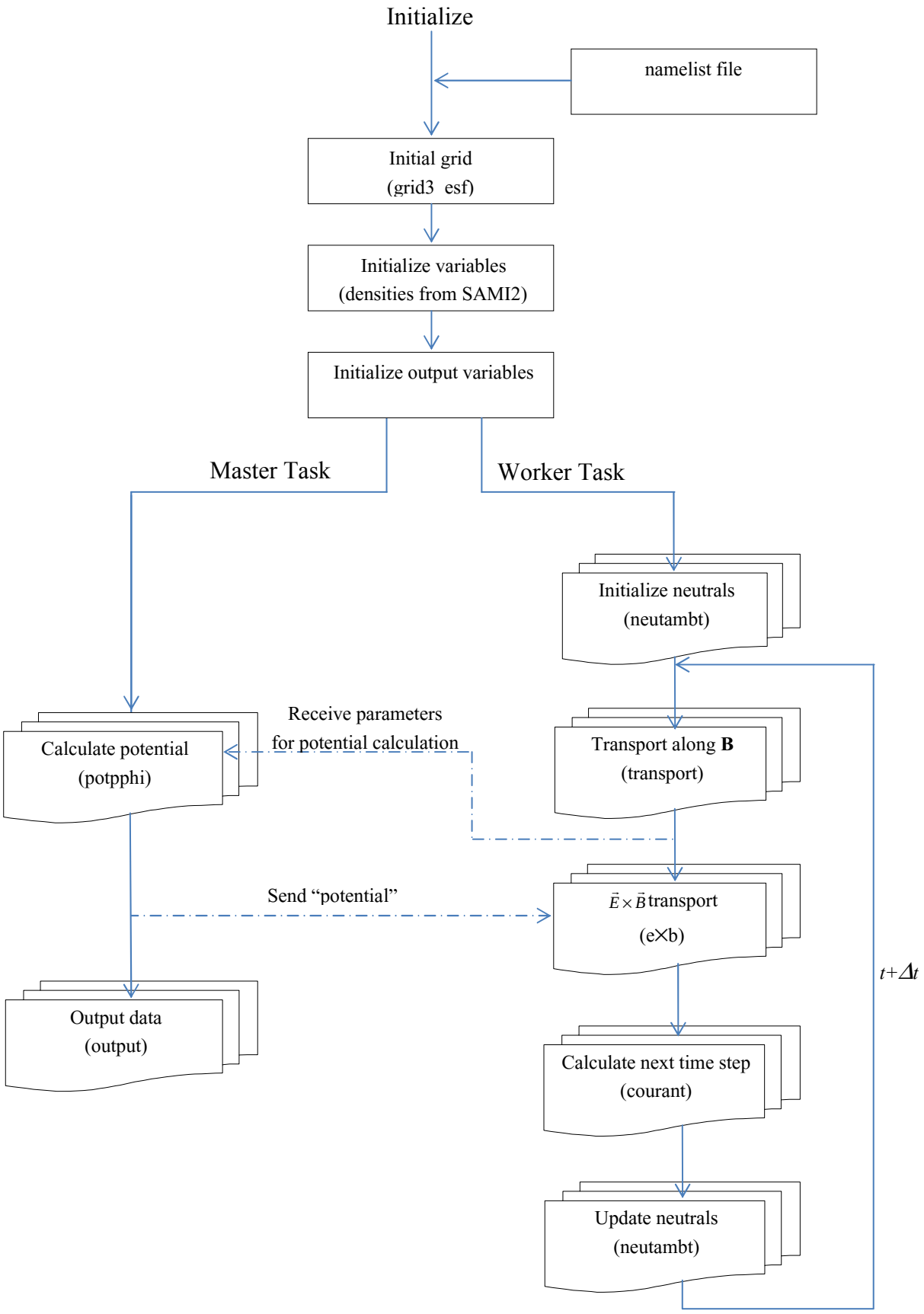

Figure 8.3 – Flow chart of time-sequence of SAMI3 numerical simulation.

8.4 Input Parameters

To run SAMI3 numerical model, it is necessary to run SAMI2 for 48 hours and the results from this SAMI2 would serves as input to SAMI3 initialization. Thereafter SAMI3 was run for hours with the following geophysical parameters which correspond to the parameters from the observed MSTIDs in the present study (section 6): Date: 18/12/2014, F10.7 = 206, F10.7A=133, Ap = 5, and day of the year = 352. The background neutral composition and temperature are specified using NRLMSISE-00. The background wind is not considered because we are only interested in the effect of the gravity waves on MSTIDs. The grid configuration used in this study has a resolution of (n_z, n_f, n_l) which implies (200, 101, 96) respectively, where n_z is the number of grid point along each magnetic field line, n_f is the number in altitude, and n_l is the number in longitude. Based on these grid configurations, the longitude extends from 300° to 304° (4°), latitude covers $\pm$43° and the altitude ranges from 85 to 6000 km with peaks at the equator.

8.5 Applied Perturbation

The gravity wave perturbation is given as a sinusoid perturbation in the region of interest (magnetic latitude = -15° to -10°). First, we perturb the background density ($\tilde{n}$) with $\tilde{n} \Rightarrow e^{i(k_y\hat{y}+k_x\hat{x}-wt)}$, run the model and obtain the data. Secondly we applied the same perturbation ($\tilde{v} \Rightarrow e^{i(k_y\hat{y}+k_x\hat{x}-wt)}$) to the meridional wind component (v). The background and the perturbation terms in both cases can be represented as:

$$n \Rightarrow n_o + \tilde{n}$$
$$v \Rightarrow v_o + \tilde{v} \qquad (8.1)$$

This perturbations are similar to Duly et al. (2014) and Huba et al. (2015). TEC was synthetically generated by integrating vertically the electron density (n_e) from the altitudes of 250 km to 450 km:

$$TEC = \int_{250km}^{450km} n_e dh \qquad (8.2)$$

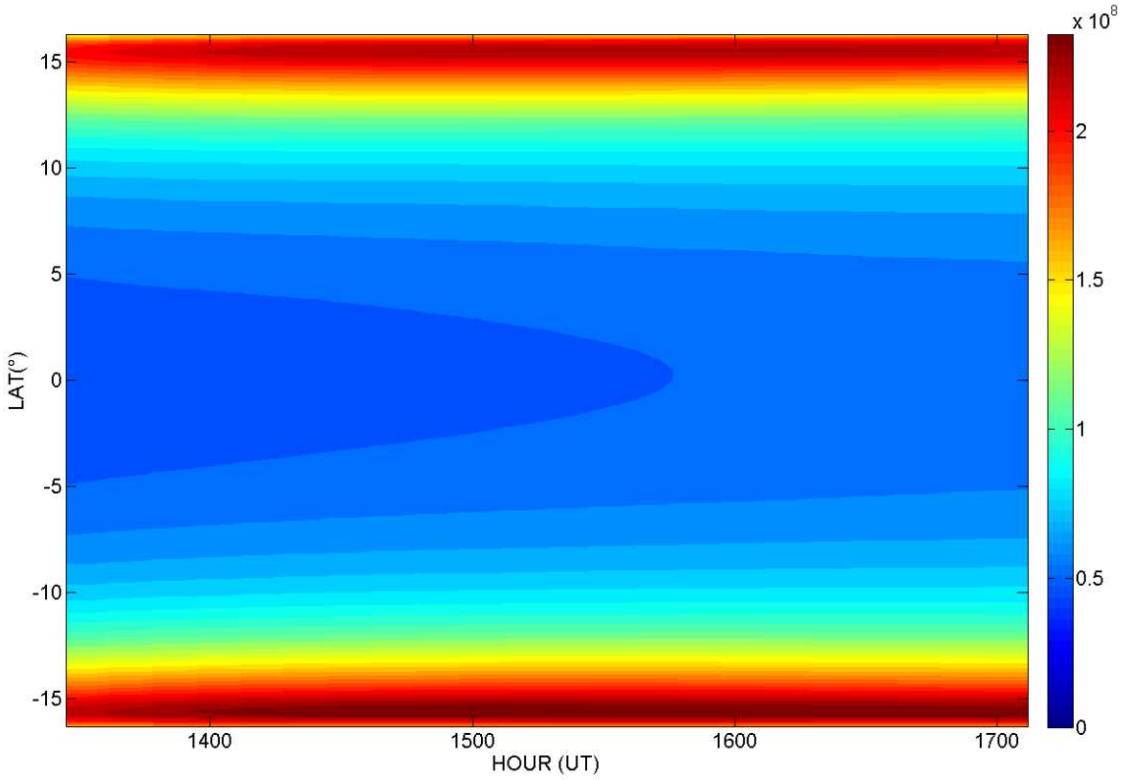

Figure 8.4 - TEC estimated within the SAMI3 numerical model for a self-consistent generation of MSTIDs displaying both northern and southern hemisphere and covering from low latitudes to the equator.

Figure 8.4 show TEC in latitude as a function of time from the model with gravity wave perturbation. The $\Delta TEC = TEC_{(t)} - TEC_0$, where $TEC_{(t)}$ and TEC_0 are the number of integrated electron densities at current and initial time respectively. Results are obtained for the two cases:

Case I: Background density perturbation. Figure 8.5 shows a given perturbation of the background density where it is possible to observe MSTIDs propagations without mapping to conjugate hemisphere. There are no MSTIDs mapping to conjugate region because just perturbing the electron density does not generate a perturbed electric field.

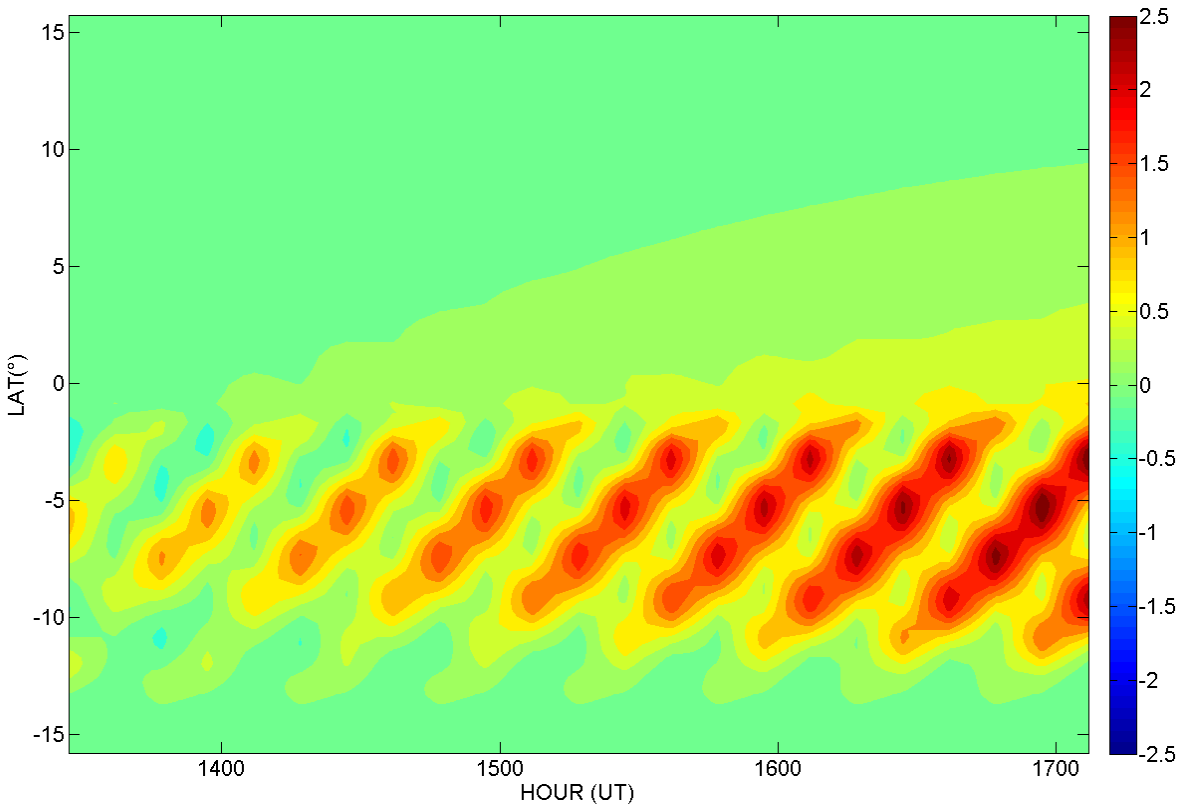

Figure 8.5 - Background density perturbation run obtained by taking the difference in the integrated electron density at current time from initial time.

Case II: Neutral wind perturbation. Figure 8.6 shows the perturbed TEC as a result of wind perturbation which has effects on the electric field (i.e. $\vec{E} = -\nabla\phi$). It is possible to observe that although the perturbation was applied in the southern hemisphere, MSTIDs maps to conjugate hemisphere and create mirrored structures. This confirms electric field involvement in the MSTIDs mapping. The MSTIDs amplitudes in the northern hemisphere are smaller compared to the source hemisphere. Previous works have shown the mapping effects of MSTIDs during nighttime. E.g. the work of Otsuka et al. (2004) and the features of the current modeling and observational studies agree well with the conjugate results. The mapping occurs as a result of high conductivity along magnetic field line, which is reasonably modeled in SAMI3. This means that perturbing the

neutral wind would cause an electric field to be generated. The electric field maps along the field line to conjugate region and generates a density perturbation. That is, as the electric field associated with MSTIDs develops in the Southern hemisphere (source hemisphere), its maps along magnetic field lines and produce similar MSTIDs effects in the density at conjugate hemisphere. This is in agreement with the nighttime simulation studies of Duly et al. (2014) on a self-consistent generation of MSTIDs within SAMI3 numerical model and Huba et al. (2015) which is based on modeling the ionospheric impact of tsunami-driven gravity waves with SAMI3.

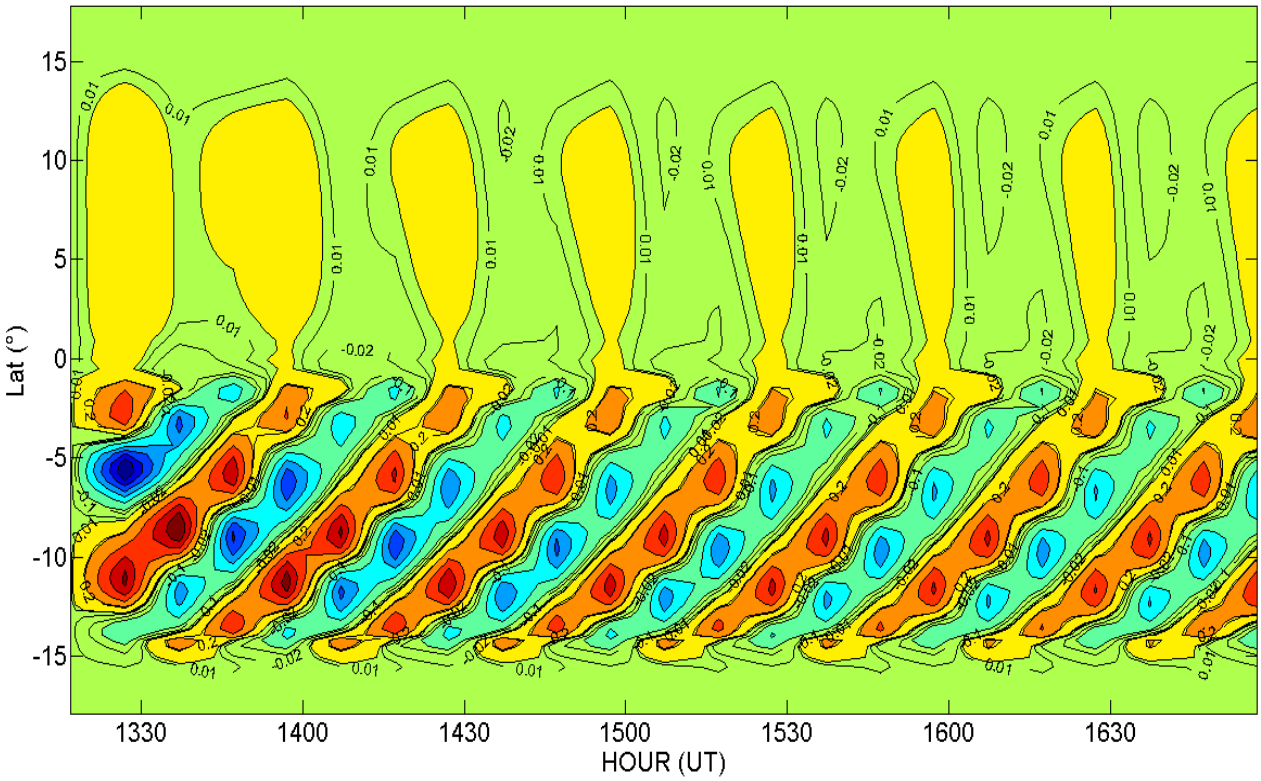

Figure 8.6 – Meridional neutral wind perturbation run obtained by taking the difference in the integrated electron density at current time from initial time.

Apart from the mapping characteristics of the MSTIDs in Figure 8.6, it is possible to also observe a propagation in time towards equator and in the

eastward direction as depicted by the middle panel and the bottom panels. This is the preferential daytime MSTID direction which agree with observation from Jonah et al, (2016) and Hernández-Pajares et al. (2006; 2012). The preferential propagation of MSTIDs towards equator could be owing to increasing perturbation electric field potential towards equator which is inversely proportional to background Pederson conductivity and Pederson conductivity is directly proportional to electron density, which decrease towards equator due to equatorial ionization anomaly phenomenon. Kotake et al. (2007) and Jonah et al. (2016) also explain the phenomenon to be due to the neutral particles oscillation parallel to $\vec{B}$ being larger for gravity wave travelling equatorward than those travelling in other directions, while the eastward propagation directions are mainly due to the distributions of the source around the observation site as illustrated in our observation results.

To show a clear horizontal structure of MSTID mapping, we present a ΔTEC in Figure 8.7 in latitude and longitude plane at 16UT.

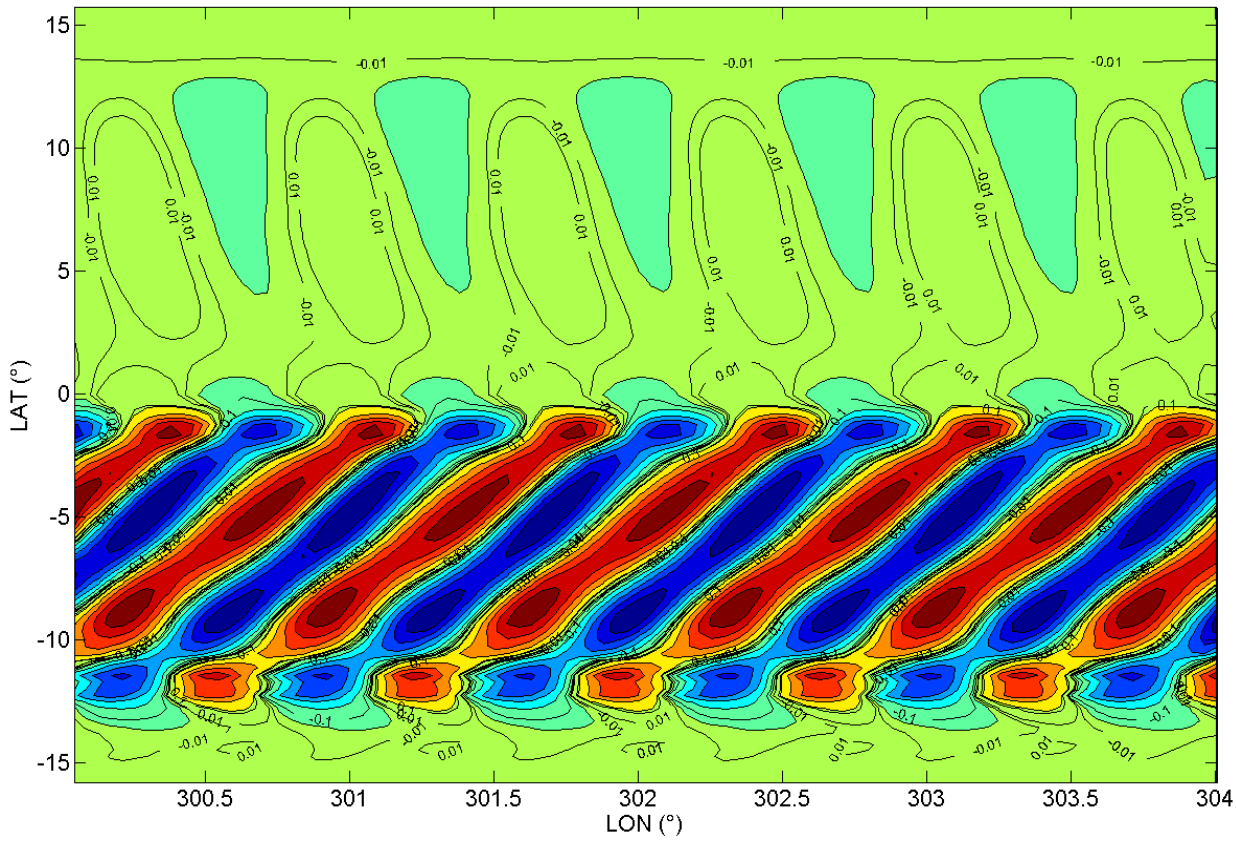

Figure 8.7. Horizontal structure of MSTID mapping in latitude and longitude plane at 16UT for the meridional wind perturbation.

Figure 8.7 shows the ΔTEC in latitude and longitude at 16.00UT. It is possible to observe an equatorward and eastward propagation of MSTIDs. Most importantly we could also observe a mirrored image of the MSTIDs at the opposite hemisphere similar to the previous keogram figures. This indicates that the SAMI3 numerical model is capable of not only reproducing the MSTIDs but also the mapping structure.

9.0 CONCLUSIONS

This thesis has provided insights to the understanding of daytime MSTIDs generations and propagations using both observational and simulation techniques over the low and equatorial regions of the Brazilian sector. Most importantly it shows that MSTIDs are not restricted to mid-latitudes but are also manifested at low to equatorial latitudes. Employing several measuring instruments such as the GNSS receivers distributed all over the Brazilian sector, constellations of satellite from COSMIC mission, GOES satellite and two digisondes located at Boa Vista and Campo Grande to describe the important physical concepts and behavior of daytime MSTIDs over the Brazilian sector were described. Two 3-dimensional ionospheric models, the Convective Atmosphere-ionosphere coupling model (CAI-CM) and the SAMI3 (Naval Research Laboratory) were also used to give more perceptions and interpretations of the mechanisms responsible for the observed MSTIDs. The principal conclusions are organized below:

9.1 Observational conclusions:

We present MSTIDs over southern hemisphere during four days, 5-6 and 26-27 December 2011, using all the various measurements mentioned above. We examine the spatial-temporal distributions of Total Electron Content (TEC) during 12-17 UT covering the ionospheric domain of 30^{o}S−20^{o}S latitude and 45^{o}−55^{o}W longitude. The investigations into the mechanism responsible for the AGW-MSTIDs are also carried out.

For the TEC data, we derive the ΔTEC disturbance by subtracting the TEC mean from corresponding best fitted (TEC_{fit}) obtained using a polynomial fit of order 7. This fitting is done in time and the temporal variation of ΔTEC and is derived at several locations within the ionospheric domain to generate the keogram of TEC. Furthermore, cross-correlation keograms of these spatially distributed ΔTEC are obtained in latitude and longitude.

These keograms suggest that the ΔTEC disturbances acquire the wave characteristics during 13-16 UT that propagate equatorward/eastward and having S-N average wavelength in the 255 - 389 km range and W-E average wavelength in the 184 - 322 km range. These characteristics classify the ΔTEC disturbances as MSTIDs resembling the MSTIDs characteristics widely reported over northern hemisphere.
This study also reports strong summer daytime MSTIDs occurrence for four days during December 2011 using detrended TEC parameter, which was not observed before over southern hemisphere. Other past studies at this region have only identified winter daytime MSTID occurrence.

A possible connection between the observed MSTIDs and gravity waves is examined by analyzing the temporal variation of the F region height (h) inferred from digisonde over a low-to-mid-latitude station on 5 and 6 December 2011. We derive the Δh by subtracting the h from its best fitted (h_{fit}) at 6, 7, 8 and 9 MHz and also obtained the cross-correlation map of height distribution of h. They show the maximum cross-correlation occurring between 13-16 UT also revealing the downward phase propagation in time suggesting the enhanced gravity wave activity during the time when MSTIDs are observed. These characteristics are found to be similar on day-to-day basis.

Our results show a close correlation between enhanced MSTIDs and AGW during daytime on day-to-day basis and bring out the issue about the convection activity as AGW generation.

We show cloud convection activity as an important factor of AGW-MSTIDs generation during daytime between the hours of 12 to 17 UT for the analyzed days. Results presented in this study also show a clear observation of upward propagating AGW from lower atmosphere to upper atmosphere which is important for atmosphere-ionosphere coupling.

We also show that eastward propagation directions of MSTIDs are due mainly to the distributions of the source around the observation sites.

Although, nighttime MSTIDs are associated with nighttime electrodynamics processes and the daytime MSTIDs are related to AGW, it should be mentioned that the nighttime MSTIDs in the northern and southern hemisphere propagate in same direction i.e. equatorward-westward and this same hemispheric directivity (as–shown in Figure 5.11) is explained as due to the geomagnetic conjugate dynamics (OTSUKA et al., 2004). For the daytime MSTIDs, with the input from our present study, Hernández-Pajares et al. (2006, 2012) and Jonah et al. (2016), it is clear that these MSTIDs propagate to the same direction in both hemispheres. Therefore, similar hemispheric directivity (as shown in Figure 5.11) for the daytime MSTIDs can possibly also be attributed to the geomagnetic conjugate dynamics.

9.1.1 Geomagnetic conjugate mapping

This is the first time the daytime MSTID was observed at conjugate hemispheres. The geomagnetic conjugate daytime MSTIDs mapping over Brazilian sector during four days, 5-6 and 26-27 December 2011 covering the ionospheric domain of 0^{o} − 20^{o}S latitude and 45^{o} − 60^{o}W longitude (comprising of both hemisphere geomagnetically) is documented. We further investigate the mechanism involved in its mapping to conjugate hemisphere. The following main conclusions were drawn:

- Experimental MSTIDs at geomagnetic conjugate hemispheres are observed for the first time over the Brazilian sector during daytime.
- The MSTIDs seem to have larger TEC perturbation amplitude at the southern hemisphere; hence, we refer to this hemisphere as the source hemisphere.
- MSTIDs phase velocity is directed toward the southeast in the northern hemisphere and towards the northeast in the southern hemisphere.
-

- We show that with the partial absence of short circuiting in the E region, electric field generated in the F region could be sustained and map along the magnetic field lines to the conjugate F region hemisphere. Thus the MSTIDs at conjugate regions are caused by these electric fields in the F region ionosphere as observed in our results
- Investigations also show that F region magnetic field aligned integrated conductivity could have more influence than E region conductivity during the mapping period

9.2 Simulation conclusions

9.2.1 CAI-CM numerical model

The CAI-CM was used to self-consistently generate MSTIDs from convection source. The model allows us to demonstrate in 3D concentric circular wavefronts as they progressively propagate outward from their convection sources.

The simulation results from the model are in good agreement with the observation result of this study.

With the CAI-CM we are able to prove how different convective sources (strong/weak) excite different level of MSTIDs (well developed/weakly developed MSTIDs).

The CAI-CM through the viscous dissipation generates a thermosphere body force which gave rise the secondary AGW in the thermosphere and consequent generation of MSTIDs in the region.

9.2.2 Conclusion from SAMI3 numerical Model

We used the SAMI3 numerical model to show the self-consistent generation of daytime MSTIDs at conjugate hemispheres. The seeding mechanism (i.e. the gravity wave induced perturbation) was directly applied within the Model.

After the establishment a self-consistent simulation of MSTID in SAMI3, the synthetic observation of TEC were calculated and thereafter the ΔTEC are captured as MSTID results shown.

Most importantly, we investigated the electric field involvement of MSTIDs mapping to opposite hemisphere by including the initial meridional wind perturbation in the southern hemisphere and observed that the signature of the instability appeared in the conjugate northern region. It is believed that density perturbation at the conjugate hemisphere are generated by the polarization electric field mapping along the field line to the conjugate region which arise owing to the current divergent free condition (i.e. $\nabla \cdot \vec{J} = 0$), as explained in section 7.3.

This effect has been previously observed during nighttime period by Otsuka et al. (2004) using experimental results and by Duly et al, (2014) and Huba et al. (2015) using simulation results. However, the results from the present study are novel results of self-consistent modeling of MSTIDs during daytime within numerical framework of SAMI3 model. These modeling results do not only match the experimental result carried out in this thesis but are also found to have good agreements with their nighttime counterpart in past literatures.

9.3 Some potential research topics

- The present study focus on AGW-MSTID activities during tropospheric convection. It would be recommended to carry out the same study during Sudden Stratospheric Warm (SSW) events.
- It would be interesting to carry out further investigations on whether stationary or moving convection source is crucial to the excitement of AGW.
- Part of the CAI-CM used in this thesis could be included in the SAMI3 numerical model in order to implement the source mechanism for MSTIDs from the atmosphere rather than directly from the thermosphere.

REFERENCES

ABDU, M. A.; BATISTA, I. S.; KANTOR, I. J.; SOBRAL, J. H. A. Gravity wave induced ionization layers in the night F -region over Cachoeira Paulista (22◦S, 45°W). **Journal of Atmospheric and Solar-Terrestrial Physics**, v. 44, n. 9, p. 759–767, 1982.

ABDU, M. A. Equatorial ionosphere–thermosphere system: electrodynamics and irregularities, **Advance in Space Research***,* v. 35, p. 771–787, 2005.

ABDU, M. A.; DE SOUZA, J. R.; KHERANI, E. A.; BATISTA, I. S.; MACDOUGALL, J. W.; SOBRAL, J. H. A. Wave structure and polarization electric field development in the bottomside F layer leading to postsunset equatorial spread F. **Journal of Geophysical Research**, v. 120, n. 8, p. 6930-6910, Aug. 2015. doi:10.1002/2015JA021235.

AFRAIMOVICH, E.L.; DEMYANOV, V.V.; KONDAKOVA, T.N. Degradation of performance of the navigation GPS system in geomagnetically disturbed conditions. **GPS Solutions,** Springer, v. 7, n. 2, 2003. DOI 10.1007/s10291-003-0053-7.

ALEXANDER, M. J.; BARNET, C. Using satellite observations to constrain parameterizations of gravity wave effects for global models. **Journal of Atmospheric Science**, v. 64, n. 5, p. 1652–1665, 2007.

ANTHES, R. A. The COSMIC/FORMOSAT-3 mission: early results. **Bull. Am. Meteorol. Soc**, v. 89, p. 313–333, 2008,

AMORIM, D. C. M.; PIMENTA, A. A.; BITTENCOURT,J. A.; FAGUNDES, P. R. Long term study of medium scale traveling ionospheric disturbances using O I 630nm all sky imaging and ionosonde over Brazilian low latitudes. **Journal of Geophysical Research,** v. 116, N. A06312, 2011. doi:10.1029/2010JA016090.

BEHNKE, R. A. F. Layer height bands in the nocturnal ionosphere over Arecibo, **Journal of Geophysical Research**, v. 84, p. 974-978, 1979.

BLEWITT, G. Basics of the GPS technique: observation equations. In: JOHNSON. B. (ed.) **Geodetic applications of GPS.** Sweden: Nordic Geodetic Commission, 1997. p. 10–54. ISSN 0280-5731.

BOWMAN, G.G. A review of some recent work on mid-latitude spread-F occurrence as detected by ionosondes. **Journal of Geomagnetism and Geoelectricity**, v. 42, p. 109–138, 1990.

BREIT, G.; TUVE, M. A. A radio method of estimating the height of the conducting layer. **Nature**, v .116, p. 357, 1925.

BRISTOW, W. A.; GREENWALD, R. A. Multiradar observations of medium-scale acoustic gravity waves using the Super Dual Auroral Radar Network. **Journal of Geophysical Research**, v. 101, p. 24499–24511, 1996.

BRUINSMA, S. L.; FORBES J. M. Medium- to large-scale density variability as observed by CHAMP, **Journal of Geophysical Research**, v. 6, n. S08002, 2008. doi:10.1029/2008SW000411.

BURNSIDE, R. G.; WALKER, J. C.G.; BEHNKE, R. A.; GONZALES C. A. Polarization electric fields in the nighttime F layer at Arecibo. **Journal of Geophysical Research**, v.88, n. A8, p.6259–6266, 1983. doi:10.1029/JA088iA08p06259.

CANDIDO, C. M. N.; PIMENTA, A. A.; BITTENCOURT, J. A.; BECKER-GUEDES, F. Statistical analysis of the occurrence of medium-scale traveling ionospheric disturbances over Brazilian low latitudes using OI 630.0 nm emission all-sky images. **Geophysical Research Letter**, v. 35, n. L17105, 2008. doi:10.1029/2008GL035043.

DAVIES, K. **Ionospheric radio propagation**. Dover Publications Inc., Manufactured in the United States of America, 1965.

DULY, T. M.; HUBA, J. D.; MAKELA, J. J. Self-consistent generation of medium-scale traveling ionospheric disturbances (MSTIDS) within the sami3 numerical model. **Journal of Geophysical Research**, v. 119, p. 6745–6757, 2014. doi:10.1002/2014JA020146.

FEJER, B. G. F region plasma drifts over Arecibo: solar cycle, seasonal, and magnetic activity effects. **Journal of Geophysical Research**, v. 98, n. A8, 13645- 13652, 1993. doi:10.1029/93JA00953.

FONG, C. J.; YANG, S. K.; CHU, C. H.; HUANG, C. Y.; YEH, J.J.; LIN, C.T.; KUO, T.C.; LIU, T. Y.; YEN, N.; CHEN, S. S.; KUO, Y. H.; LIOU, Y. A.; CHI, S. FORMOSAT-3/COSMIC constellation spacecraft system performance: After one year in orbit. **IEEE Trans. Geosci. Remote Sens**., v. 46, n. 11, 2008.

FORBES, J.; MARCOS, F.; KAMALABADI, F. Wave structures in lower thermosphere density from satellite electrostatic triaxial accelerometer measurements. **Journal of Geophysical Research**., v.100, n. A8, p. 14,693 – 14,701, 1995.

FRITTS, D. C. Shear excitation of atmospheric gravity waves. **Journal of Atmospheric Science**, v. 39, p. 1936, 1982.

FRITTS, D. C.; ALEXANDER, M. J. Gravity wave dynamics and effects in the middle atmosphere, **Rev. Geophys**., v. 41, n. 1, p. 1003, 2003. doi: 10.1029/2001RG000106.

FRITTS, D. C. Shear excitation of atmospheric gravity waves. **Journal of Atmospheric Science**, v.39, p.1936–1952, 1982.

FRITTS, D. C.; WANG, L.; WERNE, J.; LUND, T.; WAN, K. Gravity wave instability dynamics at high Reynolds numbers. Part I: wave field evolution at large amplitudes and high frequencies. **J. Atmos. Sci**., v. 66, p.1126 - 1148, 2009. doi:10.1175/2008JAS2726.1.

FUKAO, S.; KELLEY, M. C.; SHIRAKAWA, T.; TAKAMI, T.; YAMAMOTO, M.; TSUDA, T.; KATO, S. Turbulent upwelling of the midlatitude ionosphere, 1, Observational results by the MU radar. **Journal of Geophysical Research**, v. 96, p. 3725-3746,1991.

FUKUSHIMA, D.; SHIOKAWA, K.; OTSUKA, Y.; OGAWA, T. Observations of equatorial nighttime medium-scale traveling ionospheric disturbances in 630-nm airglow images over 7 years. **Journal of Geophysical Research**., v. 117, n. A10324, 2012. doi:10.1029/2012JA017758.

GALERA, M. J. F. **Posicionamento pelo GNSS -** descrição, fundamentos e aplicações. 2. Ed, Publishing Foundation of UNESP, 2008. ISBN 978-85-7139-788-0.

GALVAN, D. A.; KOMJATHY, A.;HICKEY, M. P.; MANNUCCI, A. J. The 2009 Samoa and 2010 Chile tsunamis as observed in the ionosphere using GPS total electron content. **Journal of Geophysical Research**., v. 116, A06318, 2011. doi:10.1029/2010JA016204.

GARCIA, F. J.; KELLEY, M. C.; MAKELA, J. J.; HUANG C. S. Airglow observations of mesoscale low-velocity traveling ionospheric disturbances at midlatitudes. **Journal of Geophysical Research**, v. 105, p. 18,407– 18,415, 2000.

GROCOTT, A.; HOSOKAWA, K.; ISHIDA, T.; LESTER, M.; MILAN, S. E.; FREEMAN, M. P.; SATO, N.; YUKIMATU, A. S. Characteristics of medium-scale traveling ionospheric disturbances observed near the Antarctic Peninsula by HF radar. **Journal of Geophysical Research**, v.118, p. 5830–5841, 2013. doi:10.1002/jgra.50515.

HARGREAVES, J. K. **The solar-terrestrial environment.** New York: Cambridge Univ. Press, 1992. Atmospheric and Space Science Series.

HERNANDEZ-PAJARES, M.; JUAN, J. M.; SANZ, J. Medium-scale traveling ionospheric disturbances affecting GPS measurements: Spatial and temporal analysis. **Journal of Geophysical Research**, v. 111, n. A07S11, 2006. doi:10.1029/2005JA011474.

HERNÁNDEZ-PAJARES, M.; JUAN, J. M.; SANZ, J.; ARAGÓN-ÀNGEL, A. Propagation of medium scale traveling ionospheric disturbances at different latitudes and solar cycle conditions. **Radio Science***,* v. 47, RS0K05, 2012. doi:10.1029/2011RS004951.

HINES, C. O. Internal atmospheric gravity waves at ionospheric heights. **Can. J. Phys**., v. 38, p. 1441–1481, 1960.

HOCKE, K.; SCHLEGEL, K. A Review of atmospheric gravity waves and travelling ionospheric disturbances: 1982–1995. **Ann. Geophys**., v. 14, p. 917–940, 1996. doi:10.1007/s00585-996-0917-6.

HOOKE W.H. Ionospheric irregularities produced by internal atmospheric gravity waves. **Journal of Atmospheric and Terrestrial Physics**, v. 30, n. 5, 1968, p. 795–823, 1968.

HOOKE, W. H. Gravity waves. In: RAY, P. S. (ed.). **Mesoscale meteorology and forecasting.** Amer. Meteor. Soc., 1986. p. 272–288.

HOFMANN-WELLENHOF, B.; LICHTENEGGER, H.; COLLINS, J. **GPS** - theory and practice. 3. ed. Wien: Springer-Verlag*,* 1994. 355p.

HOLTON, J. R. **An introduction to dynamic meteorology**. 3.ed. Academic Press, 1992. v. 48. 551p. International Geophysics Series.

HORINOUCHI, T.; NAKAMURA, T.; KOSAKA, J. Convectively generated mesoscale gravity waves simulated throughout the middle atmosphere. **Geophysical Research Letters**, v. 29, n. 21, 33, 34, 48, 2002.

HUANG, C. S.; MILLER, C. A.; KELLEY, M. C. Basic properties and gravity wave initiation of the midlatitude F region instability. **Radio Science***.,* v. 29, n. l, 395405, 1994.

HUBA, J. D.; DROB, D. P.; WU, T. W.; MAKELA, J. J. Modeling the ionospheric impact of tsunami-driven gravity waves with SAMI3: conjugate effects, **Geophysical Research Letter**, v. 42, p. 5719–5726, 2015. doi:10.1002/2015GL064871.

HUBA, J. D.; JOYCE, G.; KRALL, J. Three-dimensional equatorial spread F modeling. **Geophysical Research Letters**, v. 35, L10102, 2008. doi:10.1029/2008GL033509.

HUBA, J. D.; JOYCE G.; FEDDER J. A. SAMI2 is another model of the ionosphere (SAMI2): A new low-latitude ionosphere model. **Journal of Geophysical Research,** v.105, n. A10), p. 035–23,053, 2000.

HUNSUCKER, R. D.; HARGREAVES, J. K. **The high-latitude ionosphere and its effects on radio propagation**. Cambridge University Press, 2003.

HUNSUCKER, R. D. Atmospheric gravity waves generated in the high latitude ionosphere: A review. **Rev. Geophys. Space Phys**., v. 20, p. 293–315, 1982.

JONAH, O.F.; DE PAULA, E.R.; MUELLA, M.T.A.H.; DUTRA, S.L.G.; KHERANI, E.A.; NEGRETI, P.M.S.; OTSUKA, Y. TEC variation during high and low solar activities over South American sector. **Journal of Atmospheric and Solar-Terrestrial Physics***,* v. 135 p. 22–35, 2015. doi:10.1016/j.jastp.2015.10.005.

JONAH, O. F.; DE PAULA, E. R.; KHERANI, E. A.; DUTRA, S. L. G.; PAES, R. R. Atmospheric and ionospheric response to stratospheric sudden warming of January 2013. **Journal of Geophysical Research**., v. 119, n. 6, p. 4973–4980, 2014. doi:10.1002/2013JA019491.

JONAH, O. F.; KHERANI, E. A.; DE PAULA, E. R. Observation of TEC perturbation associated with medium-scale traveling ionospheric disturbance and possible seeding mechanism of atmospheric gravity wave at a Brazilian sector. **Journal of Geophysical Research**, v. 121, n. 3, p. s 2531–2546, 2016. doi:10.1002/2015JA022273.

JONAH, O. F.; KHERANI, E. A.; DE PAULA, E. R. Investigations of conjugate MSTIDs over the Brazilian sector during daytime. **Journal of Geophysical Research** (Submitted)

KELLEY, M. C.; FUKAO, S. Turbulent upwelling of the mid- latitude ionosphere: 2. Theoretical framework. **Journal of Geophysical Research***,* v. 96, n. A3, p. 3747-3753, 1991.

KELLEY M.C. On the origin of mesoscale TIDs at midlatitudes. **Ann. Geophys**., v. 29, p. 361–366, 2011, doi:10.5194/angeo-29-361.

KELLEY, C.; MICHAEL; MAKELA, J. J. Resolution of the discrepancy between experiment and theory of midlatitude F-region structures. **Geophysical Research Letters**, v. 28, n. 13, p. 2589-2592, 2001.

KELLEY, M. C. **The Earth's ionosphere***:* plasma physics and electrodynamics. 1. ed. San Diego: Academic Press, 2008. International Geophysics Series.

KHERANI, E. A.; ABDU, M. A.; FRITTS, D. C.; PAULA, E. R. DE. The acoustic gravity wave induced disturbances in the equatorial ionosphere. In: Abdu, M. A.; Pancheva, D. (Ed.). **Aeronomy of the Earth's Atmosphere and Ionosphere**, cap. 10, p. 141–162, 2011.

KHERANI, E. A.; LOGNONNÉ, P.; HÉBERT, H.; ROLLAND, L.; ASTAFYEVA, E.; OCCHIPINTI, G.; COISSON, P.; WALWER, D.; DE PAULA, E. R. Modelling of the total electronic content and magnetic field anomalies generated by the 2011 Tohoku-Oki tsunami and associated acoustic-gravity waves. **Geophysical Journal International**, v.191, p.1049–1066, 2012. doi: 10.1111/j.1365-246X.2012.05617.x.

KHERANI, E. A.; ROLLAND, L.; LOGNONNÉ, P.; SLADEN, A.; KLAUSNER, V.; DE PAULA, E. R. Traveling ionospheric disturbances propagating ahead of the Tohoku-Oki tsunami: a case study. **Geophysical Journal International,** v. 204, p. 1148-1158, 2016.

KOTAKE, N.; OTSUKA, Y.; TSUGAWA, T.; OGAWA, T.; SAITO, A. Climatological study of GPS total electron content variations caused by medium-scale traveling ionospheric disturbances. **Journal of Geophysical Research**, v.111, n. A04306, 2006. doi:10.1029/2005JA011418.

KOTAKE, N.; OTSUKA, Y.; TSUGAWA, T.; OGAWA, T.; SAITO, A. Statistical study of medium-scale traveling ionospheric disturbances observed with the GPS networks in Southern California. **Earth Planets Space**, v. 59, p. 95–102 , 2007.

KUO, Y. H.; WEE, T.K.; SOKOLOVSKIY, S.; ROCKEN, C.; SCHREINER, W.; HUNT, D.; ANTHES, R. A. Inversion and error estimation of GPS radio occultation data. **J. Meteor. Soc. Japan***,* v. 82, p. 507–531, 2004.

LANCHESTER, B.S.; NYGREN, T.; JARVIS, M.J.; EDWARDS, R. Gravity wave parameters measured with EISCAT and Dynasonde. **Annales Geophysicae**, v. 11, p. 925–936, 1993.

LARSEN, M. F.; SWARTZ, W. E.; WOODMAN, R. F. Gravity-wave generation by thunderstorms observed with a vertically-pointing 430MHz radar. **Geophysical Research Letter**, v. 9, p. 571–574, 1982.

MACDOUGALL, J.; ABDU, M.; BATISTA, I.; FAGUNDES, P. R.; SAHAI, Y.; JAYACHANDRAN, P. T. On the production of traveling ionospheric disturbances by atmospheric gravity waves. **Journal of Atmospheric and Solar-Terrestrial Physics**, v. 71, p. 2013–2016, 2009b. doi:10.1016/j.jastp.2009.09.006b.

MACDOUGALL, J. W.; JAYACHANDRAN, P. T. Spaced transmitter measurements of medium scale traveling ionospheric disturbance near equator. **Geophysical Research Letter,** v. 38, n. L16806, 2011. doi:10.1029,2011GL048598.

MACDOUGALL, J.; LI, G.; JAYACHANDRAN, P. T. Traveling ionospheric disturbances near London. **Journal of Atmospheric and Solar-Terrestrial Physics** v. 71, p. 2077–2084, 2009a. doi:10.1016/j.jastp.2009.09.016.

MAKELA, J. J.; LOGNONNÉ, P.; HÉBERT, H.; GEHRELS, T.; ROLLAND, L.; ALLGEYER, S.; KHERANI, E. A.; OCCHIPINTI, G.; ASTAFYEVA, E.; COÏSSON, P.; LOEVENBRUCK, A.; CLÉVÉDÉ, E.; KELLEY, M. C.; LAMOUROUX, J. Imaging and modeling the ionospheric airglow response over Hawaii to the tsunami generated by the Tohoku earthquake of 11 March 2011. **Geophysical Research Letter**, v. 38, n. L00G02, 2011. doi:10.1029/2011GL047860.

MARTINIS, C.; BAUMGARDNER, J.; WROTEN, J.; MENDILLO, M. Seasonal dependence of MSTIDs obtained from 630.0 nm airglow imaging at Arecibo. **Geophysical Research Letter,** v. 37, n. L11103, 2010. doi:10.1029/2010GL043569.

MARSHAM, J. H.; PARKER, D. J. Secondary initiation of multiple bands of cumulonimbus over southern Britain. II: Dynamics of secondary initiation. **Q. J. R. Meteorol. Soc**., v. 132, p. 1053–1072, 2006.

MCFARLANE, N. A. The effect of orographically excited gravity wave drag on the general circulation of the lower stratosphere and troposphere. **Journal of Atmospheric Science**, v. 44, p. 1775–1800, 1987.

MEDVEDEV, A. S.; YIGIT, E.; HARTOGH, P.; BECKER, E. Inuence of gravity waves on the Martian atmosphere: general circulation modeling. **Journal of Geophysical Research**, v. 116, n. E10004, 2011. doi:10.1029/2011JE003848.

MENDILLO, M.; BAUMGARDNER, J.; NOTTINGHAM, D.; AARONS, J.; REINISCH, B.; SCALI, J.; KELLEY, M. Investigations of thermospheric-ionospheric dynamics with 6300-A° images from the Arecibo Observatory. **Journal of Geophysical Research,** v. 102, p. 7331– 7343, 1997.

MILLER E.S.; SWARTZ, W. E.; KELLEY, M. C.; MENDILLO, M.; NOTTINGHAM, D.; SCALI, J.; REINISCH, B. Electrodynamics of midlatitude spread F, 1. Observations of unstable, gravity wave-induced ionospheric electric fields at tropical latitudes. **Journal. Geophysical. Research**., v. 102, p. 11521-11532, 1997.

MOHANNAKUMAR, K. **Stratosphere troposphere interaction**: an introduction. Cochin, India: Springer, 2008.

NICOLLS, M. J., AND KELLEY, M. C. Strong evidence for gravity wave seeding of an ionospheric plasma instability. **Geophysical Research Letter***,* v. 32, n. L05108, 2005. doi:10.1029/ 2004GL020737.

NOGUEIRA, P. A. B.; ABDU, M. A.; SOUZA, J. R.; BAILEY, G. J.; BATISTA, I. S. Longitudinal variation in Global Navigation Satellite Systems TEC and topside ion density over South American sector associated with the four-peaked wave structures. **Journal of Geophysical Research***,* v. 118, p. 1–14, 2013. doi:10.1002/2013JA019266.

OGAWA, T.; NISHITANI,N.; OTSUKA,Y.; SHIOKAWA, K.; TSUGAWA, T.; HOSOKAWA, K. Medium-scale traveling ionospheric disturbances observed with the SuperDARN Hokkaido radar, all-sky imager, and GPS network and their relation to concurrent sporadic E irregularities. **Journal of Geophysical Research**, v. 114, n. A03316, 2009. doi:10.1029/2008JA013893.

OLIVER, W. L.; OTSUKA, Y.; SATO, M.; TAKAMI, T.; FUKA, O. S. A climatology of F-region gravity wave propagation over the middle and upper atmosphere radar. **Journal of Geophysical Research,** v. 102, p. 14499–14512, 1997.

OTSUKA, Y.; KOTAKE, N.; SHIOKAWA, K.; OGAWA, T.; TSUGAWA, T.; SAITO, A. Statistical study of medium-scale traveling ionospheric disturbances observed with a GPS receiver network in Japan. **Aeronomy of the Earth's Atmosphere and Ionosphere***,* IAGA Special Sopron Book Series, v. 2, p. 291–299, 2011. doi:10.1007/978-94-007-0326-1 21.

OTSUKA, Y.; SUZUKI, K.; NAKAGAWA, S.; NISHIOKA, M.; SHIOKAWA, K.; TSUGAWA, T. GPS observations of medium-scale traveling ionospheric disturbances over Europe. **Ann. Geophys**., v. 31, p. 163–172, 2013. doi:10.5194/angeo-31-163.

OTSUKA, Y.; SHIOKAWA, K.; OGAWA, T.; WILKINSON, P. Geomagnetic conjugate observations of medium-scale traveling ionospheric disturbances at midlatitude using all-sky airglow imagers. **Geophysical Research Letter**, v.31, n. L15803, 2004. doi:10.1029/2004GL020262.

OTSUKA, Y.; OGAWA, T.; SAITO, A.; TSUGAWA, T.; FUKAO, S.; MIYAZAKI, S. A new technique for mapping of total electron content using GPS network in Japan. **Journal of Earth Planets Space**, v. 54, p. 63–70, 2002.

PAES, R. R.; BATISTA, I. S.; CANDIDO, C. M. N.; JONAH, O. F.; SANTOS, P. C. P. Equatorial ionization anomaly variability over the Brazilian region during

boreal sudden stratospheric warming events. **Journal of Geophysical Research,** v. 119, 2014. doi:10.1002/2014JA019968.

PAVELIN, E.; WHITEWAY, J. A.; VAUGHAN, G. Observations of gravity wave generation and breaking in the lowermost stratosphere. **Journal of Geophysical Research,** v. 106, n. D6, s 5173–5179, 2001. Doi: 2000JD9000480.

PERKINS, F. Spread F and ionospheric currents. **Journal of Geophysical Research**, v. 78, p. 218–226, 1973.

PFISTER, L.; CHAN, K. R.; BUI, T. P.; BOWEN, S.; LEGG, M.; GARY, B.; KELLY, K.; PROFFITT, M.; STARR, W. Gravity waves generated by a tropical cyclone during the STEP tropical field program: A case study. **Journal of Geophysical Research**, v. 9 8, p. 8611-8638, 1993.

PIANI, C.; DURRAN, D.; ALEXANDER, M. J.; HOLTON, J. R. A numerical study of three dimensional gravity waves triggered by deep tropical convection and their role in the dynamics of the QBO. **Journal of Atmospheric Science**, v. 57, p. 3689–3702, 2000.

PIMENTA, A. A.; KELLEY, M. C.; SAHAI, Y.; BITTENCOURT, J. A.; FAGUNDES, P. R. Thermospheric dark band structures observed in all-sky OI 630 nm emission images over the Brazilian low-latitude sector. **Journal of Geophysical Research**, v. 113, n. A01307, 2008. doi:10.1029/2007JA012444.

RISHBETH, H.; GARRIOTT, O. K. **Introduction to ionospheric Physics**. New York: Academic Press, 1969. v. 14. Series. International geophysics series.

SAITO, A.; FUKAO, S.; MIYAZAKI, S. High resolution mapping of TEC perturbations with the GSI GPS network over Japan. **Geophysical Research Letter,** v. 25, p. 3079–3082, 1998.

SHIOKAWA, K.; IHARA, C.; OTSUKA, Y.; OGAWA, T. Statistical study of nighttime medium-scale traveling ionospheric disturbances using midlatitude airglow images. **Journal of Geophysical Research***,* v. 108, n. A1, 1052, 2003. doi:10.1029/ 2002JA009491.

SHUME, E. B.; RODRIGUES, F. S.; MANNUCCI, A. J.; DE PAULA, E. R. Modulation of equatorial electrojet irregularities by atmospheric gravity waves. **Journal of Geophysical Research**, v. 119, p. 366–374, 66, 67, 74, 2014..

SPIGA, A.; TEITELBAUM, H.; ZEITLIN, H. Identification of the sources of inertia-gravity waves in the Andes Cordillera region. **Ann. Geophys**., v. 26: p. 2551-2568, 2008.

TAKAHASHI , H.; COSTA, S., OTSUKA, Y.; SHIOKAWA, K.; MONICO, J. F. G.; DE PAULA, E.R.; NOGUEIRA, P.; DENARDINI, C.M.; BECKER-GUEDES, F.; WRASSE, C.M.; IVO, A.S.; GOMES, V.C.F.; GARGARELA, J. R.; SANT'ANNA, N.; GATTO, R. Diagnostics of equatorial and low latitude ionosphere by TEC mapping over Brazil. **Advance in Space Research***,* v. 54, p. 385–394, 2014. doi.org/10.1016/j.asr.2014.01.032.

TAKAHASHI, H.; WRASSE, C. M.; DENARDINI, C. M.; PÁDUA, M. B.; DE PAULA, E. R.; COSTA, S. M. A.; OTSUKA, Y.; SHIOKAWA, K.; GALERA MONICO, J. F.; IVO, A.; SANT'ANNA, N. Ionospheric TEC weather map over South America. **Journal of Geophysical Research**, v.14, n. 11, p. 937-949, 2016. doi:10.1002/2016SW001474.

TSUGAWA, T.; SAITO, A.; OTSUKA, Y.; YAMAMOTO, M. Damping of large-scale traveling ionospheric disturbances detected with GPS networks during the geomagnetic storm. **Journal of Geophysical Research**, v. 108, n. A3, p. 1127, 2004. doi:10.1029/2002JA009433.

TSUGAWA, T.; OTSUKA, Y.; COSTER, A. J.; SAITO, A. Medium-scale traveling ionospheric disturbances detected with dense and wide TEC maps over North America. **Geophysical Research Letter,** v.34, n. L22101, 2007. doi:10.1029/2007GL031663.

TSUNODA, R. T. On blanketing sporadic E and polarization effects near the equatorial electrojet. **Journal of Geophysical Research**, v.113, n. A09304, 2008. doi:10.1029/2008JA013158.

UCCELLINI, L. W.; KOCH, S. E. The synoptic setting and possible source mechanisms form mesoscale gravity wave events. **Mon. Weather Rev**., v. 115, p. 721–729, 1987.

VADAS, S. L.; FRITTS, D. Influence of solar variability on gravity wave structure and dissipation in the thermosphere from tropospheric convection. **Journal of Geophysical Research**, v.111, n. A10S12, 2006. doi:10.1029/2005JA011510.

VADAS, S. L. J.; LIU A. Generation of large-scale gravity waves and neutral winds in the thermosphere from the dissipation of convectively generated gravity waves. **Journal of Geophysical Research**, v. 114, n. A10310, 2009. doi:10.1029/2009JA014108.

VADAS, S. L.; TAYLOR, M. J.; PAUTET, P.D.; STAMUS, P. A.; FRITTS, D. C.; LI, H.L.; SÃO SABBAS, F. T.; RAMPINELLI, V. T.; BATISTA, P.; TAKAHASHI, H. Convection: the likely source of the medium-scale gravity waves observed in the OH airglow layer near Brasilia, Brazil, during the SpreadFEx campaign. **Ann. Geophys**., v. 27, p. 231–259, doi: 10.5194/angeo-27-231, 2009.

VALLADARES, C. E.; SHEEHAN, R. Observations of conjugate MSTIDs using networks of GPS receivers in the American sector. **Journal of Geophysical Research***,* v. 51, n.9, p. 1470–1488 , 2016. doi: 10.1002/2016RS005967.

WANG, L.; ALEXANDER, M. J. Gravity wave activity during stratospheric sudden warmings in the 2007–2008 Northern Hemisphere winter. **Journal of Geophysical Research**, v.114, n. D18108, 2009. doi: 10.1029/2009JD011867.

WU, B. H.; FONG, C. J.; HUANG, C. Y.; LIOU, Y. A.; YEN, N.; CHEN, P. FORMOSAT-3/COSMIC mission to global Earth weather monitoring, operation, and TACC/CDAAC post-processing. In: AMS ANNU. MEETING, 86., 2006 - CONF**.** SATELLITE METEOROLOGY AND OCEANOGRAPHY, 14., 2006, Atlanta, GA. **Proceedings…** AMS, 2006.

YAMAMORI M.; SATO, K. Characteristics of inertia gravity waves over the South Pacific as revealed by radio sonde observations. **Journal of Geophysical Research**, v. 111, n. D16110, 2005. doi: 10.1029/2005JD006861.

YIGIT, E.; AYLWARD, A. D.; MEDVEDEV, A. S. Parameterization of the effects of vertically propagating gravity waves for thermosphere general circulation models: sensitivity study. **Journal of Geophysical Research**, v. 113, n. D19106, 2008. doi:10.1029/2008JD010135.

YIGIT, E.; MEDVEDEV, A. S.; AYLWARD, A. D.; RIDLEY, A. J.; HARRIS, M. J.; MOLDWIN, M. B.; HARTOGH, P. Dynamical effects of internal gravity waves in the equinoctial thermosphere. **Journal of Atmospheric and Solar-Terrestrial Physics**, v. 90-91, p. 104–116, 2012. doi: 10.1016/j.jastp.2011.11.014.

YOKOYAMA, T.; HYSELL, D. L. A new midlatitude ionosphere electrodynamics coupling model (MIECO): latitudinal dependence and propagation of medium-scale traveling ionospheric disturbances. **Journal of Geophysical Research,** v. 37, n. L08105, 2010. doi: 10.1029/2010GL042598.

ZETTERGREN, M. D.; SNIVELY, J. B. Ionospheric response to infrasonic-acoustic waves generated by natural hazard events. **Journal of Geophysical Research**, v. 120, p. 8002–8024, 2015. doi: 10.1002/2015JA021116.

ZHOU, Q.; MATHEWS, J. D. On the physical explanation of the Perkins instability. **Journal of Geophysical Research**, v. 111, n. A12, 17, 2006. doi:10.1029/2006JA011696.